Compositional and Diagenetic Evolution of a Siltstone, with Implications for Reservoir Quality; an Example from the Lower Triassic Montney Formation in western Canada

Noga Vaisblat, Nicholas B. Harris, Korhan Ayranci, Matthew Power, Chris Debhur, David L. Bish, Rick Chalaturnyk, Federico Krause, Vincent Crombez, Tristan Euzen, et al.

Compositional and diagenetic evolution of a siltstone, with implications for reservoir quality; an example from the Lower Triassic Montney Formation in western Canada

Noga Vaisblat, Nicholas B. Harris, Korhan Ayranci, Matthew Power, Chris DeBhur, David L. Bish, Rick Chalaturnyk, Federico Krause, Vincent Crombez, Tristan Euzen, Sebastien Rohais
(Manuscript in preparation)

Abstract

Diagenetic models for silt-rich mudstone (siltstone) are less advanced than those for sandstone and clay-rich mudstone. In addition, the influences of diagenetic processes on reservoir quality in siltstone formations are poorly understood. Here we examine the roles of depositional facies, detrital composition, and diagenetic processes in the compositional evolution and reservoir quality of the Lower Triassic Montney Formation, a prominent siltstone-dominated reservoir in western Canada with very large reserves of oil, gas-liquids and natural gas. We applied advanced, high-resolution petrographic methods including SEM (SE, BSE, EDX and SEM-CL), XRD, and QEMSCAN technologies, as well as He-pycnometry on samples from 17 different locations within the basin that represent a range of depths and thermal maturities. Cross-cutting and overgrowth relationships and volumes of authigenic phases demonstrate massive precipitation of quartz, feldspar, dolomite, calcite and anhydrite cements at shallow burial depths, leading to compositional homogeneity among different lithofacies. We propose that the precipitation of large volumes of cement resulted from high fluid flux through the formation at shallow depth, possibly driven by reflux of concentrated seawater in nearshore saltpans. Siltstones preserve relatively high porosity and permeability at shallow burial depths, differing from clay-rich mudstones. In contrast to sandstones, deep burial diagenesis played a relatively

minor role in the compositional evolution of the Montney Formation siltstone and is expressed in the form of pressure solution and minor amounts of fibrous illite precipitation.

1. Introduction

In contrast to clay-rich mudstones (shales), whose diagenetic evolution has received much attention (for example, Nadeau et al., 2005; Laughrey et al., 2011; Milliken and Olson, 2017; Roberts and Elmore, 2018), coarser grained silt-rich mudstones (siltstones) are considerably understudied, with only one publication investigating the diagenesis of a pure siltstone (Orberger and Pagel, 2000) that documents physical compaction, diagenetic alteration of detrital quartz, K-feldspar and mica and precipitation of calcite and dolomite cements. Although it has been established that rock fabric (grain size and sorting) of mudstones significantly affects both diagenetic processes and reservoir quality (Peng et al., 2020; Wilson et al., 2020), studies of the composition and diagenesis of mixed siltstone-mudstone or sandstone-siltstone sequences (e.g., Varga et al., 2005; Taylor and Macquaker, 2014; Lai et al., 2016; Cao et al., 2017) rarely focused on silty intervals, or grouped siltstones and fine sandstones together (McBride, 1989).

In this paper, we investigate diagenetic processes and their influence on reservoir quality of the siltstone comprising the Lower Triassic Montney Formation of the Western Canada Sedimentary Basin (Armitage, 1962; Edwards et al., 1994; Zonneveld and Moslow, 2018). With estimated reserves of 450 TCF of gas, 14,520 MMB of gas liquids, and 1125 MMB of oil (National Energy Board, Government of Canada, 2013), the Montney Formation is a major unconventional host of hydrocarbons in the Western Canadian Sedimentary Basin (WCSB) and one of the most important siltstone hydrocarbon reservoirs in the world. The availability of long cores from a range of burial depths and thermal maturities makes the Montney Formation an appropriate test case for the investigation of siltstone diagenesis and its impact on reservoir properties. We examine the relationships between lithofacies, rock fabric (grain size and sorting), rock composition (detrital and authigenic components and organic matter) and link these variables to reservoir quality.

Because porosity and permeability in the Montney Formation siltstone are functions of these relationships, a thorough understanding of the temporal and geographic variability in these components is key to understanding the paragenesis and development of this reservoir. The sedimentary and diagenetic models developed in this study will facilitate the interpretation and understanding of siltstone reservoirs elsewhere in the world.

2. Geological setting

The Montney Formation covers over 130,000 km^2 in central and southwestern Alberta and northeastern British Columbia (Fig. 1). The formation was deposited on the western margin of Pangea during the Lower Triassic (Induan and Olenekian) (Davies et al., 1997; Utting et al., 2005; Zonneveld et al., 2010; Henderson et al., 2018), in a back-arc to foreland setting (Ferri and Zonneveld, 2008; Golding et al., 2016; Rohais et al., 2018). Paleogeographic reconstructions suggest that the basin was rotated approximately 30^o clockwise from its current position and positioned at 30^o North (Golonka et al., 1994; Davies et al., 1997; Blakey, 2014). A hot, periodically arid climate with seasonal monsoons prevailed in the region during the Lower Triassic (Davies, 1997; Golonka and Ford, 2000; Preto et al., 2010; Sun et al., 2012; Zonneveld and Moslow, 2018).

Extensive sedimentological studies of the Montney Formation describe deposition in a westward-dipping and deepening basin. Depositional environments varied, and sediments include shoreface facies, near-shore facies, off-shore successions, and submarine fans (e.g., Davies et al., 1997, 2018; Zonneveld et al., 2011; Playter, 2013; Crombez et al., 2016; Euzen et al., 2018; Moslow et al., 2018; Zonneveld and Moslow, 2018). Sediments comprising the Montney Formation were predominantly derived from the northwestern Laurentian continental margin to the east of the basin, with a smaller contribution from the Inuitian orogenic wedge and the Yukon-Tanana accretionary terrain to the north of the basin (Fig. 1) (Ross et al., 1997; Beranek et al., 2010; Golding et al., 2016). The Meosin-Muinok high in the southwest part of the basin (Fig. 1) was another potential sediment source, although it is not clear whether this high existed after the

Griesbachian (Early Induan) (Zonneveld and Moslow, 2014, 2018). Finally, a portion of the sediments in the Montney Formation may have been sourced from accretionary terrains postulated to have been positioned to the west of the basin in Early Triassic time (Zonneveld and Moslow, 2018 and reference therein) (Fig. 1).

The Montney Formation is subdivided into Upper, Middle and Lower Montney siltstone members. Other local members that are not discussed herein include the Pocketknife, Anten Coquina and Altares carbonate members, and the Calais and LaGlace Sandstone members. (Davies et al., 1997; Dixon, 2000; Moslow, 2000; Zonneveld and Moslow, 2018).

The Montney Formation unconformably overlies the Permian Belloy Formation (Fig. 2). The Coplin and sub-Jurassic unconformities, formed during the Late Cretaceous Laramide Orogeny, bound the formation from above in the eastern part of the basin (Gibson and Edwards, 1990; Edwards et al., 1994; Davies et al., 1997; Moslow, 2000) and reduce its thickness to < 1m in central Alberta. In the western section of the basin (northwestern Alberta and British-Columbia) where the Coplin unconformity cuts through younger intervals, the Montney Formation retains its full depositional thickness, reaching over 350 m, and is overlain by the Sunset Prairie Formation (Furlong et al., 2018) or the Doig Formation.

Burial history analysis indicates that from the time of deposition to the end of the Jurassic (a time span of ~ 100 million years), the formation was never buried deeper than 1000 m (Ness, 2001; Ducros et al., 2017). The Laramide Orogeny, beginning in the Early Cretaceous, triggered rapid subsidence and initiated high sedimentation rates in the WCSB. The Montney Formation reached its maximum burial depth and hence maximum temperatures at the culmination of this event (ca. 57.8 Ma) (Willett et al., 1997; Ness, 2001; Ducros et al., 2017; Rohais et al., 2018). From the end of the Paleocene to present, the basin has undergone continuous erosion and uplift.

In its present configuration, the Montney Formation deepens from northeast to southwest from less than 1 Km along the eastern subcrop to > 4 Km depth near the deformation front in the west. Corrected present day bottom-hole temperatures along this transect increase from <50^{o}C to >

100 °C (BC Oil and Gas Commission, 2012), with only the southwestern edge of the formation reaching temperatures >90°C. Thermal maturity ranges from R_o=0.59% in the northeast to R_o>2% in the deeply buried southwest section (Riediger et al., 1990; Ibrahimbas and Riediger, 2004; Sanei et al., 2015; Crombez, 2016; Romero-Sarmiento et al., 2016; Wood and Sanei, 2016; Crombez et al., 2017). Those trends are locally perturbed by syndepositional tectonism or paleotopography inherited from the pre-Triassic basin structure (Davies et al., 1997, 2018; Moslow and Davies, 1997; Polt and Krause, 1997; Zonneveld and Moslow, 2014, 2018; Moslow et al., 2018).

3. Methodology

3.1 Materials and sampling

Our analyses are based on a combination of drill cuttings samples and conventional core samples, selected to represent a range of grain sizes and depositional environments. Table 1 summarizes sample types, sampling intervals, and analyses obtained from each study well. Where possible, splits for all analyses were taken vertically from the same samples. Four long cores were selected for extensive analyses, based on the availability of cores intersecting all or most of the Montney Formation interval. Two cores represent distal and deeply buried section of the basin (wells 2 and 4 in Fig. 1); one well was selected to represent a more proximal, deeply buried section of the basin (well 9), and the last well was selected to represent a proximal section of the basin buried to a shallow depth. Additional thin sections (9) and core/outcrop samples (18) from thirteen other locations were examined to provide comprehensive coverage of the formation.

3.2 Core description

Detailed sedimentological descriptions were obtained for four cores (total length of 615 m, excluding a total of 51.5 m of missing core sections), recording sedimentary features as small as 1 cm to inform the suite of lithofacies present. Lithofacies were identified and distinguished on the basis of lithology, grain size, physical sedimentary structures, trace fossil assemblages, and

bioturbation intensity (BI). The lithological classification scheme was adopted from Macquaker and Adams (2003). According to this classification, a rock description is based on its sedimentary structures and all components that form more than 10% of the rock volume; mudstones are defined as rocks comprised of at least 50% grains that are silt-size or smaller. A rock can be dominated by a component (>90%), rich in a component (50-90%) or bearing a component (10-50%).

Lithofacies were divided into three groups based on their present-day apparent grain size distribution as measured by QEMSCAN analysis (see below). Present-day apparent grain size includes the detrital grain and cement overgrowths if present and thus reflects both the water energy in the environment of deposition and the amount of cement surrounding the detrital grains.

3.3 Petrography

Petrographic observations were obtained from thin sections SEM and SEM-CL analyses. Grain size in most samples is coarse silt size or smaller (<63 µm), rendering a point count via standard optical microscopy unreliable. Therefore, quantitative data was collected from Scanning Electron microscopy (SEM) images, and thin section analysis focused on identifying coarse diagenetic phases (calcite, dolomite, and anhydrite cements). Thin section samples were selected to represent all lithofacies described in the four cores. Thin sections were polished to 30 µm and one-half of each thin section was stained with alizarin red and potassium ferricyanide to facilitate carbonate mineral identification. We examined 73 thin sections under an Axio Zeiss Scope.A1 optical microscope equipped with a CITL Mk5 cold-cathode cathodoluminescence unit.

We used SEM analysis to study mineral morphology, distinguish between detrital grains and cements, constrain the paragenetic sequence based on overgrowths and cross-cutting relationships between minerals and define the timing of cementation relative to compaction. Petrographic analysis was also used to identify grain- or cement-supported fabrics and to distinguish mobilized hydrocarbons from depositional macerals.

Both freshly exposed surfaces of broken core chips and polished or ion-milled surfaces were examined by SEM. Polished samples were ion-milled with a Fischione Model 1060 SEM Mill at the University of Alberta. All samples were coated with gold or carbon prior to SEM investigation. SEM and energy dispersive X-ray spectroscopy (EDS) analysis was carried out on a JEOL 6301F Field Emission SEM (FE-SEM) or a Zeiss EVO LS15 EP-SEM, with an accelerating voltage of 20 kV, at the University of Alberta.

To evaluate cementation volumes and detrital quartz grain size, 17 ion-milled samples were analyzed with a FEI Quanta 250 FEG SEM equipped with a GATAN MonoCL4 detector (SEM-CL) and a Bruker Quantax EDX at the University of Calgary. For each sample, three (1000X magnification) or four (750X magnification) areas perpendicular to bedding were randomly selected, and secondary-electron, back-scattered electron, and cathodoluminescence images were recorded, along with energy-dispersive spectra. A 437-point grid was used for point counting on each image. EDS elemental maps were used to identify the mineral at each node, and SEM-CL images were used for separating detrital from authigenic phases. Errors associated with point count analysis were calculated following the method described in Van Der Plas and Tobi (1965). Detrital grain size was determined by measuring the longest axis of all detrital quartz grains within each image, and sphericity ratio was obtained by dividing the short axis by the length of the perpendicular, long axis at mid height.

3.4 Mineral composition and grain size

Mineralogical compositions for a large number of samples were also obtained through QEMSCAN analysis. Quantitative x-ray diffraction (XRD) analysis was conducted on a sample subset to verify QEMSCAN analysis results. All 178 drill cutting samples (wells 3, 5, and 11), together with 238 core chips samples collected in constant intervals (wells 2, 4, 9, and 15) and 297 pseudocutting samples (well 7) were selected for mineralogical analysis. A ~5 g sub-sample was randomly separated from each drill cuttings sample and analyzed. From each core samples,

a small (~ 2 cm^2), visually representative chip was cut perpendicular to bedding and analyzed. For well 7, a continuous sliver was cut along the entire length of the core and divided into 1-m intervals. Each interval was then crushed and mixed to generate pseudo-cuttings and a random subsample from each section (~50 g) was analyzed.

Quantitative mineralogical compositions, including clay minerals, average mineral size for each of the mineralogical phases identified, average grain size for feldspars and macroporosity values (pores >5 µm), were determined by QEMSCAN analysis at SGS Canada laboratories in Burnaby, BC, Canada. Repeatability of QEMSCAN measurements is very high (commonly <2% difference between repeated measurements of the same sample (M. Power, pers. com.). Compositional and porosity analysis by QEMSCAN is limited by the pixel size selected for analysis, 4.8 µm in this study. However, clay minerals in our samples were commonly aggregated rather than forming isolated laths, and we found that a pixel size of 4.8 µm was sufficient for appropriate description of the rock.

Mineral size reported from QEMSCAN analysis is an average calculated from the horizontal intercept lengths of mineral crystals within a sample. However, if crystals of the same mineralogical phase are adjoining, QEMSCAN analysis might report those grains as a single large particle. For this reason, grain size results from QEMSCAN analysis that were larger than the 95th percentile (P_{95}) were considered outliers. For a further discussion of estimates of particle size from QEMSCAN data, see Appendix 4.

To obtain grain size (as opposed to particle size) from QEMSCAN analysis, the mineral phase of interest was isolated from the dataset and touching particles were separated. Particles were then grouped into size-bins by the length of their apparent long axis. Results are reported as percent area of the mineral in each size-bin. We obtained grain size from both K-feldspar and Na-feldspar and calculated the weighted average grain size for each sample based on the relative abundances of the two feldspars. Grain size was not obtained for quartz grains because we were unable to separate touching grains sufficiently. To overcome this, we manually measured the

203 average quartz grain size on SEM images of 17 samples and then compared the results with the
204 average grain sizes obtained from QEMSCAN analysis of feldspars. This comparison revealed
205 that the average quartz grain size (measured manually) deviated ±5 μm from the average feldspar
206 grain size obtained from QEMSCAN analysis. Since this deviation is close to the minimum
207 detection limit of the QEMSCAN, the weighted average of feldspar grain size is sufficient for
208 describing grain size distribution in our samples.

209 For grain size analysis, a bin width (~1φ) was selected to avoid data skewing due to pixel size
210 (4.8 μm). Bins are very fine silt (4.8-7.8 μm), fine silt (7.8-15.6 μm), medium silt (15.6-31 μm),
211 coarse silt (31-63 μm), very fine sand (63-125 μm), and fine sand (125-250 μm). Grains with clay
212 compositions are considered to be clay-size, confirmed by petrographic analysis (see section
213 4.3). Although an effort was made to separate touching grains, it is possible that not all such
214 contacts are identified, particularly where grains touched along a flat contact. Similar to the
215 mineral size analysis, inclusion of touching grains in the dataset may have slightly skewed results
216 towards coarser grain size. The error associated with measuring grain size using this method is
217 difficult to assess, but the error is largest where associated with measuring grains that are close
218 to the pixel size (i.e., grains with diameter close to 5 μm). Present-day grain size frequency
219 distribution properties were calculated with the geometric formulas proposed by Folk and Ward
220 (1957).

221 Twenty-six samples representing all lithofacies from all cores were selected for quantitative
222 bulk composition and clay mineral XRD examination. Six samples were analyzed at the James
223 Hutton Institute, Aberdeen, Scotland. X-ray diffraction patterns were recorded with a Panalytical
224 Xpert Pro instrument using Ni-filtered CuKα radiation and an Xcelerator position-sensitive
225 detector, counting for 100 seconds per 0.0167° step between 3-70°2θ. The clay fraction (<2μm)
226 was separated by timed sedimentation in water, prepared as oriented mounts on glass and
227 scanned between 3-45°2θ in the air-dried state and after glycolation. The remaining 20 samples
228 were analyzed at the Mineralogy Facility at the Indiana University in Bloomington. X-ray diffraction

patterns were recorded with a Bruker D8 Advance X-Ray Powder Diffractometer, using CuKα radiation and a Si(Li) energy-dispersive detector, counting for 2 seconds per 0.02° step between 2-70°2θ. A large sample (~250 g) was finely ground and the clay fraction (<2μm) was separated by timed sedimentation in water. Clay concentrates (< 1 g) were prepared as randomly oriented mounts on zero-background quartz plates and scanned between 2-20°2θ in the air-dried state and after glycolation.

3.5 Porosity

Residual (present day) porosity in the siltstone is a product of mechanical diagenesis (compaction), chemical diagenesis (cementation and dissolution), and organic matter diagenesis. Estimates of residual porosity assist in assessing the portion of original porosity lost due to diagenetic processes. QEMSCAN analysis provided the cumulative area of pores larger than 4.8 μm. This macroporosity (pores >50 nm; Rouquerol et al., 1994) includes open pores and pores occluded with organic matter. QEMSCAN macroporosity values are reported for all drill cutting, pseudocutting and core samples analyzed.

Point count analysis provided values for primary porosity, secondary porosity, and porosity filled with organic matter for 17 samples. In addition, matrix porosity was measured at Trican (now AGAT) laboratories in Calgary Alberta (136 samples from wells 2, 4 and 15), Core Laboratories in Calgary, Alberta (109 samples, well 7), or Terratek, in Salt Lake City, Utah (50 samples, well 3), all using a Quantachrome Pentapyc analyzer 5200e. Samples from wells 2, 4, and 9 were taken from gas-producing wells and did not require cleaning prior to testing. Samples from well 15 (an oil-producing well) were cleaned prior to testing in a Dean-Stark device using a mixture of acetone (30 wt%), methanol (23 wt%), and chloroform (47 wt%). Matrix porosity comprises all pores larger than the helium atom radius (1.4 Å) and is thus considered the sum of macroporosity (pores >50 nm), mesoporosity (pores between 2 and 50 nm) and microporosity (pores <2 nm) (Rouquerol et al., 1994).

3.6 Organic Matter

Organic matter fills a portion of the pores in the siltstone. It is thus important to account for this phase when evaluating the porosity in the rock. Drill cutting samples (153) were analyzed for total organic content (TOC) using a RockEval VI pyrolysis at IFPEN, France. Details of this analysis are described in Crombez et al. (2016). In addition, 153 core samples and 109 pseudocutting samples were analyzed for TOC using the LECO-TOC method at Geomark Laboratories, Humble, Texas.

4. Results

4.1 Core Description

Fourteen lithofacies were identified in the four long cores (Table 2, Fig. 3). Lithology and physical sedimentary structures were the primary criteria used to characterize these facies, but in the upper parts of the formation, (sections that were reassigned to the Sunset Prairie Formation (Furlong et al., 2018), ichnological characteristics were also important. Core descriptions for the four wells are provided in Appendix 1.

All lithofacies described in this study but one (lithofacies D, a mudstone, comprising 0.2% of the total core length examined) are either silt-dominated or silt-rich mudstones. In the distal downdip wells 2 and 4, the most abundant lithofacies are the laminated siltstone (lithofacies G/H) and the massive siliceous clayey siltstone (lithofacies J), both of which contain 86% silt-size grains. Other important lithofacies in the distal wells are the faintly laminated calcareous siltstone (lithofacies F, 83% silt), and the interbedded siliceous-mudstone and calcareous- siltstone (lithofacies P, 87% silt). The bioturbated, calcareous, sandy siltstone (lithofacies M/N, 73% silt) is found only at the uppermost section of the two distal cores and is part of the Sunset Prairie Formation (Furlong et al., 2018). Lithofacies G/H (laminated siltstone), and lithofacies J (massive siliceous clayey siltstone) were also identified in the section identified as the Sunset Prairie Formation but are not exclusive to this unit, (Table 3).

279 In the deeply buried proximal (to the Meosin Muinok High; Fig. 1) well 9, the most abundant
280 lithofacies is the massive sandy siltstone (lithofacies B). The average silt and sand contents in
281 this lithofacies are 76% and 19%, respectively, but both grain size classes are quite variable (47-
282 87% for silt; 6-47% for sand). Other important lithofacies in well 9 are the massive siliceous clayey
283 siltstone (lithofacies J, 86% silt) and the hummocky to ripple cross-stratified sandy siltstone
284 (lithofacies O, 82% silt).

285 In the proximal, shallow buried, updip well 15, the dominant lithofacies is interlaminated
286 siltstone and sandstone (lithofacies A). This lithofacies displays a wide range of silt and sand
287 content. Silt content varies between 31 and 87% with an average of 65%, and sand content varies
288 between 9 and 40% (2 samples have higher sand content of 62 and 53%) and an average of
289 23%. Dolomitic siltstone (lithofacies E) is the second major lithofacies in well 15. This highly
290 dolomitized lithofacies contains 78 to 98% silt grains (average of 84%), and up to 3% sand grains
291 (average of 2%).

292 **4.2 Grain size distribution**

293 Mudstones are defined as rocks composed predominantly of clay- and silt-size grains (< 62.5
294 μm) (Aplin et al., 1999; Flemming, 2000; Macquaker and Adams, 2003; Lazar et al., 2015). Fig. 4
295 shows the average and range of cumulative grain size distribution for each lithofacies. The graphic
296 statistical variables (Folk and Ward, 1957) were calculated for each sample from the graphs in
297 Fig. 4.

298 Samples were also grouped into larger grain-size bins: sand (> 63 μm), silt (4.8 - 63 μm) and
299 clay (<4.8 μm) and plotted on a ternary diagram. Based on a combination of the Folk and Ward
300 (1957) classification and the Macquaker and Adams (2003) classification, lithofacies were divided
301 into three groups (Table 4, Fig. 5). Group one lithofacies (lithofacies A, B, C, E, M/N, and O) are
302 somewhat coarser than other lithofacies and most samples in this group contain >10% sand size
303 grains. Samples in these lithofacies are poorly to moderately sorted ($0.5 < \sigma1 < 1.5$) with a

positively skewed grain size distribution (tail of fine grains), and have sedimentary structures such as current ripples, hummocky cross stratification, and rip-up clasts indicative of higher water energy in the depositional environment (Table 2).

Group two lithofacies (lithofacies G/H and I) are siltstones with up to 10% sand content, moderately sorted ($0.5 < \sigma1 < 1$) and have a nearly symmetrical grain size distribution (skewedness ~ 0). Samples in this group are commonly laminated. Group three lithofacies (lithofacies F, J, K, L, and P) are all fine grained, with <5% sand size grains, all moderately sorted ($0.5 < \sigma1 < 1$) with a negatively skewed grain size distribution (tail of coarse grains). With the exception of lithofacies P, samples in group three are massive in appearance. Lithofacies F (faintly laminated calcareous siltstone) showed a somewhat different grain size distribution in samples taken from well 2 and well 5. Although the mode in samples taken from these two wells is different from the other wells, (36.72 µm for well 2 and 69.74 µm for well 15), statistical variables are not significantly different for samples from either of the two wells, or for the combined dataset of all samples (Table 2.3). Consideration of the error associated with the graphic statistical parameters do not change classification of any of the lithofacies.

4.3 Detrital grain assemblage

Total mineral compositions obtained from QEMSCAN analysis, including diagenetic phases, for samples from all wells are shown in Fig. 6. Quantitative XRD results confirm QEMSCAN findings (appendix 4). Detrital minerals were identified through SEM-CL analysis and quantified by point count analysis on SEM-CL images (Table 4). Detrital quartz occurs as angular to subangular grains (Fig. 7a, i-l) and constitutes an average of 25.5% of bulk rock composition and 71.3% of total quartz (Table 4). Detrital chert grains (2.7% of bulk composition and 7.4% of total quartz) are identified by mottled blue-red luminescence pattern, and a microporous texture of silica particles that contain abundant porosity and inclusions (Fig. 7b, c). Rare collapsed agglutinated foraminifera, identified by a prominent midline, are present (Fig. 7d).

Detrital feldspar grains are angular to subangular (Fig. 8). K-feldspar and Na-feldspar average 6.9% and 6.1% of bulk samples, 67.7% and 66.0% of total feldspar, respectively. Under the optical microscope, feldspar grains are commonly weathered along cleavage planes and variably dissolved.

All micas and most clays in the siltstone are of detrital origin. Micas include muscovite and biotite. Mica grains are subangular to subrounded, and many are bent, displaced along cleavage planes, and have splayed edges in response to compaction (Fig. 9a). Based on QEMSCAN analysis, muscovite has the highest concentrations of all micas (up to 7.5 wt%), chlorite has a maximum concentration of 4.2 wt%, and biotite is present only in minor amounts (<1.5 wt%). Chlorite was recognized in both QEMSCAN and XRD analyses and was identified in SEM analysis as detrital material of metamorphic origin based on appearance and relatively coarse grain size (Fig. 9a) (also noted by Zonneveld and Moslow, 2018; Moslow et al., 2018) and is similar in morphology to other mica grains. Mica-like chlorite in our samples is susceptible to dissolution and breakage along cleavage planes (Fig. 9b).

Mixed layer illite-smectite (MLIS) clays are present as clay coats (Fig. 9c) and aggregate grains between detrital grains (Fig. 9d). MLIS is present in all the samples examined, but concentrations determined by QEMSCAN analysis vary across the basin from just under 1 wt% to over 30 wt %. Point count analysis results (Table 4) are somewhat lower than the QEMSCAN-reported concentrations, with average total clay content of 3% and a maximum of 7%. XRD analysis of glycolated clay mounts established a maximum of 5% expandable layers for MLIS throughout most of the basin. In only three samples (well 16 from the Dixonville Delta) does MLIS show higher expandability of 20%.

Dolomite occurs predominantly as rounded to well-rounded detrital grains, surrounded by rhombohedral overgrowths. These grains are identified by their bright luminescence, weathered (cloudy) appearance in thin sections (Fig. 10a), and the presence of dissolution pits (Fig. 10b) that are commonly <1.5 µm in diameter but locally larger in samples from cores 15 and core 9 (>5

355 µm) (Fig. 10d). Total dolomite concentration averages 17.5% of bulk composition. Only a third of
356 the dolomite in the Montney is of detrital origin (Table 4; 5.4% of bulk composition and 32.2% of
357 total dolomite on average); the remaining fraction is diagenetic in origin.

358 Detrital grains of different minerals vary in size. However, since detrital quartz is the least
359 susceptible to dissolution in our samples, we used it as a proxy for detrital grain size, measured
360 on SEM-CL images for samples from wells 2, 4, and 9. Detrital quartz grain size ranges in
361 individual samples from 1.4 to 95.6 µm, but most of the grains measured (P_5-P_{95}) show a narrower
362 range of 3.5 to 42.15 µm. Wells 2 and 4 have a smaller detrital quartz grains (average 12.65 µm)
363 than well 9, which averages at 25.2 µm. The sphericity index (short grain axis / long grain axis) is
364 0.55 ± 0.20 for all three wells, indicating a majority of elongated detrital quartz grains.

365 **4.4 Authigenic phases**

366 Authigenic minerals were identified through thin section, SEM and SEM-CL analyses. Cement
367 volumes were quantified from point count analysis of SEM-CL images (Table 4).

368 **4.4.1 Quartz**

369 Two generations of authigenic quartz are present (Fig. 7a). The earliest, more abundant
370 generation exhibits blue cathodoluminescence and comprises an average of 5.1% of mineral
371 volume, and 14.2% of total quartz. The second generation of quartz cement is identified by bright
372 red cathodoluminescence and forms thin rims surrounding the blue quartz cement or detrital
373 quartz grains. Red luminescent quartz cement averages 2.3% of bulk composition and 7.0% of
374 total quartz. Fractured quartz grains are uncommon, with linear fractures typically 1 µm in width.
375 Fractures are filled with either blue or red quartz cement (Fig. 7 i, j). Rarely, a complicated network
376 of red cement fills fractures developed in blue cement (Fig. 7k) or shattered detrital quartz grains
377 (Fig. 7l).

SEM images of freshly broken surfaces show that quartz cement forms overgrowths (Fig. 7e), euhedral microcrystalline cement (Fig. 7f), and silica nanospheres (Fig. 7g) (terminology adopted from Longman et al., 2019). Development of quartz overgrowths was inhibited to some degree by detrital clay coating (Fig. 7h), and in many cases overgrowth surfaces are speckled with angular holes <1µm (Fig. 7i). Silica nanospheres are a minor phase, locally forming grain coats that are too thin to identify in polished samples.

4.4.2 Feldspars

Authigenic feldspars have dark cathodoluminescence under SEM-CL (Fig. 8). K-feldspars and albite each form in a single overgrowth generation (Fig. 8a, b), and K-feldspar also forms discrete euhedral crystals (Fig. 8c). Feldspar cement constitutes 32.3% and 21.4% of total K-feldspar and total albite, respectively. K-feldspar cement overgrows detrital grains of both feldspar types (Fig. 8a, e), whereas albite cement overgrows only detrital Na-feldspar (Fig. 8b). A low-luminescing albite appears to replace both K-feldspar (Fig. 8d) and Na-feldspar (Fig. 8e). We note that these grains might also be interpreted as plutonic detrital grains with low luminescence albite. However, we favor the interpretation of albitization due to the nonlinear morphology of the low-luminescing albite and its association with porosity that is potentially secondary (Milliken, 1989). Replacive albite accounts on average for 13.5% of total Na-feldspar.

Extensive dissolution of K-feldspar cement is a minor phenomenon but is important locally. Dissolution occurs mainly along the boundary between the detrital grain and the cement rim (Fig. 8l) and is most common in Well 15, and to a lesser degree in Well 9.

4.4.3 Dolomite

At least four generations of dolomite cement were identified under CL and SEM-CL microscope (Fig. 10a, b). Absence of evidence for dissolution of authigenic dolomite, and sharp transitions between cement generations suggest continuous cementation with rapidly changing fluid composition. The last dolomite generation is an iron-rich dolomite (Fe ~ 5 wt%, based on

QEMSCAN analysis), easily identified by the brighter BSE signal and quenched cathodoluminescence (Fig. 10b). In some samples, iron-rich dolomite replaces earlier dolomite cements (Fig. 10c), and occasionally detrital dolomites.

Authigenic dolomite amounts to 12.1% of rock volume on average, and 67.8% of total dolomite, and in most samples, more than 30% of the total dolomite is Fe-rich. Dissolution pits in detrital dolomite are either empty or filled with authigenic pyrite, phosphate, and rarely quartz and K-feldspar (Fig. 10a, b).

4.4.4 Calcite

Most calcite occurs as pore-filling poikilotopic cement (Fig. 10e) and to a much lesser extent as a replacive phase after detrital dolomite (Fig. 10f). Calcite concentrations vary greatly and unpredictably and range between 0.1 and 40.8% of the rock volume. Two generations of poikilotopic calcite were identified (Fig. 10g*)*, indicated by different intensities of blue cathodoluminescence. The first calcite cement generation (37.1% of total calcite) contains euhedral pyrite inclusions. The second calcite cement generation (62.3% of total calcite) has the same CL pattern as the calcite that replaces dolomite. Point count analysis establishes that calcite that replaces dolomite accounts for < 1% of total calcite in the Montney Formation (Table 4). Moldic porosity and associated dolomitic and possible phosphatic infill cements of shells and other bioclasts (Fig. 10h, i) are evidence of dissolution and/or replacement of the primary aragonite or calcite.

4.4.5 Clay minerals

Kaolinite is present in significant amounts (P_{50}>1.75 %) only in wells 11 and 15. Samples from wells 15 and 16 also contain abundant authigenic kaolinite crystals and vermiform kaolinite that fills open pores (Fig. 9e). Authigenic fibrous illite is pore-bridging and pore-lining, nucleating on detrital clays (Fig. 9f), mica grains, and rarely on kaolinite. Fibrous illite abundance has no clear relationship to burial depth or lithofacies association. In addition, fibrous illite crystal growth is not

uniform, with fiber lengths varying from several micrometers in some samples to less than one micrometer in others. We observed no clumping of illite fibers that can sometimes occur in air-dried samples. In the quantitative data from the QEMSCAN analysis, fibrous illite is grouped together with MLIS clays.

4.4.6 Pyrite, anhydrite, and phosphate

Pyrite concentrations vary between 0.5 and 5.7% of the rock volume. Pyrite occurs in a range of forms and associations including framboids and euhedral crystals (Fig. 11a), as inclusions in a variety of cements (calcite, dolomite, feldspar and chert), in open pore space, within patched of organic matter, and between sheets of mica grains. All pyrite identified is interpreted to be authigenic, although some of the pyrite may be of detrital origin, based on the presence of clay coats on framboids (Fig. 11b).

Anhydrite concentrations are generally lower than 2% of the rock volume, but concentrations of up to 10% anhydrite were recorded in several samples. All anhydrite is authigenic and forms bedding-parallel poikilotopic cement (Fig. 11c) or is concentrated in nodules. It was not possible to distinguish different cement generations using SEM-CL due to the non-luminescent nature of anhydrite and lack of morphological differences between possible cement generations.

Phosphate concentrations are under 1 wt% in 90% of the samples. Phosphate occurs as phosphatized shell and shell debris (Fig. 10i), phosphatic nodules (Fig. 11d), grain coatings, or pore-filling cement. In addition, phosphate is also present as inclusions in dolomite and anhydrite cements (Fig. 11e). Although we considered all phosphate in our samples as authigenic, it is possible that some of the phosphate, particularly phosphate comprising shells and shell fragments is primary.

4.4.7 Organic matter:

Total organic carbon content averages 1.2 wt%, with minimum and maximum values of 0.05 and 4 wt%, respectively. Organic matter concentrations show no consistent trend with depth, but

concentration generally decreases eastward toward the shallow basin. No primary (depositional) macerals were identified in this study based on morphology, thus the organic matter in our samples appears to be of secondary origin (i.e., bitumen or pyrobitumen). Organic matter fills interparticle porosity between detrital and authigenic particles (Fig. 11a), as well as intraparticle porosity in mica, pyrite, feldspars and dolomites (Fig. 11f).

4.5 Porosity, compaction, and Intergranular Volume (IGV)

Matrix porosity from helium pycnometry ranges from 0.6 to 27.1 % with an average of 9.0 %. The error reported for these measurements is under 6% for all samples, and most commonly under 1.5%. Porosity reported from QEMSCAN analysis, which includes both open pores greater than 4.8 µm and organic matter, varies between 0.2 and 22.7%. In contrast, open porosity (primary and secondary porosity) estimated through point count analysis (Table 4) varies between 0.1 and 3.7%. No clear porosity-depth trends were observed with any method of porosity measurement. Matrix porosity and QEMSCAN macroporosity values are presented in Fig. 12. Matrix porosity (which includes micropores, mesopores and macropores) is consistently greater than QEMSCAN porosity. Porosity measured by point counting is equal to or less than porosity measured by QEMSCAN, indicating that a large fraction of the pores is smaller than 4.8 µm, although we note that the QEMSCAN macroporosity data also include large (> 4.8 um) pores filled with organic matter. Secondary porosity (porosity generated through framework grain dissolution (Siebert et al., 1984; Harris, 1989) averages 4.2% of total porosity and only 0.2% of bulk rock volume.

Evidence for mechanical compaction is present at the microscopic scale in the form of bent or broken mica grains (Fig. 9a, b), deformed clay clumps around detrital grain (Fig. 9c), and fractured detrital grains (Fig. 7i-l). To quantify mechanical compaction, we assess IGV_m (Milliken and Olson, 2017) a modification of intergranular volume (IGV; Houseknecht, 1987; Paxton et al., 2002, among others) that is more appropriate for assessing compaction of mudrocks. IGV_m

478 includes the residual primary porosity, cements, and pore-filling secondary organic matter. IGV_m
479 values obtained from point count analysis are presented in Table 4.

480 With the exception of the sample from lithofacies K, samples from group one (on average, the
481 coarsest grained samples) have the highest IGV_m values, whereas samples from groups two and
482 three have similar IGV_m values (Table 4). However, it is important to bear in mind that the reported
483 IGV_m ranges may be heavily influenced by the limited number of samples associated with each
484 lithofacies. Samples from lithofacies group 1 (lithofacies B, M/N, and O) and group 2 (lithofacies
485 G/H) have similar IGV_m values, ranging approximately between 28 and 50%. There are no
486 systematic differences in the IGV_m values between different lithofacies or samples from different
487 wells. The sample from well 9 has the lowest IGV_m value (31.1%), the samples from well 2 have
488 the highest average IGV_m value (41%), and samples from well 4 have an intermediate IGV_m value
489 (37.5%).

490 Evidence for chemical compaction (pressure-solution) is recorded in a large number of
491 samples, affecting mostly silicate minerals. For the most part, pressure-solution features only
492 penetrate cement rims of silicate minerals (Fig. 11a), and in fewer cases non-cemented detrital
493 quartz grains (Fig. 11b) As overgrowths are commonly of variable thickness, even around a single
494 grain, quantitative assessment of dissolved volumes is difficult.

495 **4.6 Relative timing of diagenetic events**

496 Our data from the Montney Formation represent a wide range of burial depths and organic
497 matter maturities, but a few systematic differences in the nature and distribution of diagenetic
498 phases with depth are expressed in our data set that can be used to differentiate the age and
499 timing of events. Based on petrographic features such as cement overgrowths and crosscutting
500 relationships, we divide diagenetic processes into pre-burial diagenesis and post-burial
501 diagenesis. The paragenetic sequence for the formation is presented in Fig. 13 and described
502 below.

4.6.1 Pre-burial diagenetic events

Early or pre-burial diagenesis occurs at or very close to the sediment-water interface. Preburial diagenetic processes include dissolution of unstable aragonite/calcite shells (Fig. 10h), phosphatization of bioclasts (Fig. 10i), and growth of phosphatic nodules (Fig. 11d) and grain coats (Fig. 11e).

4.6.2 Post-burial diagenetic events

Post-burial diagenetic events are largely characterized by mechanical compaction and massive cementation by carbonate and silicate minerals. The first cements to precipitate were the two generations of quartz (Fig. 7a), one generation of K-feldspar (Fig. 8a), one generation of Na-feldspar (Fig. 8b), and several generations of dolomite that include a final Fe-rich dolomite cement (Fig. 10b). Because no crosscutting or systematic overgrowth relationships were identified between the cement phases, we suggest they all precipitated relatively early (see discussion below) and approximately contemporaneously.

The earliest authigenic phases include quartz cement, non-ferroan dolomite cement, and feldspar cement and replacement, each surrounding a detrital core of the same mineral except for K-feldspar, which locally overgrows plagioclase. Two generations of poikilotopic calcite cement were identified, both precipitated around earlier authigenic phases (quartz, feldspars and dolomite), (Fig. 10e). The first generation of calcite cement contains pyrite inclusions (Fig. 10g) and thus postdates the formation of at least some of the pyrite. Calcite that replaces dolomite (Fig. 10g) shares similar luminescence with the second generation of calcite cement, suggesting that both precipitated from a single fluid and are contemporaneous.

Much like calcite cement, anhydrite is poikilotopic, engulfing early authigenic phases (quartz, feldspar, and dolomite), (Fig. 11c). None of our SEM-CL samples contained both anhydrite and calcite, and we were unable to constrain the relative temporal relationship between these two

phases. However, as both calcite and anhydrite cements engulf and thus postdate quartz, feldspar and dolomite cements, we interpret them as approximately contemporaneous.

Pressure solution penetrates cement rims of quartz and feldspars and were thus developed after these cements precipitated (Fig. 14). However, the temporal relationship between pressure solution and calcite and anhydrite cements based on petrographic evidence is unclear.

Pyrite occurs in numerous forms, as inclusions in different cements (calcite, dolomite, feldspar and chert), in open pore space (Fig. 7b), within patches of organic matter (Fig. 9b, d; Fig. 11a), and between sheets of mica grains. This suggests that pyrite formation was a recurring process that began shortly after deposition and ended, at the earliest, with the formation of calcite cement although crystal growth in open pores could have continued for much longer.

Residual hydrocarbons (bitumen and pyrobitumen) plug a large portion of the original inter- and intragranular pores, including secondary porosity that developed in cemented grains (Fig. 11a, f). This indicates that hydrocarbon emplacement postdated cementation of feldspars, quartz, dolomite, calcite and anhydrite and that grain dissolution either predated or was contemporaneous with the emplacement organic matter. In samples where secondary porosity is not filled with organic matter (Fig. 8f), this temporal relationship is less well constrained. Micropores developed in some of the organic matter in wells at high thermal maturity.

As suggested by the preservation of their delicate structure and their pore filling and/ or pore bridging nature, the last phases to crystalize in the Montney Formation are fibrous illite (Fig. 9f) and kaolinite clays (Fig. 9d), especially in the shallowly buried eastern wells (well 15 and well 16). Fibrous illite locally overgrows kaolinite, indicating that illite precipitation postdates the formation of kaolinite.

4.6.3 Unconstrained diagenetic events

Some diagenetic events lack clear evidence with regard to timing. Minor dissolution identified in detrital chert (Fig. 7b), feldspars (Fig. 8b) and dolomite grains (Fig. 10b) is not well constrained.

552 Dissolution is restricted to detrital grains and does not occur in any of the cement overgrowths.
553 Partial dissolution of detrital grains may be associated with pre-burial transport and weathering
554 processes but could also be a post-depositional event. Similarly, we were not able to constrain
555 the timing of albitization of detrital K-feldspar (Fig. 8d) and Na-feldspar grains (Fig. 8e). Finally,
556 the relative timing of hydrocarbons migration/generation with respect to clay minerals precipitation
557 is not entirely clear.

558 **5. Discussion**

559 **5.1 Grain size, sorting, and sediment transport mechanism**

560 Grain size and sorting can provide information about depositional processes and energy levels
561 of the transporting medium (commonly wind or water) at the site of deposition. The mean grain
562 size of samples from group one averages at 4.2 φ (54 μm) whereas mean grain size of samples
563 from groups two and three averages at 5.0 φ (31 μm). The mode (most abundant grain size)
564 varies over a narrow range, between 4.4 - 4.8 φ (36.7 and 46.3 μm). Our observations are
565 consistent with Barber (2002) and Sanei et al. (2016), who also assessed grain size in the
566 Montney Formation through microscopy, but our modal values are slightly smaller than Davies et
567 al. (1997), who reported that grain size varied between 3 and 4.6 φ (40 to 120 μm) with a majority
568 of the samples falling between 3.5 and 4 φ (62.5 - 88 μm).

569 Our samples are moderately to poorly sorted (based on 1σ, Table 2), whereas other studies
570 describe the Montney siltstone as moderately to well-sorted (Davies et al., 1997; Barber, 2002;
571 Sanei et al., 2016). Different grain size distribution (Davies et al., 1997) and sorting patterns
572 (Davies et al., 1997; Barber, 2002) arise because prior studies relied largely on thin section
573 analysis and almost exclusively examined shoreface and turbidites facies within the Montney that
574 tend to be better sorted, whereas this study examined a wider range of lithofacies using high
575 resolution electron microscopy imaging. Sampling locations were not reported by Sanei et al.
576 (2016), making comparison to our results difficult.

Similar to Davies et al. (1997) and Barber (2002), we suggest that grain size distribution indicates that sediments were introduced into the basin via a mixed traction and suspension aeolian transport mechanism (Tsoar and Pye, 1987; Bullard and Livingstone, 2009; Nickling and Neumann, 2009). In this regard, the Montney siltstone is similar to other loess deposits (e.g., Mason et al., 2003; Sun et al., 2006; Prins and Vriend, 2007; Crouvi et al., 2008; Nottebaum et al., 2015), although the medium in which sediments were finally deposited was water. Zonneveld and Moslow (2014; 2018) proposed a more complex array of transport processes, involving wind-blown material accumulation in fluvial channels of ephemeral rivers that drained into the basin during flash floods. The authors, however, agreed that aeolian processes contributed significantly to sediment accumulation in the Montney Formation siltstone.

5.2 Depth and time constraints on diagenetic processes

Compaction and cementation act in combination to reduce the depositional porosity of the rock. However, while mechanical compaction acts to reduce IGV (or IGV_m in mudrocks), cementation can preserve IGV or IGV_m if cementation occurs before maximum compaction was achieved. Once formed and unless dissolution of cement occurs, cement volume remains unchanged with continuing burial. Thus, estimates of IGV_m and cement volumes can constrain dominant mechanisms of porosity loss and the timing of cement formation, provided some knowledge of initial porosity is available.

Information on the depositional porosity of silt-size sediments is scarce. Hedberg (1926) and Chilingarian (1983) estimated initial porosities for siltstones to be between 50 and 80%. A compilation of porosities for silt-rich sediments (silt-size grain content of 60 to 90%) between 0 and 1700 m from the Ocean Drilling Program was reported by Kominz et al. (2011). In this dataset, depositional porosity of silt-rich sediment varies between 40 and 95%. However, within a few tens of meters of burial, porosity in most measurements is reduced to about 60%. We thus selected 60% as the depositional porosity for the Montney siltstone, similar to values of 53 to 57% assumed

602 by Ness (2001) in a basin modeling study of several Montney wells. In the Kominz et al. (2011)
603 dataset, porosity for silt-rich sediments is well-constrained (more than one measurement in similar
604 depths) up to a depth of 1200 m (black curve, Fig. 15).

605 Calculations of IGV_m and estimates of the timing of cement formation can be erroneous if
606 cements were dissolved. In the Montney Formation, however, there is little evidence for cement
607 dissolution, other than through pressure solution. From SEM-CL analysis, we established that
608 chemical compaction affected mostly overgrowths and was rarely documented to influence detrital
609 grains. Although it is difficult to quantify the effect of pressure solution, it is reasonable to assume
610 that chemical compaction made only a minor contribution to porosity reduction in the formation.

611 Minimum IGV_m value (27.6%, sample 5V, well 4) can be used as a lower limit to the
612 depositional porosity of the sediment, and maximum IGV_m value (69.4%, sample 4V, well 4) can
613 be used as the upper limit of sediment porosity at the time of deposition. The IGV_m of most
614 samples (14 of 17 samples) is between 31.1 and 51.9. All the samples were retrieved from depths
615 larger than 2280 m (Table 4), but the high IGV_m values of the samples suggest that compaction
616 ceased at a much shallower depth, ranging from 150 to 1100 m. Green arrows in Fig. 15 indicate
617 the cementation depths of three samples with IGV value of 52% (Fig. a), 40% (Fig. 15b) and
618 27.6% (Fig. 15c). Samples with $IGV_m > 60\%$ could not be placed on the compaction curve. An
619 IGV_m value that is higher than the depositional porosity of the rock suggests that some of the
620 cement precipitated in pores previously occupied by detrital grains.

621 Depositional porosity of clean, well-sorted sands is approximately 45% (Paxton et al., 2002).
622 Sandstones reach maximum compaction at about 2 to 2.5 Km, at which point porosity stabilizes
623 at 26% and is not further reduced with additional burial (Paxton et al., 2002) (Fig. 15). The silt-
624 rich sediment of the Montney Formation is moderately to poorly sorted (Table 3), and it is possible
625 that its initial porosity is lower than 60% and closer to that of sands. In this case, the siltstone
626 compaction curve should shift closer to the sandstone compaction curve (blue curve in Fig. 15),
627 which would result in shallower estimates of cementation depth for most of our samples. If

depositional porosity was closer to 45%, this would also indicate that samples with IGV_m values larger than 45% have experienced some degree of detrital material dissolution.

IGV_m can also be used to assess the relative effects of compaction (compactional porosity loss, COPL) and cementation (cementational porosity loss, CEPL) using equations 1 and 2 (Ehrenberg, 1989):

$$(1)\quad COPL = \emptyset_i - \frac{\left((100-\emptyset_i)*IGV_m\right)}{100-IGV_m}$$

$$(2)\quad CEPL = (\emptyset_i - COPL) * \frac{C_m}{IGV_m}$$

Where $\emptyset_i$ is the depositional porosity of the sediment, and C_m is the combined volume of cement and secondary organic matter (bitumen) in primary pores (Milliken and Olson, 2017). Assuming a depositional porosity of 60% in these calculations, cementation was responsible for more porosity loss than compaction (CEPL > COPL; Table 4) in samples that were cemented at a very shallow depth (<300 m) and thus have preserved IGV_m values larger than 44%. Heavily cemented samples are not unique to a single well, a single lithofacies, or a particular member of the formation, making it difficult to identify an individual control for cementation in these samples.

Compaction was responsible for most of the porosity loss in a majority of the samples (COPL > CEPL). These samples were cemented at a greater depth (300 - 1100 m) and thus record smaller IGV_m values (27.6 - 40.6%). This suggests that the initial compaction rate of the siltstone was very high, and only samples that were cemented within the top 300 m of the interval retained high IGV_m values. However, even samples with lower IGV_m values were also cemented at a relatively shallow depth (< 1100 m). The presence of reworked clasts containing dolomite cement at the top of each Montney member (Davies et al., 2018) and low dolomite formation temperatures (<60°C) identified from fluid inclusion analyses (Davies et al., 1997) further support our interpretation of cements precipitation at shallow burial depths.

Large volumes of cements together with indications for shallow cements precipitation suggest the existence of an open pore network that enabled massive fluid flow through the rock. Ness (2001) and Ducros et al. (2017) demonstrated through basin modeling that the Montney experienced slow burial for 100 million years following deposition, reaching a burial depth of about 1,500 m at the end of the Jurassic. We propose that shallow burial cementation occurred during this time period (Fig. 13).

5.3 Preburial and shallow burial diagenetic processes

In order to understand processes controlling dissolution and cementation at the sediment-water interface and during very shallow burial, one needs to consider the environmental conditions under which the Montney siltstone was deposited. Early Triassic oceans were hot, acidic, and at least intermittently oxygen-depleted (Sobolev et al., 2011; Zonneveld, 2011; Sun et al., 2012; Clarkson et al., 2015; Kiehl and Shields, 2005). Worldwide ocean acidification began at the end of the Permian and extended into the Middle Triassic, caused by increased atmospheric CO_2 concentrations that originated from the Siberian Traps volcanic eruptions.

Elevated atmospheric CO_2 was also responsible for elevated surface ocean temperatures, which exceeded 32^{o}C near the equator (Sun et al., 2012) and 26^{o}C at 30^{o}N latitude (Kiehl and Shields, 2005). Models show that ocean temperatures did not significantly diminish with depth, leading to arrested oceanic circulation and widespread deep-water anoxia (Kiehl and Shields, 2005). Anoxic or dysoxic bottom water conditions are proposed for the time of the Montney siltstone deposition, based on the presence of sulfide pseudomorphs of pollen grains and spores, the paucity of trace fossils, and concentration of redox-sensitive trace elements (U, V and Mo) (Zonneveld et al., 2010; Crombez et al., 2017). Under acidic and reducing conditions, the saturation limits in ocean water are high for alkaline elements such as sodium, potassium and calcium, as well as magnesium and iron (Tribovillard et al., 2006; Caracciolo et al., 2014).

5.3.1 Calcite dissolution:

676 The lack of detrital calcite in the Montney Formation can be attributed to global oceanic
677 acidification during the early Triassic (Sobolev et al., 2011; Zonneveld, 2011; Clarkson et al.,
678 2015) and elevation of the calcite compensation depth (CCD) to shallow marine settings (Playter,
679 2013). Acids released by decaying organic matter (Wallmann et al., 2008) or the presence of
680 unstable aragonitic precursors may have also contributed. Dissolution processes may also have
681 formed the small dissolution pits observed in many of the detrital minerals (mainly feldspars,
682 dolomite, and chert), although these features may also be related to grain weathering during
683 sediment transport.

684 **5.3.2 Feldspars and dolomite cementation**

685 We suggest that pH stabilized shortly after deposition through mineral dissolution that
686 released alkali elements into the pore water. The increased alkalinity was expressed through the
687 precipitation of feldspars and dolomite cements, as well pyrite and iron-rich dolomite, indicating a
688 decrease in the solubility of the dissolved alkali elements (Tribovillard et al., 2006; Caracciolo et
689 al., 2014).

690 Dolomitization models, specifically the evaporative-brine refluxing model (Saller and
691 Henderson, 1998 and reference therein; Warren, 2000; Machel, 2004) may apply to the Montney
692 Formation. This model, proposed originally by Adams and Rhodes (1960) and documented in
693 ancient and modern platforms and ramps worldwide (Saller and Henderson, 1998; Warren, 2000;
694 Machel, 2004), provides a mechanism for fluxing large volumes of water through shallowly buried
695 sediment. According to this model, dense hypersaline brines, saturated with calcium and
696 magnesium. form in lagoons through evaporation and sink downward through the underlying rock
697 where dolomite precipitates due to retrograde solubility (Warren, 2000; Jones and Xiao, 2005).

698 The reflux model provides an explanation for the large volumes of early cement in the Montney
699 Formation, in particular the dolomite cement that comprises 12% of the rock volume. We postulate
700 that an evaporative lagoon existed on the updip margin of the basin, where dense saline brines

formed and migrated downward and basinward, following permeable pathways. Although the updip portion of the Montney Formation was eroded during the Late Cretaceous Laramide Orogeny (Edwards et al., 1994; Davies et al., 1997, Moslow, 2000), the presence of an evaporative lagoon is consistent with our understanding of Early Triassic climate for the area, which is inferred to have been arid based on the presence of aeolian dunes, palynomorphs, regionally extensive anhydrite and reworked anhydrite nodules in the Montney Formation and the age-equivalent Sulphur Mountain Formation (Zonneveld and Moslow, 2018 and reference therein). The saline brines, which would have originated from seawater, possibly mixed with some fraction of hydrothermal fluids (Liseroudi et al. 2020), advected the solutes responsible for the massive precipitation of quartz, feldspars, calcite, dolomite, ferroan-dolomite, pyrite, and anhydrite cements that account for over 30% of the rock mass in the Montney siltstone (Table 4).

Evaporated seawater also contains elevated concentration of sodium and potassium. We propose that the dolomitizing fluids also carried sufficient sodium to precipitate Na-feldspar cements and enable albitization, in accordance with models proposed by Kalsbeek (1992) and González-Acebrón et al. (2010). Increased potassium concentrations in evaporated seawater, together with potassium released by albitization of K-feldspar (Fig. 8d) would have provided solutes for the precipitation of K-feldspar cement.

5.3.3 Quartz:

The precipitation of large volumes of quartz cement is commonly considered to be triggered by temperature-dependent reactions that occur during deep burial (for example: McBride, 1989; Walderhaug, 1994; Giles et al., 2000). However, high IGV values, together with overgrowth relationships that indicate quartz cement preceded calcite cement, indicate shallow cementation. Total quartz cement concentration (first and second generations) varies between 3.5 and 11.6%, with an average of 7.4% (Table 4). Shallow (1-2 Km) quartz cementation of such volumes is documented in reservoirs world-wide (Fisher et al., 2000; Giles et al., 2000; Hartmann et al., 2000)

and attributed to feldspar dissolution, reprecipitation of dissolved siliceous skeletal grains, pressure solution, and precipitation from silica-saturated meteoric water (McBride, 1989 and reference therein; Giles et al., 2000; Worden and Morad, 2000 and reference therein).

The solubility of silica in water is very low (Williams et al., 1985 and reference therein), and improbably high volumes of water would be required to supply enough silica to precipitate the volumes of quartz cement in the Montney (Worden and Morad, 2000). There is also no indication of silica influx from neighboring mudrocks in the form of increased quartz cementation towards the top or bottom edges of the Montney. Therefore, an internal silica source for quartz cement is favored. We suggest that several internal sources combined to provide silica for the two generations of quartz cement.

Some silica was provided through in-situ dissolution and/or recrystallization of chert, although this cannot account by itself for the volumes of quartz cement in the samples. Dissolution of chert grains is readily identified through SEM imaging (Fig. 7c), and evidence for chert recrystallization is in the form of intact, euhedral quartz grains that retained some of the mottled luminescence texture of chert (Fig. 7b). Angular holes identified on the surface of quartz overgrowth (Fig. 7h) suggest the incomplete recrystallization of chert to quartz (see Hattori et al.'s (2003) study of the Miocene Kunimi Formation in Japan). Alternatively, the angular cavities in chert grains and dissolution porosity in chert may reflect decalcification of the chert (tripolitic chert; Manger, 2014).

Silt-size quartz grains themselves may have been another potential source for the quartz cement. The structure of all quartz crystals terminates in a thin layer (~100 nm) of amorphous silica (Cecil, 2004) that is much more soluble than quartz (Aase at al., 1996) and can become an important source for silica (Cecil, 2004). Experiments on mechanically abraded quartz grains demonstrated that the lattice structure of quartz is distorted to a depth of at least 15 µm, rendering the outer section of the grain metastable and relatively soluble (Cecil, 2004 and references therein). These experiments suggest that silt-size quartz grains deposited by aeolian processes,

particularly very small grains (2-3 microns) are highly reactive and can be easily dissolved, which suggests that the original detrital composition may have been more quartz-rich than at present.

Another fraction of the quartz cement may have been be sourced from biogenic silica. Reports of biogenic silica in the Montney Formation are rare. Zelazny et al. (2018) hypothesized that chert in the time-equivalent Sulphur Mountain Formation in Alberta resulted from recrystallization of concentrations of radiolarian and/or sponge spicules. In mudrocks, excess of silicon relative to aluminum indicates the presence of biogenic silica (Tribovillard et al., 2006; Ross and Bustin, 2009). Wüst et al. (2018) suggested that biogenic silica is an important component in at least 2 intervals within the Montney Formation in Alberta, based on Al/Si ratios and results from principal component analysis. However, whole rock concentrations of both aluminum and silicon in the Montney Formation are affected by the presence of large amounts of quartz and feldspars cements and authigenic clays, and in this case, increased ratio between silicon and aluminum cannot be easily used to indicate the presence of biogenic silica.

Our petrographic observations suggest that a small amount of biogenic silica is preserved in the Montney Formation in the form of silica nanospheres (Fig. 7g), interpreted to be the product of bacterial activity (Al Rajaibi et al., 2015; Milliken and Olson, 2017; Longman et al., 2019), and possible remnants of agglutinated foraminifera (Fig. 7d). Silica nanosphere cement is difficult to identify in polished Montney samples, but examination of freshly exposed surfaces under the SEM indicates that it is a minor type of silica cement. It is possible, however, that some of the biogenic silica was dissolved and incorporated into one of the generations of quartz cements.

The illitization of smectite (discussed below) also would have released large amounts of silica (Hower et al., 1976; Boles and Franks, 1979), which may have contributed to the first generation of quartz cement. Mass balance calculations assuming an initial composition of 20% smectite (appendix 2) show that illitization of smectite would have contributed 5-20% of the silica composing the first quartz cement generation.

776 Finally, some of the quartz cement originated from pressure solution (Fig. 7b, Fig. 14).
777 Pressure solution is generally associated with high temperatures during deep burial (Walderhaug,
778 1994; Bloch et al., 2002), but other studies (summarized by Makowitz and Milliken, 2003) suggest
779 that quartz dissolution is enhanced, even at low temperatures, by the presence of fractures close
780 to the dissolution front in quartz grains. However, we did not identify a clear relationship between
781 quartz microfractures and the presence of pressure solution.

782 Quartz cement volumes vary over a wide range (2 to 11 wt%) for samples with average grain
783 sizes < 20 µm. Samples with coarser grain size usually have larger cement volumes (5-12 wt%)
784 (Fig. 16a). We propose that a major control on quartz cementation is the abundance of detrital
785 clay coatings on detrital quartz grains (Fig. 7c, 9c), which inhibit quartz cementation by blocking
786 nucleation cites (Heald and Larese, 1974; Wilson, 1992). Needham et al. (2005) demonstrated
787 that clay coats can be generated through digestive processes of worms. Lithofacies in group one
788 have the highest bioturbation index (Table 2) and are thus more likely to have clay coats and
789 consequently lower quartz cement volume. It is worth noting, however, that the presence of clay
790 coats is not directly related to clay abundance. Group one samples have the lowest amount of
791 total clay and high quartz cement volume, while samples from group three have higher total clay
792 concentration but similarly high quartz cement volume. (Fig. 16b).

793 **5.3.4 Pyrite**

794 Pyrite framboids form under euxinic conditions, either in the water column or below the water-
795 sediment interface (Wilkin et al., 1996; Wilkin and Barnes, 1997; Wignall and Newton, 1998).
796 Berner (1984) and Wilkin et al. (1996) demonstrated that framboids growing in a euxinic water
797 column are generally <6 µm and are more uniform in size than framboids growing in sediment,
798 whereas crystalline pyrite is thought to develop only within the sediment itself. The wide size
799 variation in pyrite framboids observed in our samples, together with the presence of crystalline
800 pyrite suggest that pyrite precipitation occurred mostly within the sediment rather than in the water

column. Pyrite precipitation requires both iron and sulfur to be available in the pore water. Based on sulfur and oxygen isotopic composition, Liseroudi et al. (2020) postulated that a sulfur-rich fluid derived from a mix of Triassic seawater, brines sourced from Devonian evaporites in the WCSB, and in-situ anhydrite dissolution was present in the porewater of the siltstone.

5.3.5 Calcite and anhydrite cementation

Sources for calcite cement in the Montney are unclear but it has been postulated to be derived from carbonate dissolution in the underlying Permian strata (Nassichuk, 2000), possibly due to hydrothermal fluid involvement (Liseroudi et al., 2020). Our petrographic observations demonstrate only one generation of anhydrite cement, although Liseroudi et al. (2020) identified two generations of anhydrite in the Montney Formation based on sulfur isotopic compositions. Consistent with our observations, Davies et al. (1997) and Liseroudi et al. (2020) attributed all of the anhydrite cementation to early diagenesis (shallow diagenesis in this study). Based on sulfur and oxygen isotopic compositions, Liseroudi et al. (2020) suggested that the first anhydrite cement precipitated directly from Triassic seawater, whereas the later generation shows compositional similarities to underlying Devonian evaporites.

5.3.6 Illitization and albitization:

Compositional variations of MLIS clays in the Montney Formation provide additional information about the diagenetic evolution of the siltstone. Our QEMSCAN analysis results indicate that the major clay species in the Montney Formation are illite and MLIS (70-98% of total clay content), and quantitative XRD analysis determined MLIS composition to be illite (95)/ smectite (5) with insignificant swelling potential throughout most of the basin. Reports of swelling clays in the Montney are limited to the Ring-Border and Dixonville fields (Fig. 1) at the northeastern margin of the formation (Edwards et al., 1994; Zonneveld and Moslow, 2014, 2018). Quantitative XRD analysis of three samples taken from the Dixonville field (well 16, Fig. 1) confirmed the presence of MLIS with approximately 20% swelling layers (illite (80)/ smectite (20)).

826 SEM examination of freshly exposed surfaces indicated that all the clays in those samples (other
827 than kaolinite) have a detrital morphology and although they may have been chemically altered
828 from a detrital precursor, they did not precipitate in situ.

829 The occurrence of slightly swelling clays geographically near and at similar burial depth to
830 occurrences of non-swelling clays indicates that reduction of swelling potential (conversion
831 smectite to illite) of the clays in the Montney does not result from high temperatures (>90 ^{o}C), as
832 has been convincingly demonstrated for illitization of smectite in the Gulf of Mexico (Hower et al.,
833 1976; Boles and Franks, 1979). As it is unlikely that the Ring-Border and Dixonville deltas (Fig.
834 1) had a different sediment source than the rest of the formation, a different model for illitization
835 of smectite is required. We suggest that this process was a time-dependent, low temperature
836 reaction, taking place at temperatures of 60-80^{o}C, over extended period of time (10^{8} years). Such
837 a process would have required sufficient permeability to allow large volumes of water to interact
838 with the rock (Buatier, 1992; Kirsimäe et al., 1999; Moore, 2000). We propose that partially illitized
839 detrital MLIS clays were deposited as dispersed material between other matrix components. The
840 MLIS clays were further illitized to their current composition [illite (95)/ smectite (5)] over 100
841 million years following deposition, as the Montney was slowly buried to a maximum depth of
842 ~1500 m. Prolonged shallow burial maintained high porosity and permeability in the siltstone,
843 allowing large volumes of fluid to pass through the formation and interact with the available MLIS.

844 The illitization of smectite consumes potassium. Mass balance calculations based on point
845 count results (appendix 2) show that albitization (replacement of K-feldspar by Na-feldspar) would
846 have released sufficient potassium to illitize all MLIS clays in the Montney to their present-day
847 composition, similar to models developed for a number of other settings (Hower et al., 1976;
848 Morad and Aldahan, 1987; Saigal et al., 1988; Aagaard et al., 1990). Post-burial K-feldspar and
849 mica dissolution may have also contributed potassium (Moore, 2000).

850 For the most part, clays in the Montney Formation are dispersed within the matrix of hard
851 grains. The slightly swelling clays [illite (80)/ smectite (20)] in the Dixonville and Ring Border deltas

852 however were deposited mostly in several cm thick beds. The lower permeability of these beds
853 restricted fluid flow and thus potassium supply and led to the preservation of some swelling
854 potential in these clays.

855 **5.3.7 Organic matter**

856 The origin of organic matter in the Montney, whether primary (i.e., present in the siltstone at
857 the time of deposition) or the result of hydrocarbons migration, is still vigorously debated.
858 Movement of liquid hydrocarbon within the siltstone is recorded by flow structure preserved in
859 solid pyrobitumen (Chalmers and Bustin, 2012; Akai and Wood, 2014; Sanei et al., 2015; Wood
860 et al., 2015; Wood et al., 2018), but these observations have no bearing on the source of the
861 liquid hydrocarbons.

862 Some oil-to-source correlation studies concluded that oil migrated into the Montney from the
863 overlying Doig, Nordegg, and the Exshaw Formations (Riediger et al., 1990; Chatellier et al.,
864 2018; Feng et al., 2016) but others suggest that at least some hydrocarbons were generated in
865 the western section of the Montney Formation (Feng et al., 2016; Feng, personal communication).
866 However, depositional macerals have never been reported from this deeply buried western
867 section of the formation, possibly because of the high maturity that makes it is extremely difficult
868 to distinguish pyrobitumen from kerogen, if the latter is present in the rock (Lewan and Kotarba,
869 2014).

870 The presence of depositional macerals and remnant generation potential are also disputed.
871 Sanei et al. (2015) and Wood et al. (2018) noted the absence of primary macerals from their
872 samples, which varied in maturity (Ro% 0.93 to 2.08), and Sanei et al. (2015) indicated that fewer
873 than 10% of samples examined still have some generation potential. On the other hand, Romero-
874 Sarmiento et al. (2016) established the presence of vitrinite and liptinite in immature Montney
875 samples, and there are several reports of good to very good generation potential for samples with
876 immature and early mature organic matter from the Montney (Ibrahimbas and Riediger, 2004;

877 Ejezie, 2007; Chalmers and Bustin, 2012; Feng et al., 2016; Chatellier et al., 2018) that indicate
878 the presence of non-spent organic matter.

879 We did not identify any depositional macerals in our samples, and all the organic matter is
880 considered secondary in origin (i.e., migrated hydrocarbons). The massive cementation
881 documented in our study require that large volumes of water-bearing solutes flow through the
882 siltstone, and it is difficult to envision that marine organic matter will be preserved under such
883 conditions. It is possible that primary organic matter was preserved in very fine-grained intervals,
884 where flow was restricted.

885 **5.4 Late shallow burial diagenesis (eastern subcrop)**

886 Late diagenesis in the eastern section of the Montney Formation, particularly near the subcrop
887 edge (wells 15 and 16, Fig. 1), is characterized by meteoric water influence at shallow depth. The
888 effect of meteoric water is evident by the precipitation of kaolinite (Fig. 9e) and massive
889 overgrowths of quartz (Fig. 7e) and K-feldspar, together with extensive dissolution of dolomite
890 (Fig. 10d). We lack quantitative data to assess the degree of cement development for the shallow
891 Montney wells (wells 15 and 16), but QEMSCAN data show an increase in kaolinite for wells 11
892 and 15, demonstrating the effect of meteoric water on the erosional edge of the subcrop. Similar
893 observations were reported for the subcrop edge of the Brent Formation of the North Sea
894 (Osborne et al., 1994).

895 **5.5 Composition and grain size dependency of lithofacies**

896 The diagenetic pathway of a rock may be linked to its depositional environment through
897 variation in grain size and detrital composition. Grain size and composition dictate both the initial
898 porosity and permeability of a rock (Morad et al., 2010) and its compaction rate, thus controlling
899 available pore space for cementation and fluid-flow, while mineralogy and grain size influence
900 chemical reactivity during diagenesis. Here we examine the relationships between lithofacies in

the Montney Formation, grain size and detrital mineralogical composition. In addition, we consider the effects of diagenetic processes on the overall mineralogical composition of the lithofacies.

Bulk rock compositions and calculated average detrital compositions for seven lithofacies from three cores are presented in figure 6b. Detrital compositions were calculated by subtracting the percentage of cement (obtained from point count analysis) from the total content of each phase (obtained from QEMSCAN analysis). For example, lithofacies F in well two has an average of 39.2 wt% of quartz. Point count analyses (Table 4) demonstrated that 28.8% of the quartz in this facies is authigenic, while 71.2% of the quartz is detrital. The detrital quartz content for lithofacies F in well 2 is therefore 27.9 wt%. Figure 6b demonstrates that carbonate minerals exhibit the largest differences between present-day mineralogical composition and calculated detrital composition.

In terms of present-day mineralogy (Fig. 6b), lithofacies are compositionally indistinct from one another with the exception of the easternmost well (well 15). We propose that the present homogeneity is explained by little variability in the composition of deposited detrital material and the large volume of cements that precipitated during shallow burial diagenesis. These cements, which account for more than 30% of present-day rock volume (Table 4), overprinted small compositional differences in detrital grain composition between the different lithofacies in the rock.

5.6 Implications of diagenesis for reservoir quality

It is important to consider how diagenetic processes influence porosity and relative permeability, key parameters that describe reservoir quality. Locally (primarily in areas near the erosional edge of the formation), dissolution can be an important porosity-generating mechanism, but dissolution is generally a minor phenomenon in the Montney Formation and will not be discussed further.

Cementation and compaction acted together to reduced porosity and permeability in the Montney Formation, as discussed in section 5.2. Ghanizadeh et al. (2015) and Sanei et al. (2016)

926 qualitatively associated volumes of carbonate cement with grain size. The authors suggested that
927 coarser sediments retained higher porosity and permeability during earlier burial and allowed
928 higher fluid flow and larger fluxes of cementing components. Both Ghanizadeh et al. (2015) and
929 Sanei et al. (2016) referred to present day apparent grain size, which includes detrital grains and
930 cement overgrowths rather than the detrital grains present at the time of dolomite cement
931 precipitation.

932 We examined relationships between detrital quartz grain size (calculated using the equation
933 presented in Appendix 3) and cement volumes in three wells in the study area. To calculate
934 cements volumes, we assumed that average cements volumes identified in point count analysis
935 are representative for the formation. Cement volumes were calculated from QEMSCAN analyses
936 for each lithofacies in each well and the relative percentage of each cement, obtained from point-
937 count analyses. For example, point count analyses results show that dolomite cement is 53% of
938 the total dolomite for lithofacies G/H in well 2 (Table 4). Therefore, 53% of the dolomite identified
939 in QEMSCAN analysis for all samples of lithofacies G/H in well 2 was estimated to be authigenic.

940 Results of these calculations are presented in figure 16 (closed symbols) together with the
941 point count analysis results (open symbols). Note that the calculated volumes of quartz cement
942 fit reasonably well within the error of the measured data from point count analysis. No clear
943 distinction between samples from different lithofacies groups exist in any of the graphs in Fig. 16,
944 although it is possible that the large error associated with the measured detrital grain size (not
945 depicted in the figure) may mask these relationships. Fig. 16 demonstrate that no positive
946 correlation exists between detrital quartz grain size and total cement volume (Fig. 16 c) or calcite
947 cement volume (Fig. 16 d) in our samples. In fact, most samples from group one, which are the
948 coarser samples, have little to no calcite cement.

949 Our observations are consistent with findings of Chalmers and Bustin (2012) that calcite
950 cement is responsible for much of the porosity destruction in the Montney Formation (Vaisblat,
951 2020). In addition, we recognize that organic matter emplacement dramatically reduced porosity

952 in the Montney Formation and agree with the conclusion of Wood et al. (2015) that there is no
953 statistically significant correlation between porosity and TOC on a regional scale.

954 **5.7 Are siltstones unique?**

955 A comparison of compaction curves for sandstones, siltstones and mudstones (Fig. 15)
956 demonstrates that the compaction rate of clastic sediments in the upper 1.5 Km diminishes with
957 increasing grain size. At depth > 1Km, a siltstone retains higher porosity and permeability than
958 the finer grained mudstone.

959 The influences of grain size on chemical diagenesis are complex. Finer grained rocks provide
960 larger surface area of detrital minerals per unit volume, increasing the amount of nucleation sites
961 for quartz, feldspar and dolomite cementation and resulting in larger cement volumes (Ben Baccar
962 et al., 1993; Walderhaug, 1994, 1996; Lander and Walderhaug, 1999). On the other hand,
963 experiments demonstrated that quartz cement crystallization rates decrease considerably when
964 euhedral faces develop, which happens faster when the cores of detrital grains are small (Lander
965 et al., 2008). Our observations suggest that the large surface area available for cementation in
966 the Montney siltstone, combined with slower initial compaction rate (compared to clay-rich
967 mudstones) and a prolonged shallow burial allowed for enough time for quartz cement growth in
968 spite of the slow cementation rate. The prolonged shallow burial also allowed for sufficient flux of
969 fluids transporting solute that precipitated feldspar and carbonate cements. Thus, in certain burial
970 history scenarios, siltstones may be more prone to early massive cementation than sandstones
971 and mudstones.

972 The Montney Formation siltstone contains equal or lower amounts of clay and carbonate
973 minerals and more quartz and feldspar than other well-described fine-grained sediments (Fig. 17),
974 (with the exception of the Barnett and Woodford mudstones, where much of the silica is of
975 biogenic origin (Milliken et al., 2007; Dong and Harris, 2020). It is important to note that almost all
976 studies of mudstone diagenesis do not report grain size distribution, making the comparison

977 between the Montney siltstone and other mudrocks difficult. However, it is possible to compare
978 the abundance of hard grains (quartz and feldspar) and soft, malleable components (clays and
979 organic matter) between the two mudstones types. This comparison shows that the Montney
980 siltstone contains less clays and more hard grains than most mudrocks (Fig. 17).

981 Our study of the Montney Formation illustrates that a fundamental difference between
982 mudrocks and siltstones is the nature of the rock framework. Mudrocks are matrix-supported, in
983 which silt grains 'float' in an organic matter- and clay-rich matrix. In contrast, the Montney siltstone
984 has a hard grain, cement-supported framework. This difference affects compaction and thus fluid
985 flow during early burial. The resulting diagenesis leads in turn to different reservoir and
986 geomechanical properties.

987 **6. Conclusions**

988 Our results demonstrate both significant similarities and important differences between the
989 diagenetic evolution of the Montney Formation, predominantly a siltstone, and that of sandstones
990 and shales. Like shale formations, the Montney underwent substantial modification at relatively
991 shallow burial depth, but unlike shales, this modification was largely the result of massive import
992 of diagenetic components. Like sandstones, cementation of an open grain framework was
993 significant, but unlike most sandstones, the components were derived from external rather than
994 internal sources.

995 We demonstrate that most of the diagenetic processes affecting the Montney Formation
996 occurred during shallow burial (less than 1100 m). Precipitation of massive amounts of cements
997 at shallow burial depth including quartz, calcite and dolomite, overprinted minor depositional
998 variability in composition between the different lithofacies in the rock. The massive amounts of
999 shallow burial cement were related to brine reflux from updip (now eroded) parts of the Montney
1000 depositional system. This hydrologic drive, combined with an open pore system, allowed for large-
1001 scale transport of chemical components into the formation.

In the Montney Formation, and possibly in other siltstones, deep burial diagenesis plays only a minor role in the compositional evolution of the rock and appears to be limited to precipitation of fibrous illite and, possibly, to pressure solution and the precipitation of a late, secondary quartz cement phase. The limited variability of grain size and the relatively homogeneous detrital composition largely constrained diagenetic pathways, although we attribute the massive cementation to reflux of saline brines from updip lagoons, a consequence of deposition setting.

Finally, we demonstrated that the framework of silt-rich mudrocks (siltstones) differs fundamentally from that of clay-rich mudrocks (shales). Clay-rich mudrocks are fine-matrix-supported whereas the Montney siltstone has a hard-grain and cement-supported framework that was resistant to compaction, leading to different diagenetic pathways between the two rock types, and thus different porosity and permeability and different geomechanical properties.

Acknowledgments

The authors acknowledge NSERC (CRDPJ 462381 - 2013) and Energi Simulation Research Consortia in Reservoir Geomechanics for their financial support to the Reservoir Geomechanics Research Group $(RG)^2$ at the University of Alberta. We would also like to acknowledge SGS Canada for providing QEMSCAN analysis and interpretations used in this work. In addition, we thank Dr. Brian Jones, Dr. Stephen Hillier, and Dr. Eric Eslinger for their suggestions and advice in preparing this paper.

7. Reference

Aagaard, P., Egeberg, P.K., Saigal, G.C., Morad, S., Bjorlykke, K., 1990. Diagenetic albitization of detrital K-feldspars in Jurassic, Lower Cretaceous and Tertiary clastic reservoir rocks from offshore Norway; II, Formation water chemistry and kinetic considerations. Journal of Sedimentary Research, 60(4), 575-581.

Aase, N.E., Bjørkum, P.A., Nadeau, P.H., 1996. The effect of grain-coating microquartz on preservation of reservoir porosity. American Association of Petroleum Geologists Bulletin, 80(10), 1654-1673.

Adams, J.E., Rhodes, M.L., 1960. Dolomitization by seepage refluxion. American Association of Petroleum Geologists Bulletin, 44(12), 1912-1920.

Akai, T., Wood, J.M., 2014. Petrophysical analysis of a tight siltstone reservoir: Montney Formation, Western Canada. The 20th Formation Evaluation Symposium of Japan, P. 1-4.

Al Rajaibi, I.M., Hollis, C., Macquaker, J.H., 2015. Origin and variability of a terminal Proterozoic primary silica precipitate, Athel Silicilyte, South Oman Salt Basin, Sultanate of Oman. Sedimentology, 62(3), 793-825. https://doi.org/10.1111/sed.12173.

Aplin, A.C., Fleet, A.J., Macquaker, J.H., 1999. Muds and mudstones: physical and fluid-flow properties. Geological Society of London, Special Publications 158, 1-8.

Armitage, J. H., 1962. Triassic oil and gas occurrences in northeastern British Columbia, Canada. Bulletin of Canadian Petroleum Geology 10-2, 35-56.

Barber, L.M., 2002. Sedimentology, diagenesis and reservoir characterization of the Montney Formation at Sturgeon Lake South 'F' pool west-central Alberta. M.Sc. thesis, Department of Geology and Geophysics, University of Calgary, Calgary, Alberta, Canada.

BC Oil and Gas Commission, 2012. Montney Formation play atlas for NEBC.

Ben Baccar, M., Fritz, B., Made, B., 1993. Diagenetic albitization of K-feldspar and plagioclase in sandstone reservoirs: thermodynamic and kinetic modeling. Journal of Sedimentary Research, 63(6), 1100-1109. https://doi.org/10.1306/D4267CB2-2B26-11D7-8648000102C1865D.

Beranek, L.P., Mortensen, J.K., Orchard, M.J., Ullrich, T., 2010. Provenance of North American Triassic strata from west-central and southeastern Yukon: correlations with coeval strata in the Western Canada Sedimentary Basin and Canadian Arctic Islands. Canadian Journal of Earth Sciences 47, 53-73. https://doi.org/10.1139/E09-065.

Berner, R.A., 1984. Sedimentary pyrite formation: an update. Geochimica et Cosmochimica Acta, 48(4), 605-615. https://doi.org/10.1016/0016-7037(84)90089-9.

1054 Blakey, R.C., 2014. Mesozoic paleogeography and tectonic history - western North America:
1055 Triassic tectonics and paleogeography, 245 Ma. http://deeptimemaps.com/north-american-
1056 key-time-slices-series. Last accessed july 20, 2019.
1057 Bloch, S., Lander, R.H., Bonnell, L., 2002. Anomalously high porosity and permeability in deeply
1058 buried sandstone reservoirs: origin and predictability. American Association of Petroleum
1059 Geologists Bulletin, 86(2), 301-328.
1060 Boles, J.R., Franks, S.G., 1979. Clay diagenesis in Wilcox sandstones of Southwest Texas;
1061 implications of smectite diagenesis on sandstone cementation. Journal of Sedimentary
1062 Research, 49(1), 55-70.
1063 Buatier, M.D., 1992. Smectite-Illite transition in Barbados accretionary wedge sediments: TEM
1064 and AEM evidence for dissolution/crystallization at low temperature. Clays and Clay Minerals,
1065 40(1), 65-80. https://doi.org/10.1346/CCMN.1992.0400108.
1066 Bullard, J.E., Livingstone, I., 2009. Dust. In Geomorphology of Desert Environments, A.J. Parsons
1067 and A.D. Abrahams (eds.), 629-654. Springer, Dordrecht.
1068 Cao, Z., Liu, G., Zhan, H., Gao, J., Zhang, J., Li, C. and Xiang, B., 2017. Geological roles of the
1069 siltstones in tight oil play. Marine and Petroleum Geology, 83, 333-344.
1070 Caracciolo, L., Arribas, J., Ingersoll, R.V., Critelli, S., 2014. The diagenetic destruction of porosity
1071 in plutoniclastic petrofacies: the Miocene Diligencia and Eocene Maniobra formations,
1072 Orocopia Mountains, southern California, USA. Geological Scoiety of London speciasl
1073 publication, 386, 49–62. https://doi.org/10.1144/SP386.9.
1074 Cecil, C.B., 2004. Eolian dust and the origin of sedimentary chert. Open-File Report 2004-1098:
1075 US Geological Survey, 2004. Last accessed March 31, 2020.
1076 Chalmers, G.R., Bustin, M.R., 2012. Geological evaluation of Halfway–Doig–Montney hybrid gas
1077 shale–tight gas reservoir, northeastern British Columbia. Journal of Marine and Petroleum
1078 Geology, 38(1), 53-72.
1079 Chatellier, J.Y., Simpson,K., Perez, R., Tribobillard, N., 2018. Geochemically focused integrated
1080 approach to reveal reservoir characteristics linked to better Montney productivity potential.
1081 Bulletin of Canadian Petroleum Geology, 66(2), 516-551.
1082 Chilingarian, G.V., 1983. Compactional Diagenesis. In: Parker A., Sellwood B.W. (Eds.),
1083 Sediment diagenesis. NATO ASI Series (Series C: Mathematical and Physical Sciences),
1084 vol 115. Springer, Dordrecht.
1085 Clarkson, M.O., Kasemann, S.A., Wood, R.A., Lenton, T.M., Daines, S.J., Richoz, S.,
1086 Ohnemueller, F., Meixner, A., Poulton, S.W., Tipper, E.T., 2015. Ocean acidification and the
1087 Permo-Triassic mass extinction. Science, 348(6231), 229-232.

https://doi.org/10.1126/science.aaa0193.

Crombez, V., 2016 P´etrofaci`es, s´edimentologie et architecture stratigraphique des roches riches en mati`ere organique: ´etude multi-approches des formations Montney et Doig (Trias inferieur et moyen, Alberta - Colombie Britannique, Canada). PhD. Thesis, Sciences de la Terre. Universit´e Pierre et Marie Curie, Paris, France.

Crombez, V., Baudin, F., Rohais, S., Riquier, L., Euzen, T., Pauthier, S., Ducros, M., Caron, B., Vaisblat, N., 2017. Basin scale distribution of organic matter in marine fine-grained sedimentary rocks: insight from sequence stratigraphy and multi-proxies analysis in the Montney and Doig Formations. Marine and Petroleum Geology, 83: 382-401.

Crombez, V., Rohais, S., Baudin, F., Euzen, T., 2016. Facies, well-log patterns, geometries and sequence stratigraphy of a wave-dominated margin: insight from the Montney Formation (Alberta, British Columbia, Canada). Bulletin of Canadian Petroleum Geology, 64(4), 516-537.

Crouvi, O., Amit, R., Enzel, Y., Porat, N., Sandler, A., 2008. Sand dunes as a major proximal dust source for late Pleistocene loess in the Negev Desert, Israel. Quaternary Research, 70(2), 275-282.

Davies, G.R., 1997. Aeolian sedimentation and bypass, Triassic of western Canada, Bulletin of Canadian Petroleum Geology 45(4), 624–642.

Davies, G.R., Watson, N., Moslow, T.F., Maceachern, J.A., 2018. Regional subdivisions, sequences, correlations and facies relationships of the Lower Triassic Montney Formation, west-central Alberta to northeastern British Columbia, Canada - with emphasis on role of paleostructure. Bulletin of Canadian petroleum geology, 66(1), 23-92.

Davies, G.R., Moslow, T.F., Sherwin, M.D., 1997. The Lower Triassic Montney Formation, west-central Alberta. Bulletin of Canadian Petroleum Geology, 45(4), 474-505.

Dixon, J., 2000. Regional lithostratigraphic units in the Triassic Montney formation of Western Canada. Bulletin of Canadian Petroleum Geology, 48(1), 80–83.

Dong, T. and Harris, N.B., 2020. The effect of thermal maturity on porosity development in the Upper Devonian–Lower Mississippian Woodford Shale, Permian Basin, US: Insights into the role of silica nanospheres and microcrystalline quartz on porosity preservation. International Journal of Coal Geology, 217, 103346.

Ducros, M., Sassi, W., Vially, R., Euzen, T., Crombez, V., 2017. 2-D basin modeling of the Western Canada Sedimentary Basin across the Montney-Doig System: implications for hydrocarbon migration pathways and unconventional resources potential, in: AbuAli, M.A., Moretti, I., Bolås, H.M.N. (Eds.), Petroleum Systems Analysis-Case Studies: American Association of Petroleum Geologists Bulletin Memoir, 114. pp. 117-134.

https://doi.org/10.1306/13602027M1143703.

Edwards, D.E., Barclay, J.E., Gibson, D.W., Kvill, G.E., Halton, E., 1994. Triassic strata of the Western Canada Sedimentary Basin, in: Mossop, G.D., Shetsen, I. (Eds.), Geological Atlas of the Western Canada Sedimentary Basin. Canadian Society of Petroleum Geologists and Alberta Research Council, Calgary, pp. 259–275.

Ehrenberg, S.N., 1989. Assessing the relative importance of compaction processes and cementation to reduction of porosity in sandstones: reply. American Association of Petroleum Geologists Bulletin, 73(10), 1274-1276. https://doi.org/10.1306/44b4aa23-170a-11d7-8645000102c1865d.

Ejezie, N., 2007, Triassic oil families and possible source rocks, Peace River Embayment area, Alberta, Canada, Ms.C. Thesis, Department of Geology and Geophysics, University of Calgary, Calgary, Alberta, Canada.

Euzen, T., Moslow, T.F., Crombez, V., Rohais, S., 2018. Regional stratigraphic architecture of the spathian deposits in western Canada - implications for the Montney resource play. Bulletin of Canadian Petroleum Geology, 66(1), 175-192.

Feng, W., Chen, Z., Jiang, C., 2016. Oil and source correlations of Triassic Montney Formation in WCSB: implication to shale gas resource potential in: GeoConvention. CSPG CSEG CWLS, Calgary, AB, Canada, p. 1.

Ferri, F., Zonneveld, J.-P., 2008. Were Triassic rocks of the Western Canada Sedimentary Basin deposited in a foreland. Canadian Society of Petroleum Geologists Reservoir, 35(10), 12-14.

Fisher, Q.J., Knipe, R.J., Worden, R.H., 2000. Microstructures of deformed and non-deformed sandstones from the North Sea: implications for the origins of quartz cement in sandstones. Special Publication - International Association of Sedimentologists, 29, 129-146.

Flemming, B.W., 2000. A revised textural classification of gravel-free muddy sediments on the basis of ternary diagrams. Continental Shelf Research, 20(10-11), 1125-1137.

Folk, R.L., Ward, W.C., 1957. Brazos River bar [Texas]; a study in the significance of grain size parameters. Journal of Sedimentary Research, 27(1), 3-26.

Furlong, C.M., Gingras, M.K., Moslow, T.F., Zonneveld, J.-P., 2018. The Sunset Prairie Formation: designation of a new Middle Triassic formation between the Lower Triassic Montney Formation and Middle Triassic Doig Formation in the Western Canada Sedimentary Basin, northeast British Columbia. Bulletin of Canadian Petroleum Geology, 66(1), 193-214.

Ghanizadeh, A., Clarkson, C.R., Aquino, S., Ardakani, O.H., Sanei, H., 2015. Petrophysical and geomechanical characteristics of Canadian tight oil and liquid-rich gas reservoirs: I. Pore network and permeability characterization. Fuel, 153, 664-681.

https://doi.org/10.1016/j.fuel.2015.03.020.
Gibson, D.W., Edwards, D.E., 1990. An overview of Triassic stratigraphy and depositional environments in the Rocky Mountain Foothills and Western Interior Plains , Peace River Arch area , northeastern British Columbia. Bulletin of Canadian Petroleum Geology, 38(1), 146-158.
Giles, M.R., Indrelid, S.L., Beynon, G.V., Amthor, J., Worden, R.H., Morad, S., 2000. The origin of large-scale quartz cementation: evidence from large data sets and coupled heat-fluid mass transport modelling. Special Publication - International Association of Sedimentologists, 29, 21-38.
Golding, M.L., Mortensen, J.K., Ferri, F., Zonneveld, J.-P., Orchard, M.J., 2016. Determining the provenance of Triassic sedimentary rocks in northeastern British Columbia and western Alberta using detrital zircon geochronology, with implications for regional tectonics. Canadian Journal of Earth Sciences, 53(2), 140-155. https://doi.org/10.1139/cjes-2015-0082.
Golonka, J., Ford, D., 2000. Pangean (Late Carboniferous–Middle Jurassic) paleoenvironment and lithofacies. Palaeogeography, Palaeoclimatology, Palaeoecology, 161(1-2), 1-34. https://doi.org/10.1016/S0031-0182(00)00115-2.
Golonka, J., Ross, M.I., Scotese, C.R., 1994. Phanerozoic paleogeographic and paleoclimatic modeling maps, in: Embry, A.F., Beauchamp, B., Glass, D.J. (Eds.), Pangea, Global Environments and Resources. Canadian Society of Petroleum Geologist, Calgary, 1-47.
González-Acebrón, L., Arribas, J., Mas, R., 2010. Role of sandstone provenance in the diagenetic albitization of feldspars: a case study of the Jurassic Tera Group sandstones (Cameros Basin, NE Spain). Sedimentary Geology, 229(1-2), 53-63.
Harris, N.B., 1989. Diagenetic quartzarenite and destruction of secondary porosity: an example from the Middle Jurassic Brent sandstone of northwest Europe. Geology 17(4), 361. https://doi.org/10.1130/0091-7613(1989)017<0361:DQADOS>2.3.CO;2.
Hartmann, B.H., Juhász-Bodnár, K., Ramseyer, K., Matter, A., 2000. Polyphased quartz cementation and its sources: a case study from the Upper Palaeozoic Haushi Group sandstones, Sultanate of Oman. Special Publication-International Association of Sedimentologists, 29, 253-270.
Hattori, I., Umeda, M., Yamamoto, H., 2003. From chalcedonic chert to quartz chert; diagenesis of chert hosted in a Miocene volcanic-sedimentary succession, central Japan. Journal of Sedimentary Research, 66(1), 163-174.
Heald, M.T., Larese, R.E., 1974. Influence of coatings on quartz cementation. Journal of Sedimentary Research, 44(4), 1269-1274.

Hedberg, H.D., 1926. The Effect of gravitational compaction on the structure of sedimentary rocks. American Association of Petroleum Geologists Bulletin, 10(11), 1035-1072.

Henderson, C.M., Golding, M.L., Orchard, M.J., 2018. Conodont sequence biostratigraphy of the Lower Triassic Montney Formation. Bulletin of Canadian Petroleum Geology, 66(1), 7-22.

Houseknecht, D.W., 1987. Assessing the relative importance of compaction processes and cementation to reduction of porosity in sandstones. American Association of Petroleum Geologists Bulletin, 71(6), 633-642. https://doi.org/10.1306/44B4AA23-170A-11D7-8645000102C1865D.

Hower, J., Eslinger, E.V., Hower, M.E., Perry, E.A., 1976. Mechanism of burial metamorphism of argillaceous sediment: 1. Mineralogical and chemical evidence. *Geological Society of* America Bulletin, 87(5), 725.

Ibrahimbas, A., Riediger, C., 2004. Hydrocarbon source rock potential as determined by RockEval 6/TOC pyrolysis, N.E. B.C. and N.W. Alberta. Resource Development and Geoscience Branch, Summary of Activities 2004, 7-18.

Jones, G.D., Xiao, Y., 2005. Dolomitization, anhydrite cementation, and porosity evolution in a reflux system: insights from reactive transport models. AAPG bulletin, 89(5), 577-601.

Kalsbeek, F., 1992. Large-scale albitisation of siltstones on Qeqertakavsak Island, northeast Disko Bugt, West Greenland. Chemical Geology, 95(3-4), 213-233.

Kiehl, J.T., Shields, C.A., 2005. Climate simulation of the latest Permian: implications for mass extinction. Geology 33(9), 757. https://doi.org/10.1130/G21654.1.

Kirsimäe, K., Jøgensen, P., Kalm, V., 1999. Low-temperature diagenetic illite-smectite in Lower Cambrian clays in North Estonia. Clay Minerals, 34(1), 151-163. https://doi.org/10.1180/000985599546000.

Kominz, M.A., Patterson, K., Odette, D., 2011. Lithology dependence of porosity in slope and deep marine sediments. Journal of Sedimentary Research, 81(10), 730-742.

Lai, J., Wang, G., Ran, Y., Zhou, Z. and Cui, Y., 2016. Impact of diagenesis on the reservoir quality of tight oil sandstones: The case of Upper Triassic Yanchang Formation Chang 7 oil layers in Ordos Basin, China. Journal of Petroleum Science and Engineering, 145, 54-65.

Lander, R.H., Larese, R.E., Bonnell, L.M., 2008. Toward more accurate quartz cement models: the importance of euhedral versus noneuhedral growth rates. American Association of Petroleum Geologists Bulletin, 92(11), 1537-1563.

Lander, R.H., Walderhaug, O., 1999. Predicting porosity through simulating sandstone compaction and quartz cementation. American Association of Petroleum Geologists Bulletin, 83(3), 433449. https://doi.org/10.1306/00AA9BC4-1730-11D7-8645000102C1865D.

Laughrey, C.D., Ruble, T.E., Lemmens, H., Kostelnik, J., Butcher, A.R., Walker, G., Knowles, W., 2011. Black shale diagenesis: insights from integrated high-definition analyses of post-mature Marcellus Formation rocks, Northeastern Pennsylvania. *American Association of Petroleum Geologists,* Search and Discovery, Article #110150. http://www.searchanddiscovery.com/documents/2011/110150laughrey/ndx_laughrey.pdf. Last accessed March 31, 2020.

Lazar, O.R., Bohacs, K.M., Macquaker, J.H., Schieber, J., Demko, T.M., 2015. Capturing key attributes of fine-grained sedimentary rocks in outcrops, cores, and thin sections: nomenclature and description guidelines. Journal of Sedimentary Research, 85(3), 230-246.

Lewan, M.D., Kotarba, M.J., 2014. Thermal-maturity limit for primary thermogenic-gas generation from humic coals as determined by hydrous pyrolysis. American Association of Petroleum Geologists Bulletin, 98(12), 2581-2610. DOI: 10.1306/06021413204.

Liseroudi, M.H., Ardakani, O.H., Sanei, H., Pedersen, P.K., Stern, R.A., Wood, J.M., 2020. Origin of sulfate-rich fluids in the early Triassic Montney Formation, Western Canadian Sedimentary Basin. Marine and Petroleum Geology, 104236. https://doi.org/10.1016/j.marpetgeo.2020.104236.

Longman, M.W., Drake, W.R., Milliken, K.L., Olson, T.M., 2019. A comparison of silica diagenesis in the Devonian Woodford shale (Central Basin Platform, West Texas) and Cretaceous Mowry shale (Powder River Basin, Wyoming), in: W. Camp, Milliken, K., Taylor, K., Fishman, N., Hackley, P., Macquaker, J. (Eds.), Mudstone Diagenesis: Research Perspectives for Shale Hydrocarbon Reservoirs, Seals, and Source Rocks: American Association of Petroleum Geologists, Memoir 121, 49-68. https://doi.org/10.1306/13672210M12163.

Machel, H.G., 2004. Concepts and models of dolomitization: a critical reappraisal. Geological Society, London, Special Publications, 235(1), 7-63.

Macquaker, J.H., Adams, A.E., 2003. Maximizing information from fine-grained sedimentary rocks: an inclusive nomenclature for mudstones. Journal of Sedimentary Research, 73(5), 735-744.

Makowitz, A., Milliken, K.L., 2003. Quantification of brittle deformation in burial compaction, Frio and Mount Simon Formation sandstones. Journal of Sedimentary Research, 73(6), 1007-1021.

Manger, W.L., 2014. Tripolitic chert development in the Mississippian lime: new insights from SEM. In Mississippian Lime Play Forum. February 20, 2014, Oklahoma City, OK, USA.

Mason, J.A., Jacobs, P.M., Greene, R.S., Nettleton, W.D., 2003. Sedimentary aggregates in the Peoria Loess of Nebraska, USA. Catena, 53(4), 377-397.

McBride, E.F., 1989. Quartz cement in sandstones: a review. Earth-Science Reviews, 26(1-3), 69-112.

Milliken, K.L., 1989. Petrography and composition of authigenic feldspars, Oligocene Frio Formation, south Texas. Journal of Sedimentary Research, 59(3), 361-374.

Milliken, K.L., Olson, T., 2017. Silica diagenesis, porosity evolution, and mechanical behavior in siliceous mudstones, Mowry Shale (Cretaceous), Rocky Mountains, U.S.A.. Journal of Sedimentary Research, 87(4): 366-387. doi: https://doi.org/10.2110/jsr.2017.24.

Milliken, K., Choh, S.J., Papazis, P., Schieber, J., 2007. “Cherty” stringers in the Barnett Shale are agglutinated foraminifera. Sedimentary Geology, 198(3-4), 221-232.

Moore, D.M., 2000. Diagenesis of the Purington Shale in the Illinois Basin and implications for the diagenetic state of sedimentary rocks of shallow Paleozoic basins. Journal of Geology, 108(5), 553-567. https://doi.org/10.1086/314423.

Morad, S., Al-Ramadan, K., Ketzer, J.M., De Ros, L.F., 2010. The impact of diagenesis on the heterogeneity of sandstone reservoirs: a review of the role of depositional facies and sequence stratigraphy. American Association of Petroleum Geologists Bulletin, 94(8), 1267–1309. https://doi.org/10.1306/04211009178.

Morad, S., Aldahan, A.A., 1987. Diagenetic replacement of feldspars by quartz in sandstones. Journal of Sedimentary Research, 57(3), 488-493. https://doi.org/10.1306/212F8B70-2B24-11D7-8648000102C1865D.

Moslow, T.F., 2000. Reservoir architecture of a fine-grained turbidite system: Lower Triassic Montney Formation, Western Canada Sedimentary Basin, in: Weimer, P. (Ed.), Deep-Water Reservoirs of the World. SEPM Society for Sedimentary Geology, Houston, Texas, pp. 686-713. https://doi.org/10.5724/gcs.00.15.0686.

Moslow, T.F., Haverslew, B., Henderson, C.M., 2018. Sedimentary facies, petrology, reservoir characteristics, conodont biostratigraphy and sequence stratigraphic framework of a continuous (395m) full diameter core of the lower Triassic Montney Fm, northeastern British Columbia. Bulletin of Canadian Petroleum Geology, 66(1), 259-287.

Moslow, T.F., Davies, G.R., 1997. Turbidite reservoir facies in the Lower Triassic Montney Formation, west-central Alberta. Bulletin of Canadian Petroleum Geology, 45(4), 507-536.

Nadeau, P.H., Bjørkum, P.A., Walderhaug, O., 2005. Petroleum system analysis: impact of shale diagenesis on reservoir fluid pressure, hydrocarbon migration, and biodegradation risks. In Geological Society, London, Petroleum Geology Conference series, 6(1), 1267-1274.

Nassichuk, B.R., 2000. Sedimentology, diagenesis and reservoir development of the lower Triassic Montney formation, northeastern British Columbia. M.Sc. Thesis, Department of

Earth and Ocean Sciences, University of British Columbia, Vancouver, British Columbia, Canada.

National Energy Board, Government of Canada, 2013. Canada's energy future 2013 energy supply and demand projections to 2035. https://www.cer-rec.gc.ca/nrg/ntgrtd/ftr/2013/2013nrgftr-eng.pdf. Last accessed March 31, 2020.

Needham, S.J., Worden, R.H., McIlroy, D., 2005. Experimental production of clay rims by macrobiotic sediment ingestion and excretion processes. Journal of Sedimentary Research, 75(6), 1028-1037.

Ness, S.M., 2001. The application of basin analysis to the Triassic succession, Alberta Basin: an investigation of burial and thermal history and evolution of hydrocarbons in Triassic rocks. M.Sc. Thesis, Department of Geology and Geophysics, University of Calgary, Calgary, Alberta, Canada.

Nickling, W.G., Neuman, C.M., 2009. Aeolian sediment transport, In: Parsons, A.J., Abrahams, A.D., (eds.), Geomorphology of Desert Environments, 517-555. Springer, Dordrecht.

Nottebaum, V., Stauch, G., Hartmann, K., Zhang, J., Lehmkuhl, F., 2015. Unmixed loess grain size populations along the northern Qilian Shan (China): relationships between geomorphologic, sedimentologic and climatic controls. Quaternary International, 372, 151-166.

Orberger, B., Pagel, M., 2000. Diagenetic evolution of Cretaceous siltstones from drill core MAR 501 (South-Eastern France*). Journal of Geochemical Exploration*, 69, 115-118.

Osborne, M., Haszeldine, R.S., Fallick, A.E., 1994. Variation in kaolinite morphology with growth temperature in isotopically mixed pore-fluids, Brent Group, UK North Sea. Clay Minerals, 29(4), 591-608. https://doi.org/10.1180/claymin.1994.029.4.15.

Paxton, S.T., Szabo, J.O., Ajdukiewicz, J.M., Klimentidis, R.E., 2002. Construction of an intergranular volume compaction curve for evaluating and predicting compaction and porosity loss in rigid-grain sandstone reservoirs. American Association of Petroleum Geologists Bulletin, 86(12), 2047-2067.

Peng, J., Milliken, K. L., Fu, Q., Janson, X., & Hamlin, H. S., 2020. Grain assemblages and diagenesis in organic-rich mudrocks, Upper Pennsylvanian Cline shale (Wolfcamp D), Midland Basin, Texas. AAPG Bulletin, 104(7), 1593-1624.

Playter, T.L., 2013. Petrographic and x-ray microtomographic analysis of the Upper Montney Formation, Northeastern British Columbia, Canada. M.Sc. Thesis, Department of Earth and Atmospheric Sciences, University of Alberta, Edmonton, Alberta, Canada.

Polt, R.H., Krause, F.F., 1997. New discovery in the Montney Formation: Sturgeon Lake South,

Triassic F-Pool, a shoreface sandstone reservoir. Core Conference: CSPG-SEPM Joint Convention, p. 237-255.

Preto, N., Kustatscher, E., Wignall, P.B., 2010. Triassic climates - State of the art and perspectives. Palaeogeography, Palaeoclimatology, Palaeoecology, 290(1-4), 1-10. https://doi.org/10.1016/j.palaeo.2010.03.015.

Prins, M.A., Vriend, M., 2007. Glacial and interglacial eolian dust dispersal patterns across the Chinese Loess Plateau inferred from decomposed loess grain-size records. Geochemistry, Geophysics, Geosystems, 8(7).

Riediger, C.L., Fowler, M.G., Brooks, P.W., Snowdon, L.R., 1990. Triassic oils and potential Mesozoic source rocks, Peace River Arch area, Western Canada Basin. Organic Geochemistry, 16(1-3), 295–305. https://doi.org/10.1016/0146-6380(90)90049-6.

Roberts, J.M., Elmore, R.D., 2018. A diagenetic study of the Woodford Shale in the southeastern Anadarko Basin, Oklahoma, USA: Evidence for hydrothermal alteration in mineralized fractures. Interpretation, 6(1), SC1-SC13.

Rohais, S., Crombez, V., Euzen, T., Zonneveld, J.-P., 2018. Subsidence dynamics of the Montney Formation (Early Triassic, western Canada sedimentary basin): insights for its geodynamic setting and wider implications. Bulletin of Canadian Petroleum Geology, 66(1), 128-160.

Romero-Sarmiento, M.F., Euzen, T., Rohais, S., Jiang, C., Littke, R., 2016. Artificial thermal maturation of source rocks at different thermal maturity levels: application to the Triassic Montney and Doig formations in the Western Canada Sedimentary Basin. Organic Geochemistry, 97, 148-162. https://doi.org/10.1016/j.orggeochem.2016.05.002.

Ross, G.M., Gehrels, G.E., Patchett, P.J., 1997. Provenance of Triassic strata in the Cordilleran miogeocline , western Canada. Bulletin of Canadian Petroleum Geology, 45(4), 461-473.

Ross, D.J.K., Bustin, R.M., 2009. The importance of shale composition and pore structure upon gas storage potential of shale gas reservoirs. Marine and petroleum Geology, 26(6), 916-927.

Rouquerol, J., Avnir, D., Fairbridge, C.W., Everett, D.H., Haynes, J.M., Pernicone, N., Ramsay, J.D.F., Sing, K.S.W., Unger, K.K., 1994. Recommendations for the characterization of porous solids (technical report). Pure and Applied Chemistry, 66(8), 1739-1758.

Saigal, G.C., Morad, S., Bjorlykke, K., Egeberg, P.K., Aagaard, P., 1988. Diagenetic albitization of detrital K-feldspar in Jurassic, Lower Cretaceous, and Tertiary clastic reservoir rocks from offshore Norway, I. Textures and origin. Journal of Sedimentary Research, 58(6), 1003-1013.

Saller, A.H., Henderson, N., 1998. Distribution of porosity and permeability in platform dolomites: insight from the Permian of west Texas. American Association of Petroleum Geologists Bulletin, 82(8), 1528-1550.

Sanei, H., Haeri-Ardakani, O., Ghanizadeh, A., Clarkson, C.R., Wood, J.M., 2016. Simple petrographic grain size analysis of siltstone reservoir rocks: an example from the Montney tight gas reservoir (Western Canada). Fuel 166, 253-257. https://doi.org/10.1016/j.fuel.2015.10.103.

Sanei, H., Wood, J.M., Ardakani, O.H., Clarkson, C.R., Jiang, C., 2015. Characterization of organic matter fractions in an unconventional tight gas siltstone reservoir. International Journal of Coal Geology, 150-151, 296-305. https://doi.org/10.1016/j.coal.2015.04.004.

Siebert, R.M., Moncure, G.K., Lahann, R.W., 1984. A Theory of framework grain dissolution in sandstones, in: McDonald, D.A., Surdam, R.C. (Eds.), Clastic Diagenesis. The American Association of Petroleum Geologists, Tulsa, pp. 163-176. https://doi.org/10.1306/M37435.

Sobolev, S.V., Sobolev, A.V., Kuzmin, D.V., Krivolutskaya, N.A., Petrunin, A.G., Arndt, N.T., Radko, V.A., Vasiliev, Y.R., 2011. Linking mantle plumes, large igneous provinces and environmental catastrophes. Nature, 477, 312-316. https://doi.org/10.1038/nature10385.

Sun, Y., Joachimski, M.M., Wignall, P.B., Chunbo, Y., Chen, Y., Jiang, H., Wang, L., Lai, X., Yan, C., 2012. Lethally hot temperatures during the Early Triassic greenhouse. Science, 338, 366-370. https://doi.org/10.1126/science.1224126.

Sun, Y., Lu, H. An, Z., 2006. Grain size of loess, palaeosol and Red Clay deposits on the Chinese Loess Plateau: Significance for understanding pedogenic alteration and palaeomonsoon evolution. Palaeogeography, Palaeoclimatology, Palaeoecology, 241(1), 129-138.

Taylor, K. G., and Macquaker, J. H. S., 2014. Diagenetic alterations in a silt-and clay-rich mudstone succession: an example from the Upper Cretaceous Mancos Shale of Utah, USA. Clay Minerals 49(2), 213-227.

Tribovillard, N., Algeo, T.J., Lyons, T., Riboulleau, A., 2006. Trace metals as paleoredox and paleoproductivity proxies: an update. Chemical Geology, 232(1-2), 12-32. https://doi.org/10.1016/j.chemgeo.2006.02.012.

Tsoar, H., Pye, K., 1987. Dust transport and the question of desert loess formation. Sedimentology, 34(1), 139-153.

Utting, J., Zonneveld, J.-P., MacNaughton, R.B., Fallas, K.M., 2005. Palynostratigraphy, lithostratigraphy and thermal maturity of the Lower Triassic Toad and Grayling, and Montney formations of western Canada, and comparisons with coeval rocks of the Sverdrup Basin, Nunavut. Bulletin of Canadian Petroleum Geology, 53(1), 5-24. https://doi.org/10.2113/53.1.5.

Vaisblat, N., 2020. Controls on Reservoir Quality in the Lower Triassic Montney Formation. Ph.D. dissertation. University of Alberta, Department of Earth and Atmospheric Sciences, Edmonton, Alberta, Canada.

Van der Plas, L., Tobi, A.C., 1965. A chart for judging the reliability of point counting results. American Journal of Science, 263(1), 87-90.

Varga, R., Szakmány, A.G., Raucsik, B., Máthé, Z., 2005. Chemical composition, provenance and early diagenetic processes of playa lake deposits from the Boda Siltstone Formation (Upper Permian), SW Hungary. Acta Geologica Hungarica, 48(1), pp.49-68.

Walderhaug, O., 1996. Kinetic modeling of quartz cementation and porosity loss in deeply buried sandstone reservoirs. American Association of Petroleum Geologists Bulletin, 80(5), 731-745.

Walderhaug, O., 1994. Temperatures of quartz cementation in Jurassic sandstones from the Norwegian continental shelf; evidence from fluid inclusions. Journal of Sedimentary Research, 64(2a), 311-323. https://doi.org/10.1306/D4267D89-2B26-11D7-8648000102C1865D.

Wallmann, K., Aloisi, G., Haeckel, M., Tishchenko, P., Pavlova, G., Greinert, J., Kutterolf, S., Eisenhauer, A., 2008. Silicate weathering in anoxic marine sediments. Geochimica et Cosmochimica Acta, 72(12), 2895-2918.

Warren, J., 2000. Dolomite: occurrence, evolution and economically important associations. Earth-Science Reviews, 52(1-3), 1-81.

Wignall, P.B., Newton, R., 1998. Pyrite framboid diameter as a measure of oxygen deficiency in ancient mudrocks. American Journal of Science, 298(7), 537-552. https://doi.org/10.2475/ajs.298.7.537.

Wilkin, R.T., Barnes, H.L., 1997. Formation processes of framboidal pyrite. Geochimica et Cosmochimica Acta, 61(2), 323-339. https://doi.org/10.1016/S0016-7037(96)00320-1.

Wilkin, R.T., Barnes, H.L., Brantley, S.L., 1996. The size distribution of framboidal pyrite in modern sediments: An indicator of redox conditions. Geochimica et Cosmochimica Acta, 60(20), 3897–3912. https://doi.org/10.1016/0016-7037(96)00209-8.

Willett, S.D., Issler, D.R., Beaumont, C., Donelick, R.A., Grist, A.M., 1997. Inverse modeling of annealing of fission tracks in apatite; 2, Application to the thermal history of the Peace River Arch region, Western Canada sedimentary basin. American Journal of Science, 297(10), 970-1011. https://doi.org/10.2475/ajs.297.10.970.

Williams, L.A., Parks, G.A., Crerar, D.A., 1985. Silica diagenesis; I, Solubility controls. Journal of Sedimentary Research, 55(3), 301-311.

Wilson, M.D., 1992. Inherited grain-rimming clays in sandstones from eolian and shelf environments: their origin and control on reservoir properties. Origin Diagenesis and Petrophysics of Clay Minerals in Sandstones, SEPM Special Publication No. 47, 209-225.

Wilson, R. D., Chitale, J., Huffman, K., Montgomery, P., & Prochnow, S. J., 2020. Evaluating the depositional environment, lithofacies variation, and diagenetic processes of the Wolfcamp B

and lower Spraberry intervals in the Midland Basin: Implications for reservoir quality and distribution. AAPG Bulletin, 104(6), 1287-1321.

Wood, J.M., Sanei, H., Haeri-Ardakani, O., Curtis, M.E., Akai, T., 2018. Organic petrography and scanning electron microscopy imaging of a thermal maturity series from the Montney tight-gas and hydrocarbon liquids fairway. Bulletin of Canadian Petroleum Geology, 66(2), 499-515. https://doi.org/10.1038/ncomms13614.

Wood, J.M., Sanei, H., 2016. Secondary migration and leakage of methane from a major tight-gas system. Nature Communications, 7, 13614.

Wood, J.M., Sanei, H., Curtis, M.E., Clarkson, C.R., 2015. Solid bitumen as a determinant of reservoir quality in an unconventional tight gas siltstone play. International Journal of Coal Geology, 150-151, 287–295. https://doi.org/10.1016/j.coal.2015.03.015.

Worden, R., Morad, S. (Eds.), 2000. Quartz Cementation in Sandstones, Malden, MA: Blackwell Science.

Wüst, R.A., Tu, S., Nassichuk, B., Bozarth, T., Tucker, J., Cui, A., 2018. Chemostratigraphy, petrography, and SEM investigations of the Lower Triassic Montney Formation in Alberta: Implications for a new and revised diagenetic and depositional model. Bulletin of Canadian Petroleum Geology, 66(2), 436-471.

Zelazny, I.V., Gegolick, A., Zonneveld, J.-P., Playter, T., Moslow, T.F., 2018. Sedimentology, stratigraphy and geochemistry of Sulphur Mountain (Montney equivalent) Formation outcrop in south central Rocky Mountains, Alberta, Canada. Bulletin of Canadian Petroleum Geology, 66(1), 288-317.

Zonneveld, J.-P., 2011. Suspending the rules: unraveling the ichnological signature of the Lower Triassic post-extinction recovery interval. Palaios 26(11), 677–681. https://doi.org/10.2307/41317453.

Zonneveld, J.-P., Moslow, T.F., 2018. Palaeogeographic setting, lithostratigraphy, and sedimentary framework of the Lower Triassic Montney Formation of western Alberta and northeastern British Columbia. Bulletin of Canadian Petroleum Geology, 66(1), 93-127.

Zonneveld, J.-P., Moslow, T.F., 2014. Perennial river deltas of the Montney Formation: Alberta and British Columbia subcrop edge, in: Geoconvention. CSPG CSEG CWLS, Calgary, AB, Canada, pp. 1-2.

Zonneveld, J.-P., Golding, M.L., Moslow, T.F., Orchard, M.J., Playter, T.L., Wilson, N., 2011. Depositional framework of the Lower Triassic Montey Formation, West-central Alberta and Northeastern British Columbia, in: Geoconvention. CSPG CSEG CWLS, Calgary, AB, Canada, pp. 1-4.

Zonneveld, J.-P., Beatty, T.W., MacNaughton, R.B., Pemberton, S.G., Utting, J., Henderson, C.M., 2010. Sedimentology and ichnology of the Lower Triassic Montney Formation in the Pedigree-Ring/Border-Kahntah River area, northwestern Alberta and northeastern British Columbia. Bulletin of Canadian Petroleum Geology, 58(2), 115–140. https://doi.org/10.2113/gscpgbull.58.2.115.

8. Figure caption

Fig. 1: A map of the Montney Formation in Alberta and British Columbia. Insert shows the location of the Montney Formation in the Western Canada Sedimentary basin. Green Arrows show inferred directions of sediments transport into the basin. Arrow size indicates the relative importance of the sediment source. Most of the sediments were sourced from the northwestern Margin of Laurentia, positioned to the east (arrow 1). Smaller amounts of sediment came from the Inuitian orogenic wedge and the Yukon-Tanana accretionary terrain to the north (arrow 2), and from the Meosin-Muinok High to the southwest (arrow 3). A potential minor western sediment source (arrow 4) was also postulated. Most of the updip section of the Formation was eroded, but two deltas are preserved (yellow). Hexagons show location of study wells. Color-coding relates to the dataset obtained from the wells (see table 1 for more details). Full dataset includes core description, SEM and SEM-CL imaging, thin section analysis, QEMSCAN analysis on rock chips, porosity, and TOC. Map modified after Zonneveld and Moslow (2018).

Fig. 2: A chronostratigraphic chart for the Lower Triassic Montney Formation. The location of wells where mineralogy data was obtained for is marked at the top of the chart. UC is unconformity. Ages after Golding et al., 2016.

Fig. 3: Representative photograph of lithofacies identified in the four Montney Formation cores. (a) Lithofacies A - interlaminated siltstone and sandstone with current ripples. (b) Lithofacies B - massive to convolute bedded Massive sandy siltstone with carbonate concentration (in white). (c) Lithofacies C - bioturbated clay-rich siltstone. (d) Lithofacies D - mudstone with Horizontal parallel lamination (sections where lithofacies D is present are marked by arrows). (e) Lithofacies E - dolomitic siltstone. (f) Lithofacies F - faintly laminated calcareous siltstone. Arrows point to faint laminations). (g) Lithofacies G/H - laminated siltstone. (h) Lithofacies I - horizontal to irregularly laminated calcareous siltstone. (i) Lithofacies J - massive siliceous clayey siltstone. (j) Lithofacies K - massive siliceous clayey siltstone. (k) Lithofacies l -

siliceous phosphatic siltstone with phosphate nodules (highlighted in white). (l) Lithofacies M/N - bioturbated, calcareous, sandy siltstone. (m) Lithofacies O - hummocky to ripple cross-stratified sandy siltstone. (n) Lithofacies P - interbedded siliceous-mudstone and calcareous- siltstone. CR - current ripple, PL- planar lamination, B - burrow, PH - phosphate, TS - truncation surface.

Fig. 4: Cumulative grain size distribution in phi (φ) units, for all lithofacies identified in the study. Black line is the average cumulative grain size for the lithofacies. Gray area shows grain size range for all samples taken from the lithofacies. No samples were obtained from lithofacies D (mudstone). Lithofacies F (faintly laminated calcareous siltstone) is the only lithofacies where a significant difference in grain size distribution exists between samples taken from different cores.

Fig. 5: Grain size distribution of all 14 lithofacies identified in wells 2, 4, 9, and 15. (a) Group 1, mixed siltstone-sandstone lithologies (sand commonly >10%). Samples in this group have sedimentary structures indicative of higher water energy in the depositional environment such as current ripples, hummocky cross stratification, and rip-up clasts. (b) Group 2, siltstone with up to 10% sand. Samples in this group are commonly laminated. (c) Group 3, siltstone with up to 5% sand. With the exception of lithofacies P, samples in this group are massive in appearance. Letters (blue) mark the classification fields denoted by Macquaker and Adams (2003), where [a] is silt-dominated mudstone, [b] silt-rich mudstone, [c] sand-bearing, silt-rich mudstone, [d] sand and clay-bearing, silt-rich mudstone, [e] clay-bearing, silt-rich mudstone, and [m] sand and silt-bearing mudstone.

Fig. 6: QEMSCAN analysis results in wt%. QFM is the sum of quartz, K-feldspar, Na-feldspar and micaceous minerals. Clay minerals include MLIS and kaolinite, and carbonate minerals include calcite, dolomite and Fe-rich dolomite. Compositional variations between samples of different groups (a) and different lithofacies (b) are presented for the four Montney cores logged. Note the large variations in the content of carbonate minerals between samples in

all wells. Plus symbols in (b) are calculated detrital composition for several lithofacies. With the exception of well 15, lithofacies from group one have the lowest clay content. With the exception of well 15, different lithofacies and different lithofacies groups are compositionally indistinct from one another.

Fig. 7: Quartz in the Montney Formation (a) SEM CL image of detrital quartz grains (Qd), blue luminescent early quartz cement (Qc1), and red luminescent late quartz cement (Qc2); Sample 3B, well 9, 3340 m. (b) SEM-CL image of a chert fragment (Crt) with spongy texture and mottled blue and red luminescence. Note concave-convex contact of pressure solution (PS) between chert fragment and adjacent detrital quartz grain; sample 2H, well 4, 2664m. (c) SEM-EDS image of chert (Crt) with spongy texture and abundant porosity. Sample 2AE, well 4, 2621 m. (d) SEM-EDS image of agglutinated foraminifera. Sample 1AE, well 15, 864.9 m. (e) SEM-SE image of massive quartz cement overgrowth (Qog). Note clay coats inhibiting quartz cementation (white arrow), sample 1S, well 15, 876.9 m. (f) SEM-SE image of euhedral microcrystalline quartz cement (Qmc). Note lack of cement adjacent grains, where detrital clay coats are present (white arrow). (g) SEM-SE of Silica nanospheres, sample 20A, well 2, 2530 m.(h) SEM-SE image of recrystallized chert (R-Crt). Incomplete transformation of chert to quartz created holes on the face of a quartz crystal, sample 10, well 1, 2028m. (i) SEM-CL image of a fractured detrital quartz grain. Fractures are filled with blue-luminescing cement. Sample 5K, well 9, 3379 m. (j) SEM-CL image of a fractured detrital quartz grain. Fractures are filled with red-luminescing cement. Sample 3E, well 2, 2281 m. (k) SEM-CL image of fractured blue-luminescing cement. Fractures are filled with red-luminescing cement. Sample 4P, well 2, 2289 m. (l) Shattered detrital quartz cement. Many fractures are filled with red-luminescing cement. Shattered grains are rare. Sample 2AQ, well 9, 3289 m.

Fig. 8: Feldspars in the Montney Formation. (a) SEM-EDS image (left) and SEM-CL image (right) of highly luminescent detrital K-feldspar (K-frd) surrounded by a rim of non-luminescent

K-feldspar cement (K-frc), sample 4F, well 9, 3364m. (h) SEB-SE image of K-feldspar and quartz overgrowth, sample 1S, well 15, 878.5 m. (b) SEM-EDS image (left) and SEM-CL image (right) showing detrital Na-feldspar (Na-frd) and Na feldspar cement (Na-frc). Note the straight edges of the cement, sample 4F, well 9, 3364m. (c) SEM-EDS image showing discrete euhedral K-feldspar crystals (white arrows), sample 1AE, well 15, 864.9m. (d) SEM-EDS image (left), SEM BSC (center), and SEM-CL image (right) of luminescent detrital K-feldspar (K-frd) and non-luminescent authigenic Na-feldspar replacing the detrital grain (Na-frr), sample 2AQ, well 4, 3289.05 m. (e) SEM-EDS image (left) and SEM-CL image (right) of highly luminescent detrital Na-feldspar (Na-frd) and non-luminescent authigenic Na-feldspar replacing the detrital grain (Na-frr). Note K-feldspar cement (K-frc) overgrowing Na-feldspar, sample 1C, well 9, 3278m. (f) SEM-EDS image of dissolution at the boundary between detrital grain and cement rim of K-feldspar, sample 1C, well 9, 3278m.

Fig. 9: Mica and clay minerals in the Montney Formation. (a) SEM-EDS image of chlorite (Mg-rich mica). Note split grain edges, sample 16I, well 2, 2487m. (b) SEM-BS image of deformed (green arrow) and dissolved (yellow arrow) mica grain, sample 10D, well 2, 2396 m. (c) SEM-SE image of detrital clay coats around a detrital quartz grain, sample, 7C, well 2, 2342.1 m. (d) SEM-BS image of a clay clump (white arrows) between detrital grains. White minerals are pyrite; sample 9P, well 2, 2366.25 m. (e) SEM-SE image of authigenic pore lining kaolinite, sample A, well 16, 875.55 m. (f) SEM-SE image of pore bridging fibrous illite, developing on detrital clay, sample 1, well 1, 2006 m.

Fig 10: Carbonate minerals. Thin section photomicrograph showing euhedral dolomite cement (Dc) surrounding a detrital dolomite (Dd) core. Note pyrite (Py) inclusions in the dolomite cement, sample 1AC, well 15, 867 m. (b) SEM-EDS (left) and SEM-CL (blue channel, right) of detrital dolomite (Dd), surrounded by dolomite cement (Dc) and Fe-rich dolomite cement (Fe-Dc). Small dissolution pits (yellow arrows) are present in the detrital dolomite,

sample 16I, well 2, 2487 m. (c) SEM-CL image showing detrital dolomite and cement. Outer rim is composed of non- luminescent Fe-dolomite. Fe-dolomite cement is replacing earlier dolomite cement with bright blue luminescence (yellow arrows), sample 3AJ, well 4, 2653 m. (d) Large dissolution vuggs in dolomite (in both detrital well and cement), sample 1AE, well 15, 864.9 m. (e) Poikilotopic calcite cement in SEM-EDS image. Sample 3AJ, well 4, 2653 m.(f) SEM-EDS image showing calcite filling pores left by dissolution of detrital dolomite, sample 3E, well 2, 2281 m. (g) SEM-EDS (left) and SEM-CL (right) showing two generations of calcite. The first calcite cement generation (Ca_1) contains euhedral pyrite inclusions and has bright luminescence. The second calcite cement generation (Ca_2) crystallized around Ca_1, has darker, more muted blue luminescence pattern than Ca_1. (h) Moldic porosity in dolomite cement, sample 170803, well 13, 1960.5 m. (i) Phosphate replacing fossils, sample 2AE, well 4, 2621 m.

Fig. 11: Organic matter and minor mineral phases in the Montney Formation. (a) BS-SEM image of pyrite framboids and pyrite crystals (white) within the siltstone matrix. Note abundant organic matter (OM) plugging pores. Sample,3A, well 2, 2285 m. (b) SE-SEM image of a pyrite framboids coated in detrital clay. Clay coats suggest pyrite framboids were transported from the original site of precipitation, sample 6, well 1, 1986 m. (c) QEMSCAN image of bedding -parallel anhydrite (pink color), sample 3B, well 9, 3340 m. (d) QEMSCAN image showing phosphatic nodules (salmon color), sample 170940, well 10, 1794.5 m. (e) EDS- SEM image showing (1) phosphate incorporated into dolomite (white arrow), and (2) phosphate precipitating at the boundary of a dolomite grain (white arrow), together with pyrite (white crystals) ,sample 3E, well 2, 2281 m. (f) BSE-SEM image showing organic matter (red arrows) filling secondary porosity in dolomite. Blue arrows point to pores which show darker on BSE images. Sample 1AE, core 15, 864.9 m.

Fig. 12: Macroporosity values obtained from QEMSCAN analysis (pores > 4.8) and matrix porosity (pores> 0.31 Å). Matrix porosity is consistently higher than porosity measured through

QEMSCAN analysis indicating that a large fraction of the pores in the samples consists of micropores, smaller than 4.8 μm.

Fig. 13: Paragenetic sequence for the Montney Formation. Burial diagram adopted from well C-70-B/93-P-9 of Ducros et al. (2017). (a) Detrital component slightly dissolved on seabed include dolomite, feldspars and chert (b) Process continues in the deep section of the basin when temperatures are currently 100^{o}C or higher (c) Albitization (d) Process developed only in the shallow section of the basin.

Fig. 14: Pressure solution in Montney samples. (a) SEM-EDS image (left) and SEM-CL image (right) of pressure solutions (white arrow) between a detrital quartz grain (Qd) and quartz cement (Qc). Sample 5N, well 9, 3376m. (b) SEM-EDS image (left) showing quartz grains with morphology that resembles pressure solution (white arrow). SEM-CL image (right) confirms pressure solution between two detrital quartz grains (Qd). Sample 2AQ, well 9, 3289 m.

Fig. 15: Porosity/ IGV depth plot for silt-rich sediment (black line), clean, well-sorted sandstone (blue line), and shale (red line). The rate of mechanical compaction is the main control over porosity reduction with depth, but cement halts compaction. If cement is present, the IGV value can indicates the depth of cementation.

Green arrows show the cementation depths of three samples from the Montney siltstone. (a) sample depth is 2653 m, but an IGV of 52% indicates cementation occurred at ~150 m depth (sample 3AJ, well 4). (b) sample depth is 3278 m, but an IGV of 40% indicates cementation occurred at 500 m depth (sample 1C, well 9). (c) sample depth is 2739 m, but an IGV of 27.6% indicates cementation occurred at 1000 m depth (Sample 5V, well 4). Samples with IGV > 60% (initial porosity) could not be placed on the compaction graph. Such high IGV value suggests that a portion of the detrital grains was dissolved or that the initial porosity is larger than 60%.

Fig. 16: calculated (close symbols) and measured (open symbols) detrital quartz grain size versus different cements for the three lithofacies groups in the Montney formation. Cement volumes were calculated from QEMSCAN analysis results based on the average cement content of each mineral per facies, obtained from point count analysis (Table 4). Note that the calculated volumes of quartz cement fit reasonably well within the error of the measured data from point count analysis. No clear distinction between samples from different groups exist in any of the graphs although it is possible that the large error associated with the measured detrital grain size (not depicted in the figure) may be masking such correlations. (a) Quartz cement volume versus detrital quartz grain size. Quartz cement volume vary greatly for any given grain size, suggesting that detrital grain size is not the main factor controlling the volume of quartz cement. (b) Quartz cement versus clay content. Samples from lithofacies group one have the lowest amount of clay and high quartz cement volume, and samples from lithofacies group three have higher clay concentration but similarly high quartz cement volume, demonstrating that higher clay concentration in the matrix does not equate more extensive clay coats on detrital grains. Lithofacies in group one have the highest bioturbation index and thus the highest probability to have clay coats generated through bioturbation. Respectively, samples from this group have the lowest volume of quartz cement. Here too, it is possible that the large error associated with the measured detrital grain size may be masking a correlation between the volume of quartz cement and clay content. (c) Detrital quartz grain size and total cements volume. Total cements volume includes quartz, feldspar, dolomite, calcite, anhydrite, pyrite, halite and phosphate. No correlation exists between detrital quartz grain size and dolomite cement or total cement volume. (d) Detrital quartz grain size and calcite cements. No correlation exists between detrital quartz grain size and calcite cement. Most samples from group one which have the largest grain size, have the lowest amount of calcite cement.

Fig. 17: Mineralogical composition of the Montney Formation (black diamonds, gray envelope) compared to various shale formations (after Chermak and Schreiber, 2014). The Montney Formation is most similar to the Barnett (blue rectangles, till envelope), but contains similar or lower clay concentrations, and for the most part less carbonate minerals than other shales.

9. Tables:

Table 1: Data set summary

Table 2: A summary of all lithofacies characteristics in four Montney core

Table 3: Grain size statistical parameters of all lithofacies

Table 4: Point count analysis results

Appendix 1: Core description for the four cored wells.

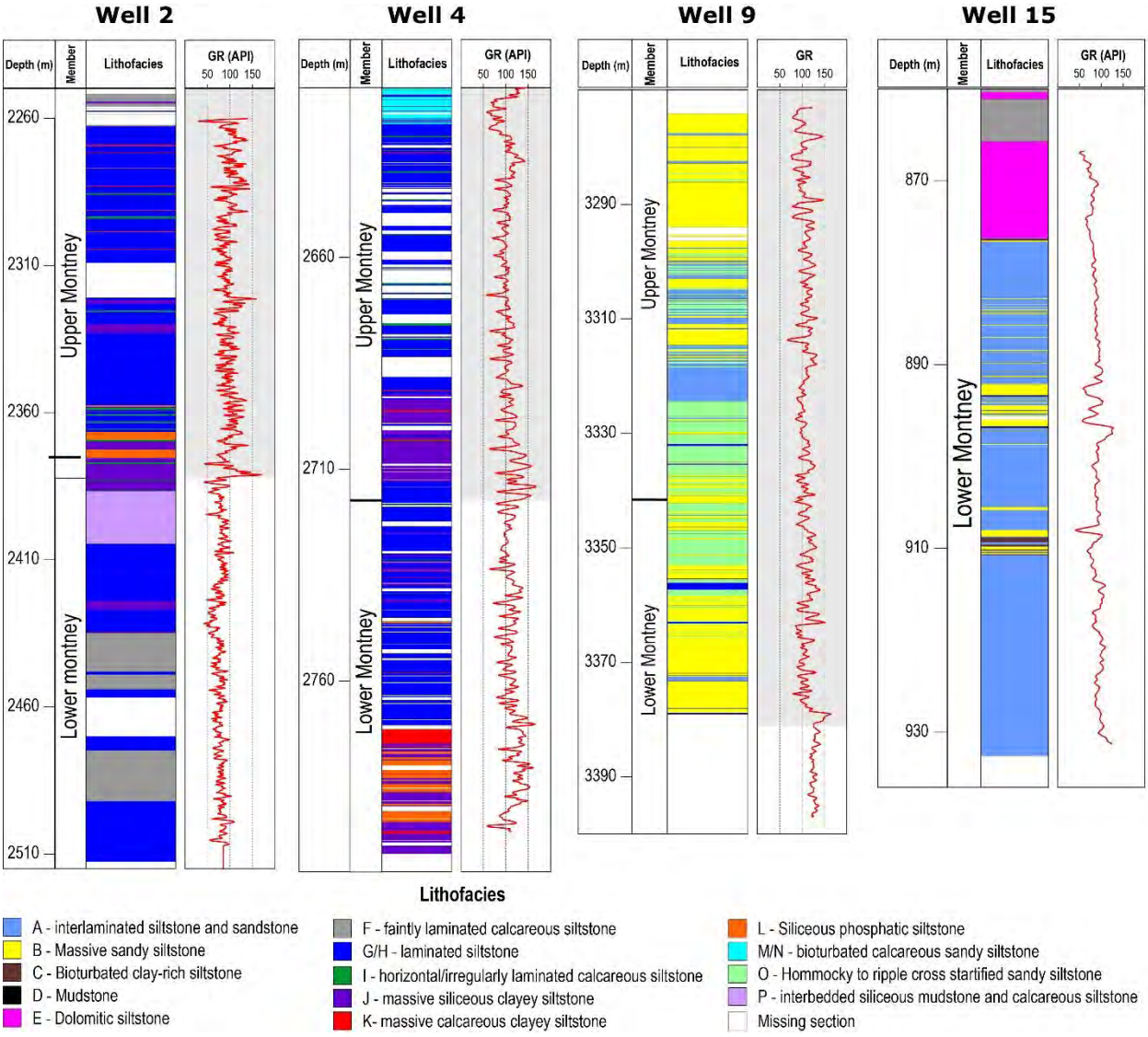

Appendix 2: Mass balance calculations for smectite to illite reaction in the Montney Formation. Also included are the amount of K-feldspar albitization and silica liberated during smectite illitization.

		well						
	unit	2	3	4	5	9	11	15
Average MLIS content[a]	gr	15.19	11.18	16.58	11.66	5.71	13.96	14.18
Smectite content [b]	gr	2.28	1.68	2.49	1.75	0.86	2.09	2.13
Smectite content [b]	moles	5.66E-04	4.16E-04	6.17E-04	4.34E-04	2.13E-04	5.20E-04	5.28E-04
Illite generated[b,c]	moles	3.60E-04	2.65E-04	3.93E-04	2.76E-04	1.36E-04	3.31E-04	3.36E-04
K+ needed to create the illite[c]	moles	1.42E-03	1.04E-03	1.55E-03	1.09E-03	5.33E-04	1.30E-03	1.32E-03
Average Na-feldspar concentration[a]	gr	8.87	6.64	8.94	6.65	9.82	3.44	2.33
Albitized K-feldspar[d]	gr	1.12	0.84	1.13	0.84	1.24	0.43	0.29
K+ released by Na-feldspar albitization[e]	moles	4.26E-03	3.19E-03	4.29E-03	3.19E-03	4.72E-03	1.65E-03	1.12E-03
Access of K+ [f]	moles	2.85E-03	2.15E-03	2.75E-03	2.11E-03	4.19E-03	3.52E-04	-2.01E-04
Si released through illitization[c,g]	moles	8.89E-03	6.54E-03	9.70E-03	6.82E-03	3.34E-03	8.16E-03	8.30E-03
SiO_2 precipitated[c]	gr	0.53	0.39	0.58	0.41	0.20	0.49	0.50

All calculations done for 100 gr of rock.

[a]concentration from QEMSCAN analysis.

[b]concentration of detrital smectite assuming original composition of illite (80)/smectite (20) and final composition of illite (95)/ smectite (5).

[c]according to molar ratios from Eq.1.

[d]according to point count analysis albitized Kspar is 12.6% of total Na-feldspar.

[e]K+ released by Na-feldspar albitization is equal to Na^+ consumed by the albitization reaction.

[f] K+ released by Na-feldspar albitization and not consumed by conversion of smectite to illite.

[g] Silica released by smectite to illitization.

Appendix 3: Correlation between average quartz mineral size measured through QEMSCAN analysis and average detrital quartz grain size measured from SEM-images.

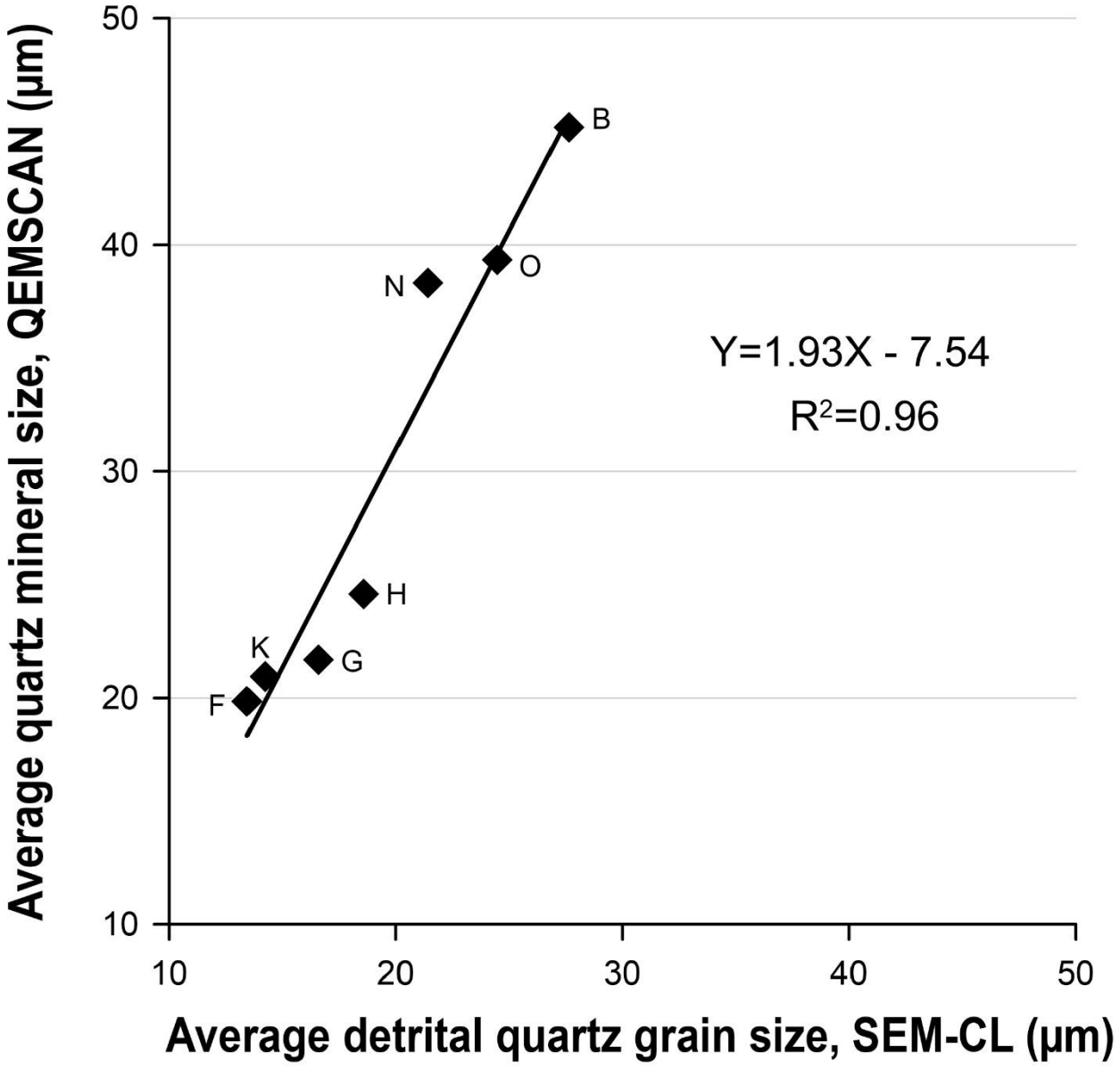

Appendix 4: Rock composition and Mineral size from QEMSCAN analysis for seven wells in the Montney Formation. Dark gray area shows results between P_5 and $P9_5$., light gray areas are the upper and lower 5^{th} percentiles (minimum and maximum), and the dashed line is the median value.

For graphs depicting minerals content, point count averages (full circles), and XRD ranges and average compositions (diamonds, error bars) are superimposed on QEMSCAN results and show good agreement. (a) Quartz content (c) K-feldspar (e) Na-feldspar (g) mica (i) Calcite (k) dolomite (m) total clay content; no XRD results are presented, since XRD analysis cannot distinguish between muscovite and illite. (n) kaolinite content (o) total organic carbon content.

Mineral size was obtained from QEMSCAN analysis. (a) Quartz; Circles are average detrital quartz grain size obtained from SEM-CL analysis (d) K-feldspar (f) Na-feldspar (h) mica (j) Calcite (l) dolomite.

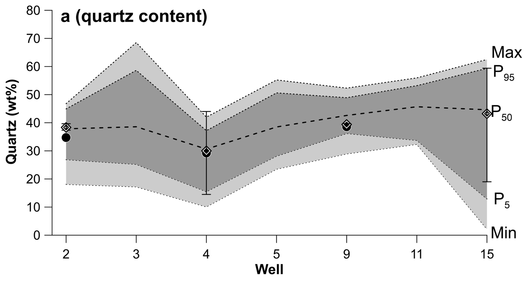
a (quartz content)
Quartz (wt%)
Max
P95
P50
P5
Min
Well

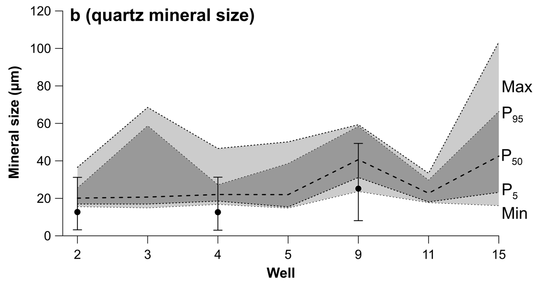
b (quartz mineral size)
Mineral size (µm)
Max
P95
P50
P5
Min
Well

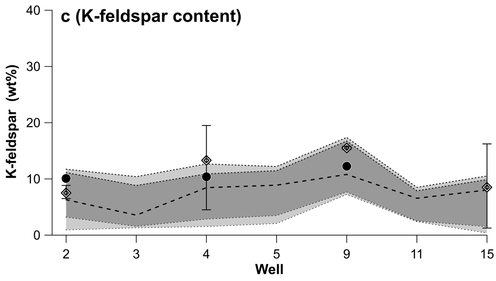
c (K-feldspar content)
K-feldspar (wt%)
Well

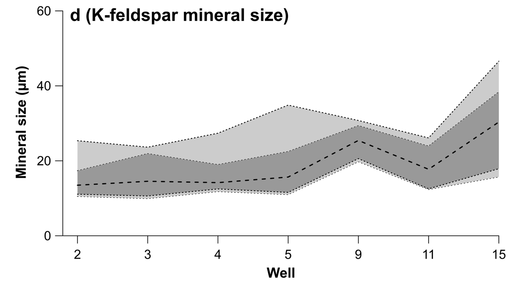
d (K-feldspar mineral size)
Mineral size (µm)
Well

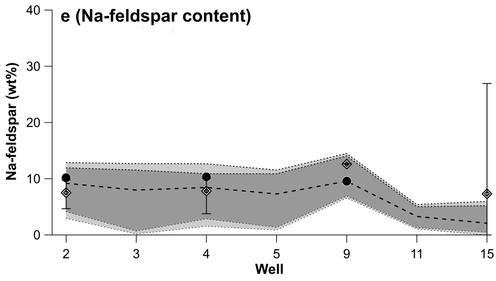
e (Na-feldspar content)
Na-feldspar (wt%)
Well

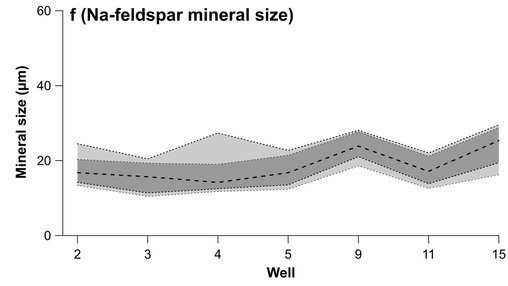
f (Na-feldspar mineral size)
Mineral size (µm)
Well

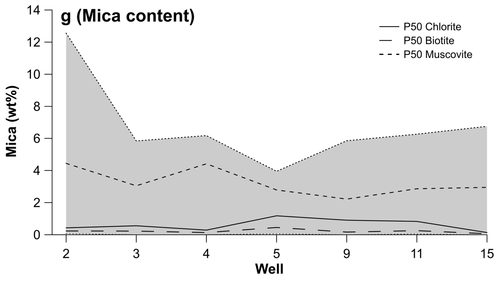
g (Mica content)
P50 Chlorite
P50 Biotite
P50 Muscovite
Mica (wt%)
Well

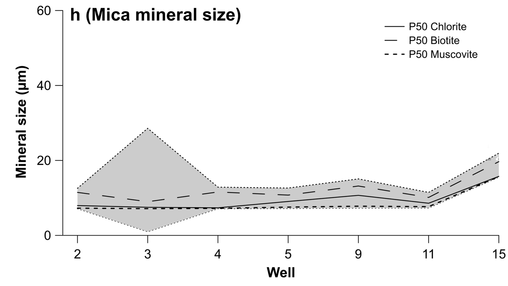
h (Mica mineral size)
P50 Chlorite
P50 Biotite
P50 Muscovite
Mineral size (µm)
Well

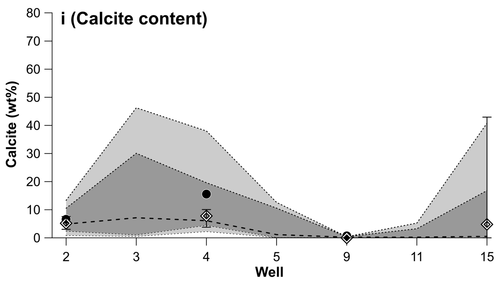
i (Calcite content)
Calcite (wt%)
Well

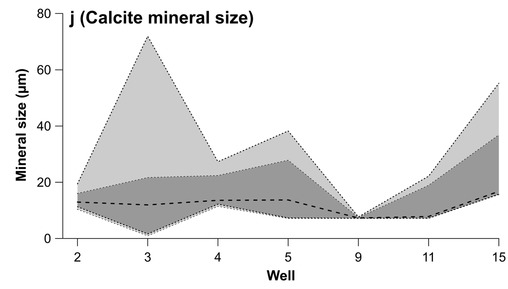
j (Calcite mineral size)
Mineral size (µm)
Well

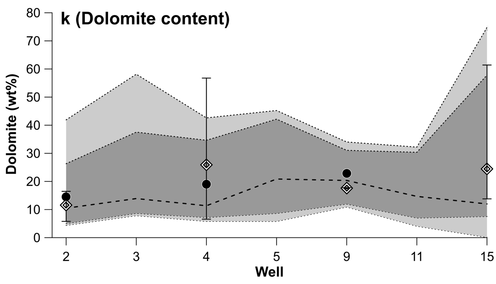
k (Dolomite content)
Dolomite (wt%)
Well

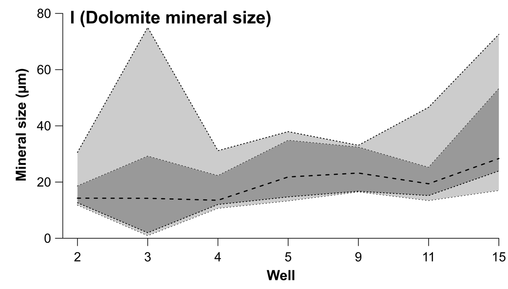
l (Dolomite mineral size)
Mineral size (µm)
Well

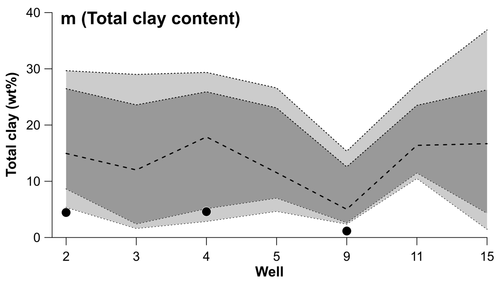
m (Total clay content)
Total clay (wt%)
Well

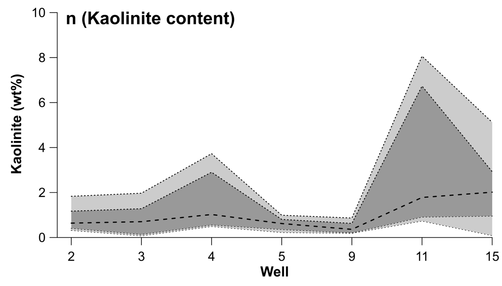
n (Kaolinite content)
Kaolinite (wt%)
Well

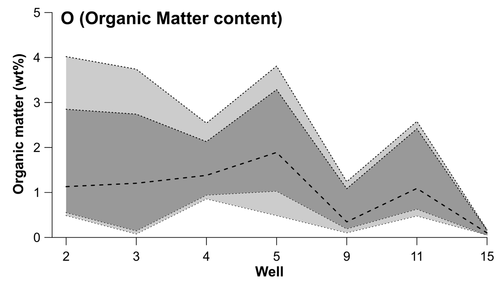
O (Organic Matter content)
Organic matter (wt%)
Well

122°W
120°W
118°W
116°W
58°N
56°N
54°N
British Columbia
Alberta
Yukon
Northwest Territories
WCSB
Alberta
British Columbia
US
0 150 300 Kilometres
Ring-Pedigree delta
Dixonville delta
Deformation front
Meosin-Muinok High
1
2
3
4
?
SEM images, XRD
Core, full dataset
QEMSCAN (cuttings)
Thin sections
0 50 100 150
Km

Relative location of study wells

1 2 3 4 5 7 9 11 15

Systems	Series	Stage
Jurassic	Lower 201.3 Ma	Pliensbachian
		Sinemurian
		Hettangian
Triassic	Upper 237 Ma	Rhaetian
		Norian
		Carnian
	Middle 247.2 Ma	Ladinian
		Anisian
	Lower 252 Ma	Olenekian
		Induan
Permian	Lopoingian	Changhsingian
		Wuchiapingian
	Guadalupian	Capitanian

West — British Columbia — Alberta — East

Nordegg

Sub Jurassic UC

Pardonet

Baldonnel

Charlie Lake

Coplin UC

Halfway

Doig

Sunset Prairie

Montney

Belloy

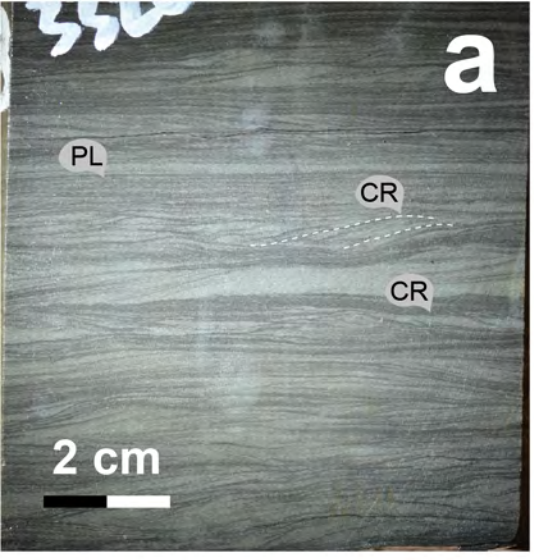
a
PL
CR
CR
2 cm

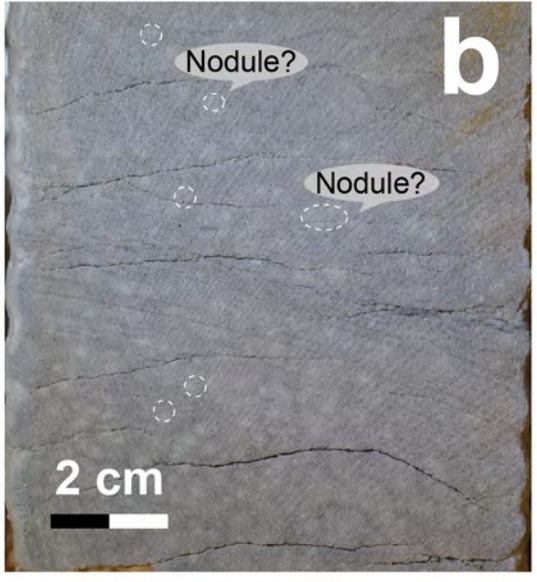
b
Nodule?
Nodule?
2 cm

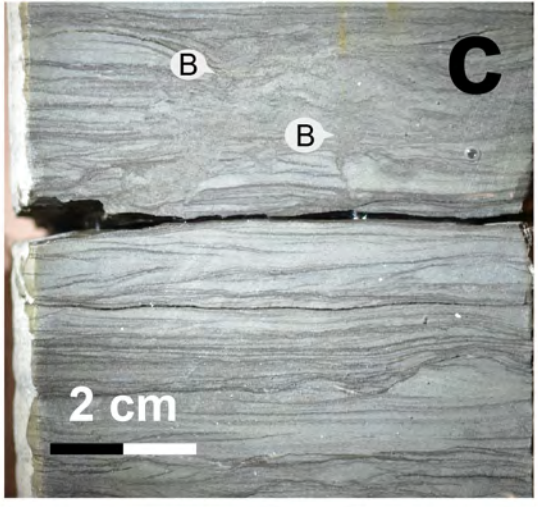
c
B
B
2 cm

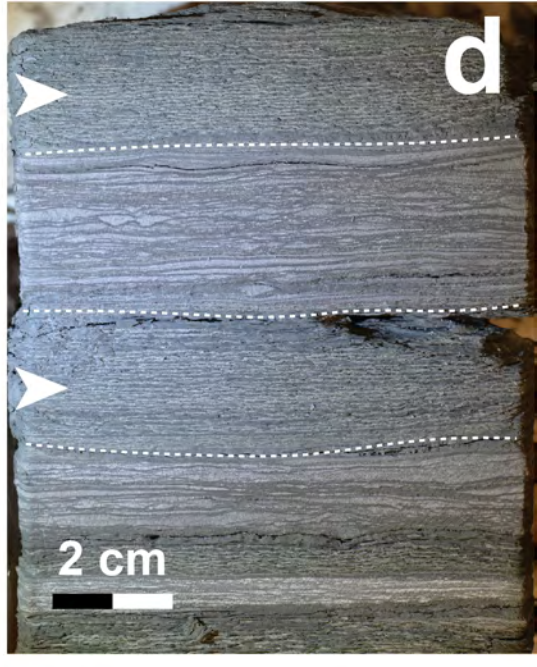
d
2 cm


e
2 cm

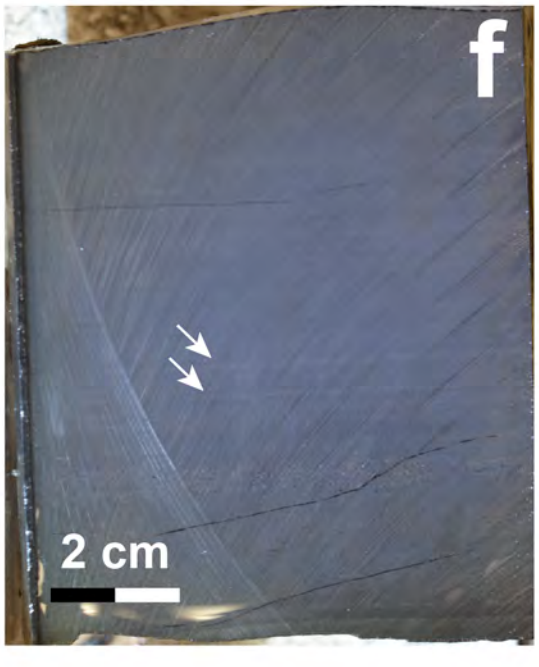
f
2 cm

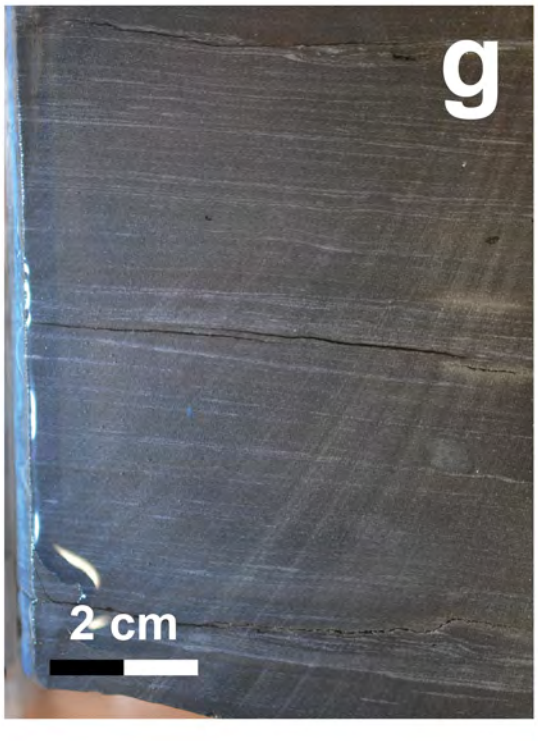
g
2 cm

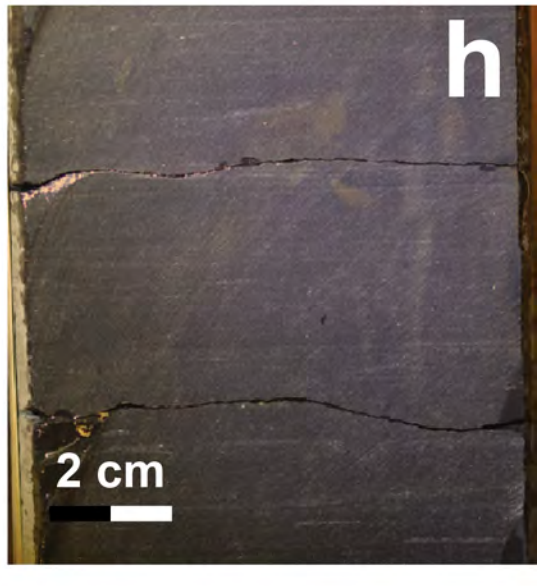
h
2 cm

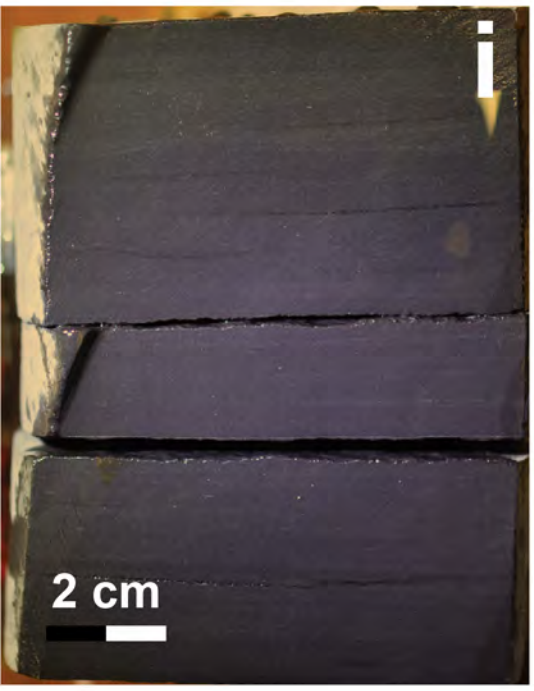
i
2 cm


j
2 cm

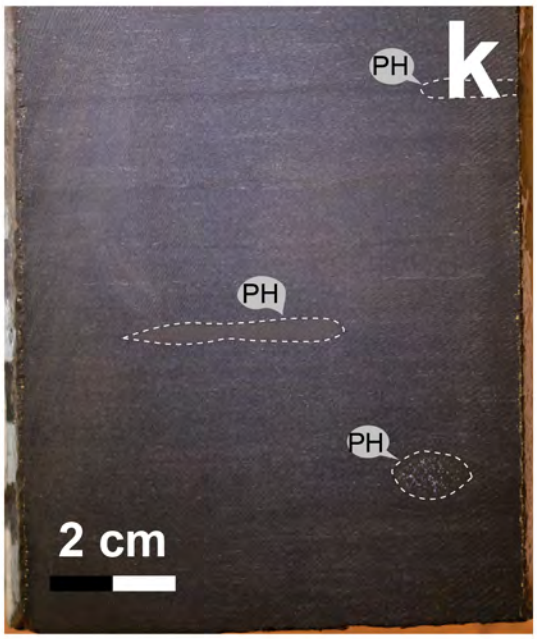
PH
k
PH
PH
2 cm

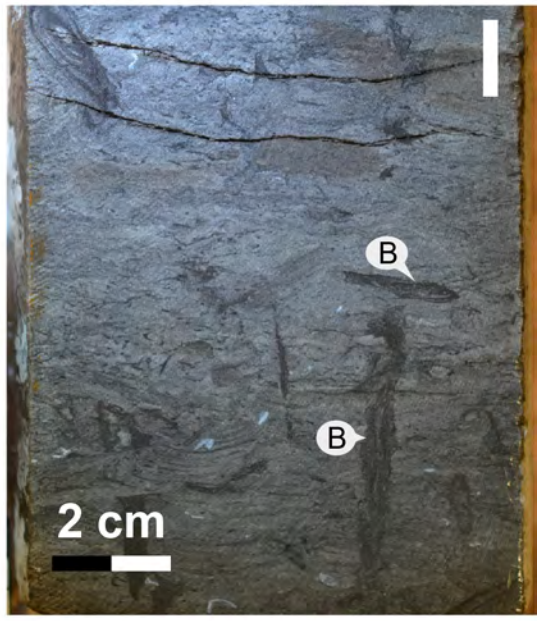
l
B
B
2 cm

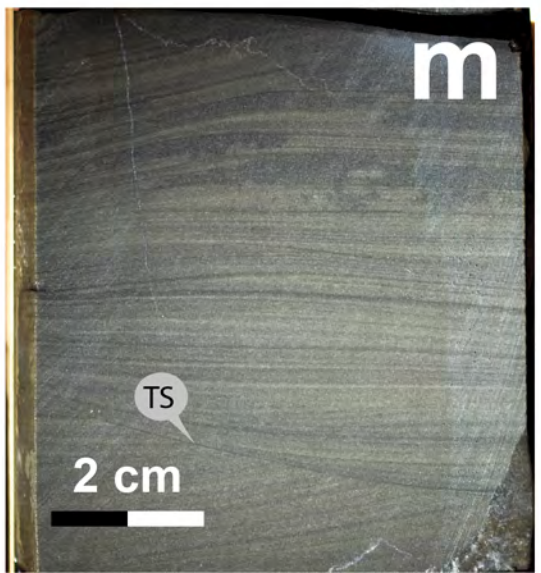
m
TS
2 cm

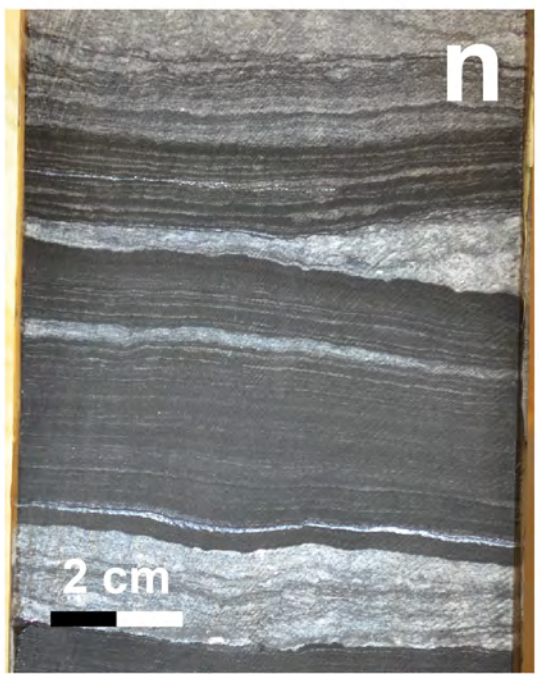
n
2 cm

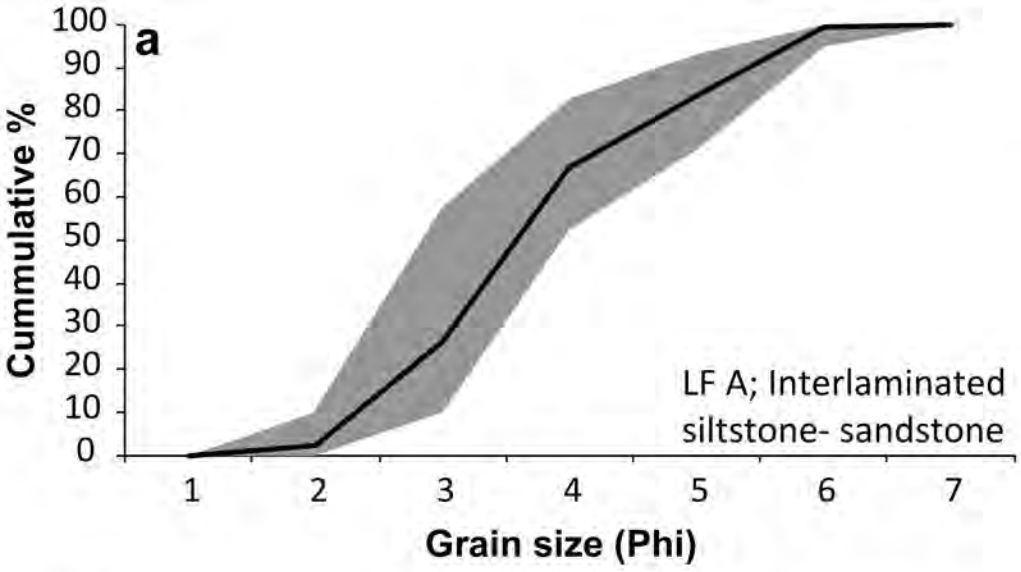
a
Cummulative %
Grain size (Phi)
LF A; Interlaminated siltstone- sandstone

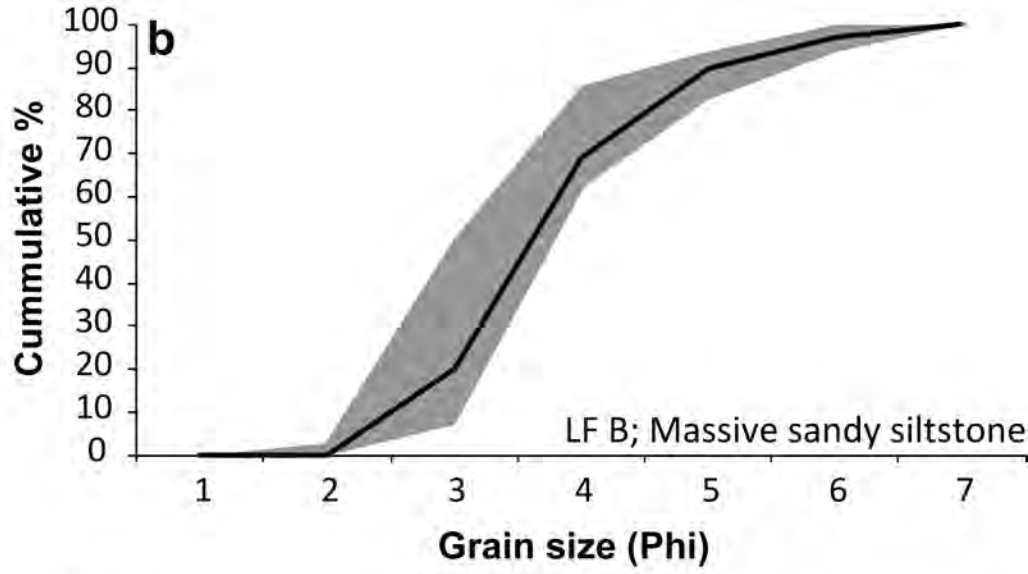
b
Cummulative %
Grain size (Phi)
LF B; Massive sandy siltstone

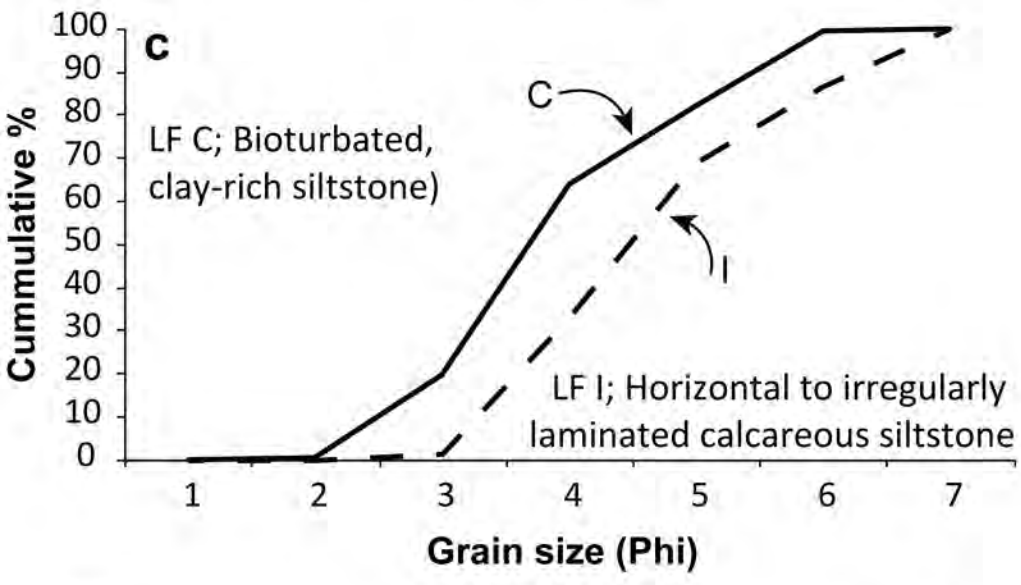
c
Cummulative %
Grain size (Phi)
LF C; Bioturbated, clay-rich siltstone)
C
I
LF I; Horizontal to irregularly laminated calcareous siltstone

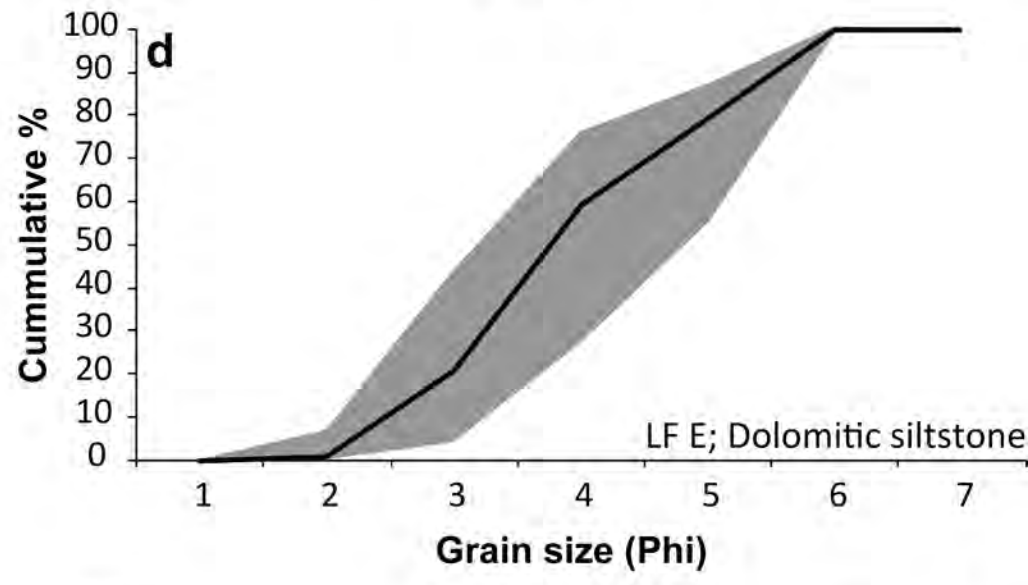
d
Cummulative %
Grain size (Phi)
LF E; Dolomitic siltstone

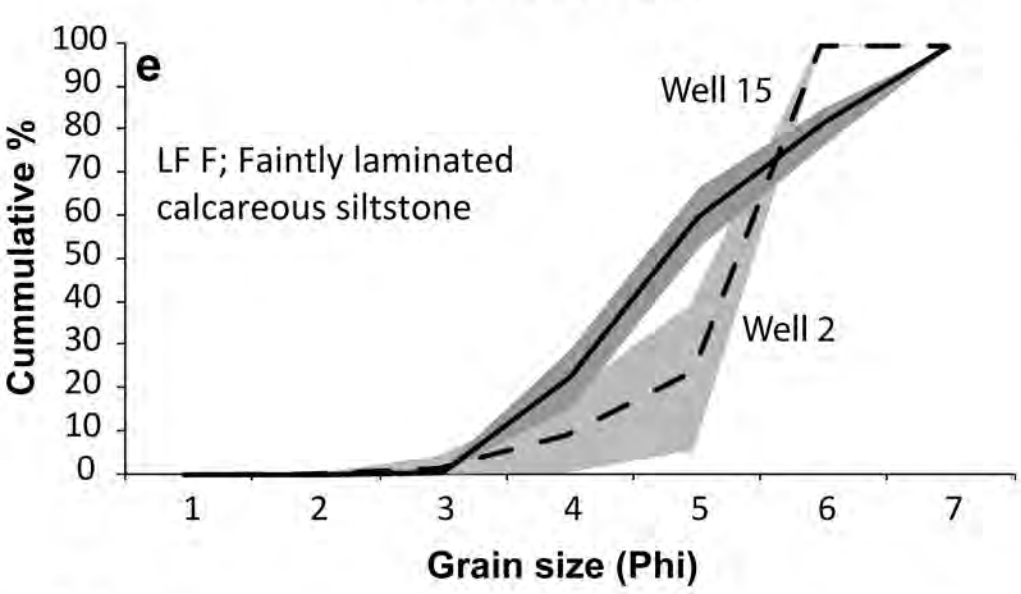
e
Cummulative %
Grain size (Phi)
LF F; Faintly laminated calcareous siltstone
Well 15
Well 2

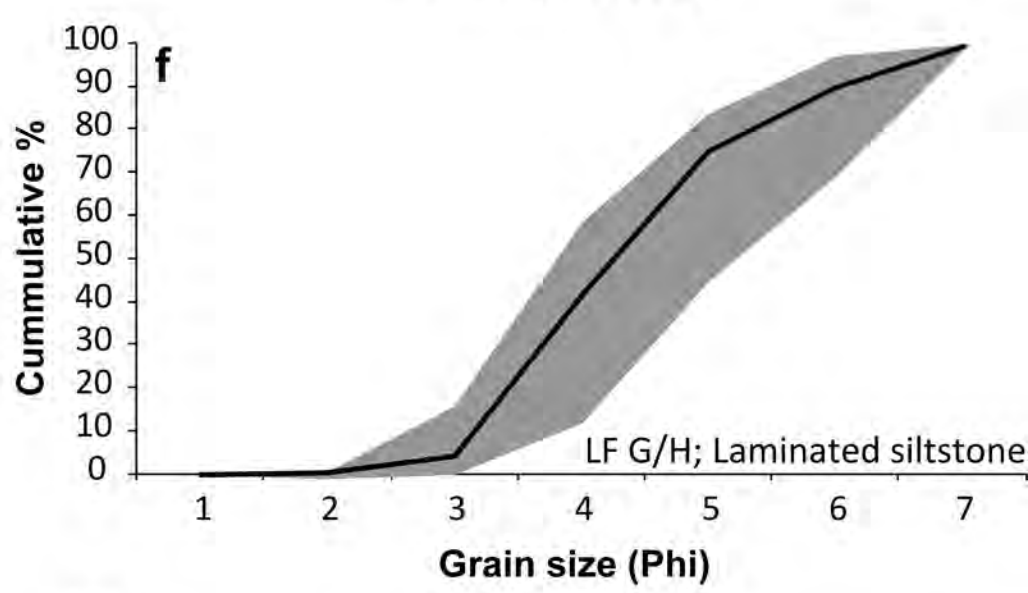
f
Cummulative %
Grain size (Phi)
LF G/H; Laminated siltstone

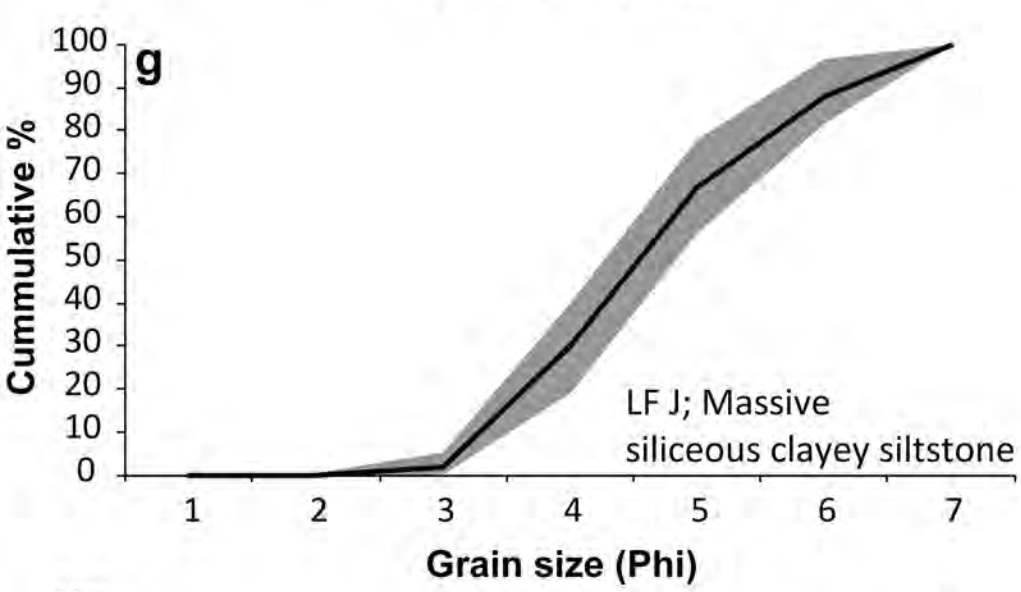
g
Cummulative %
Grain size (Phi)
LF J; Massive siliceous clayey siltstone

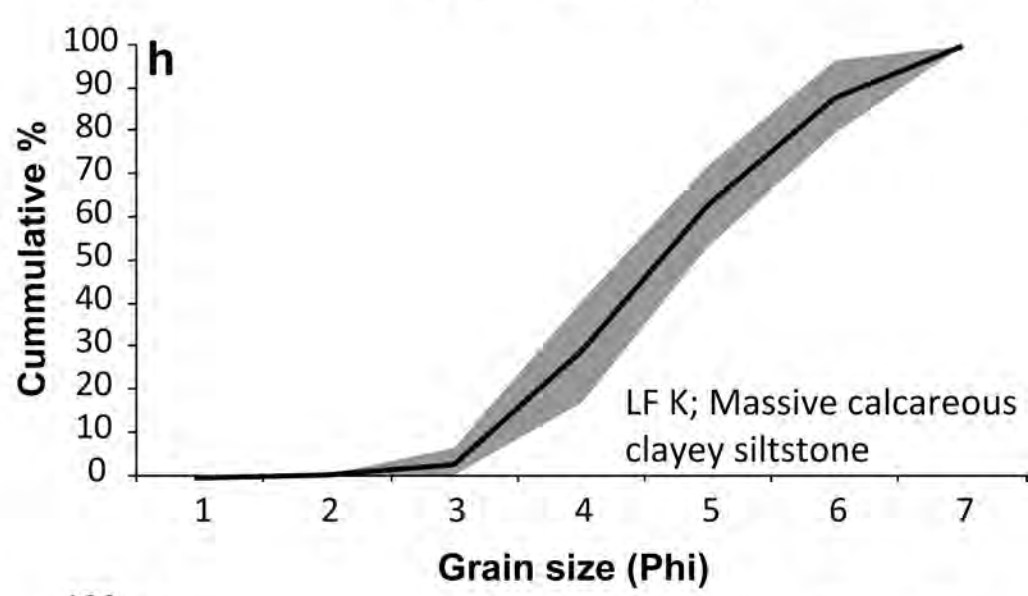
h
Cummulative %
Grain size (Phi)
LF K; Massive calcareous clayey siltstone

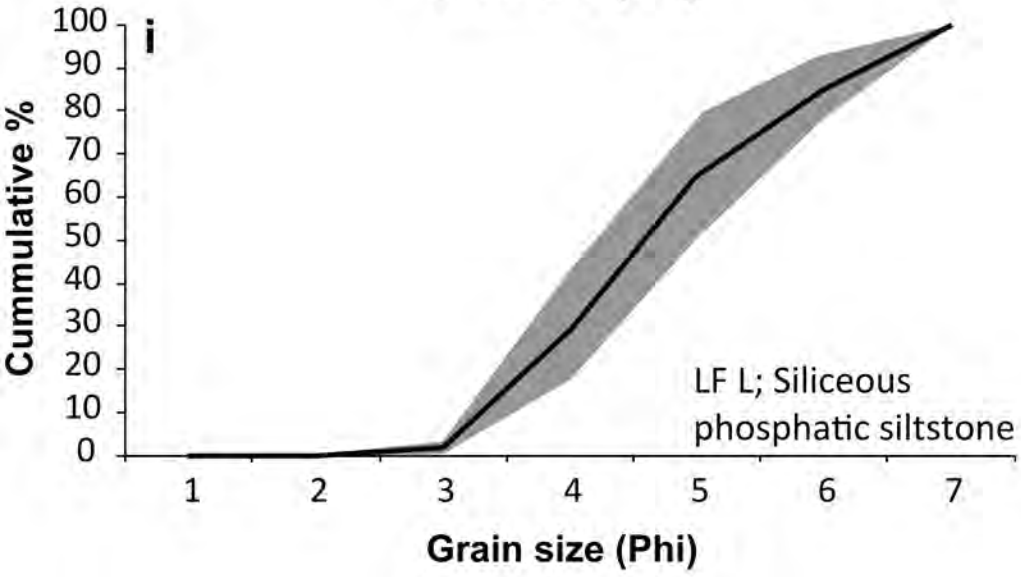
i
Cummulative %
Grain size (Phi)
LF L; Siliceous phosphatic siltstone

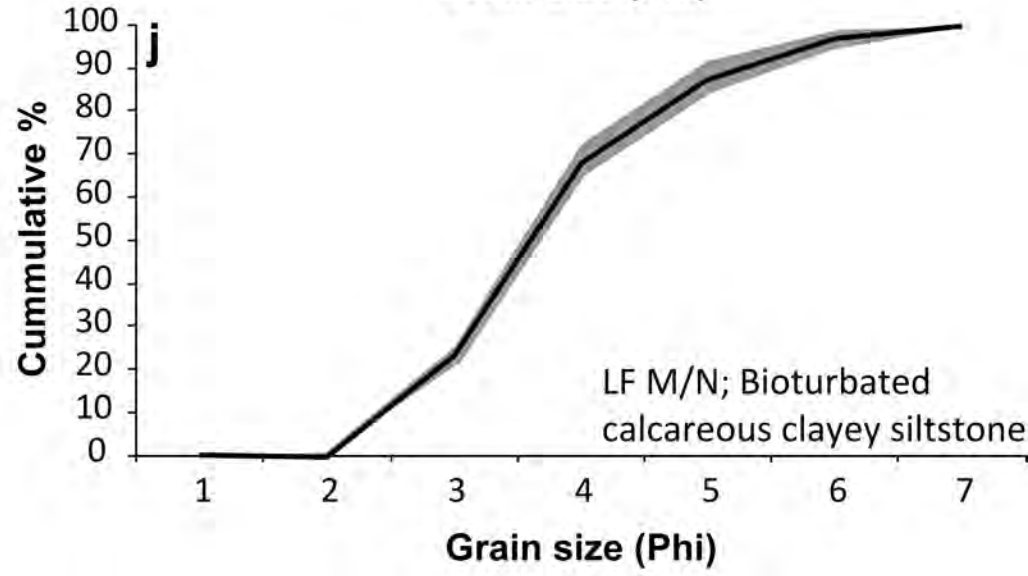
j
Cummulative %
Grain size (Phi)
LF M/N; Bioturbated calcareous clayey siltstone

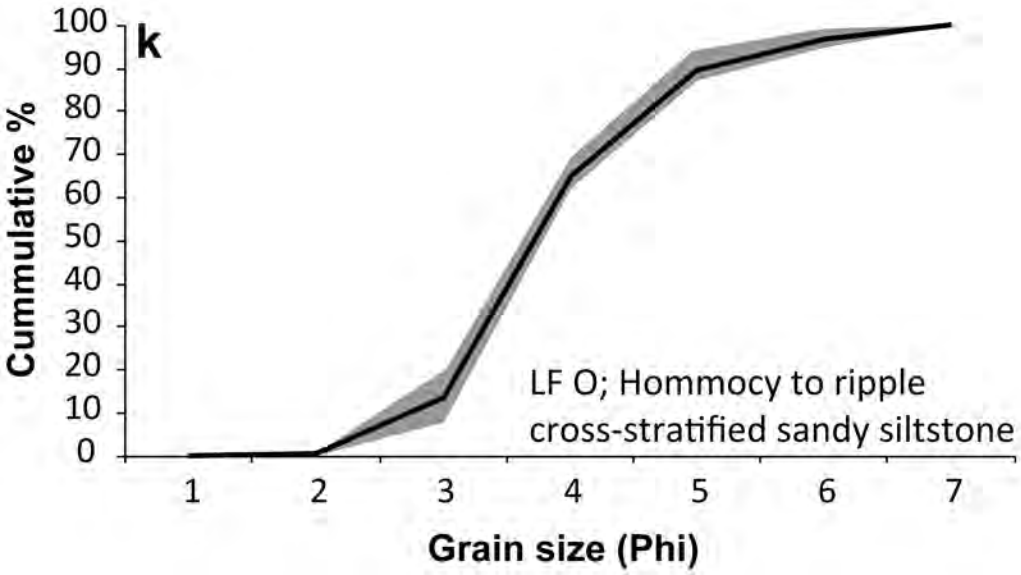
k
Cummulative %
Grain size (Phi)
LF O; Hommocy to ripple cross-stratified sandy siltstone

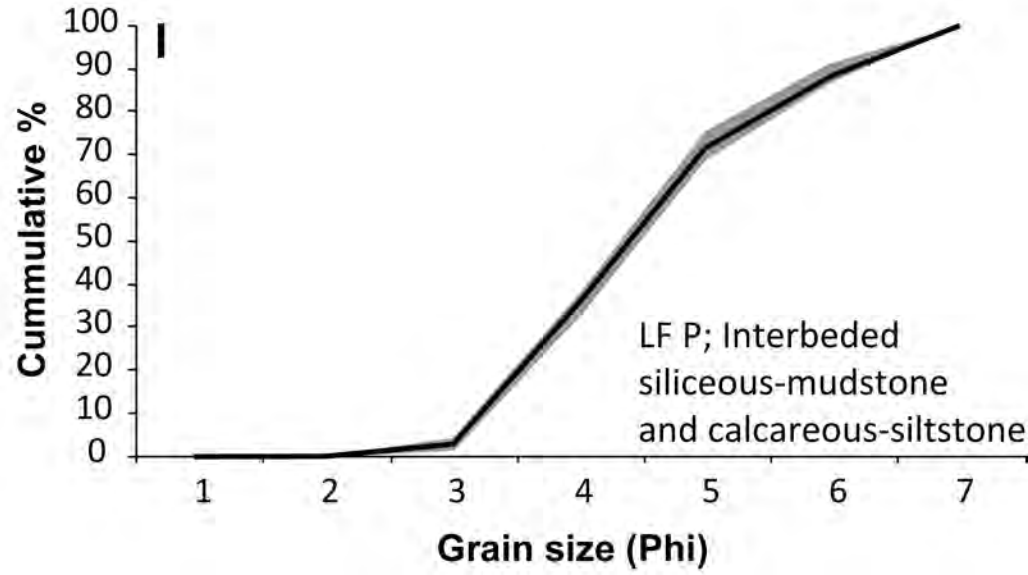
l
Cummulative %
Grain size (Phi)
LF P; Interbeded siliceous-mudstone and calcareous-siltstone

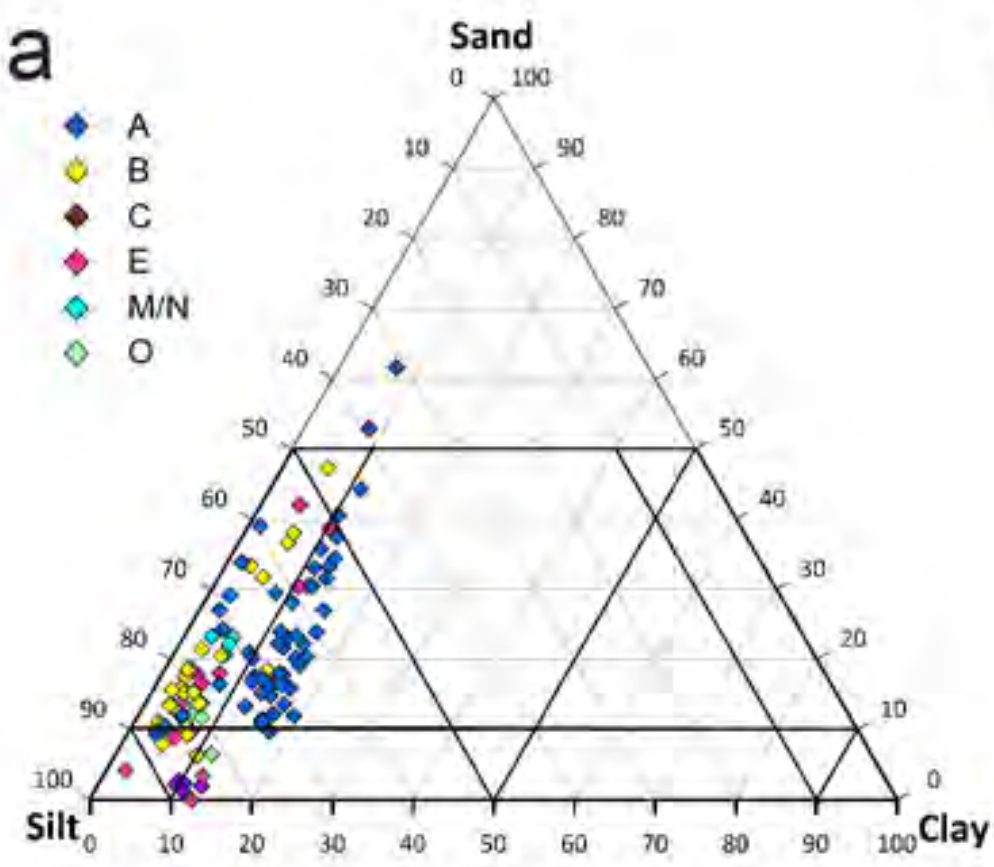
a
Sand
A
B
C
E
M/N
O
Silt
Clay

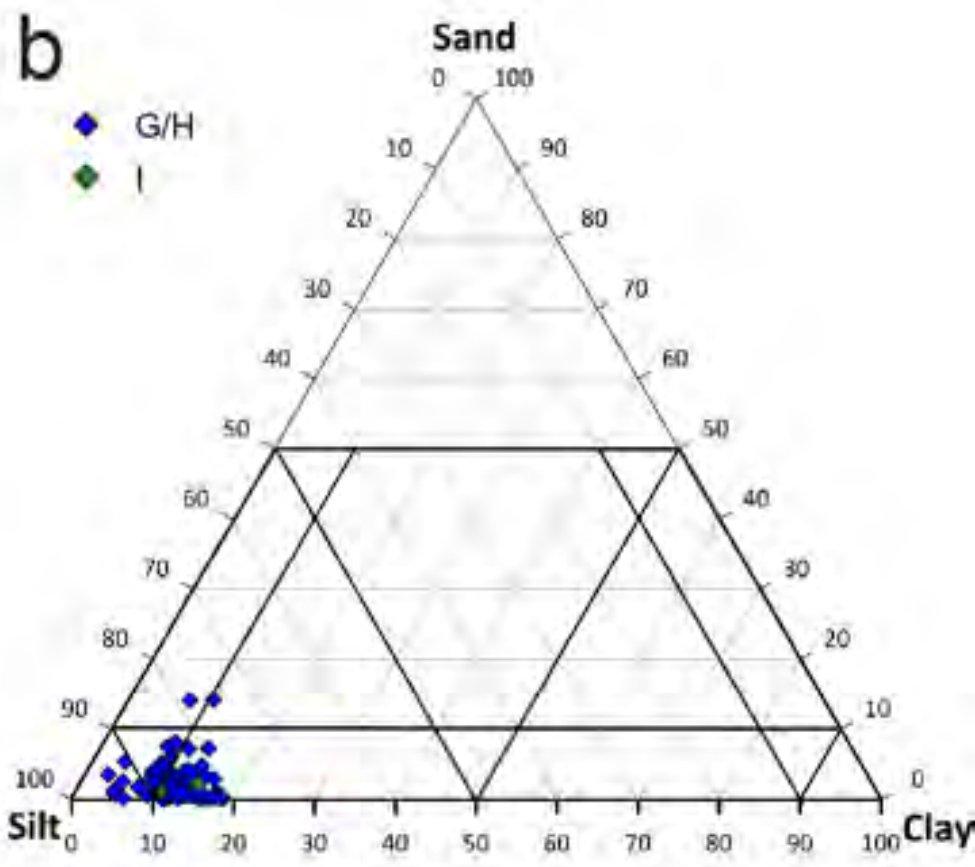
b
Sand
G/H
I
Silt
Clay

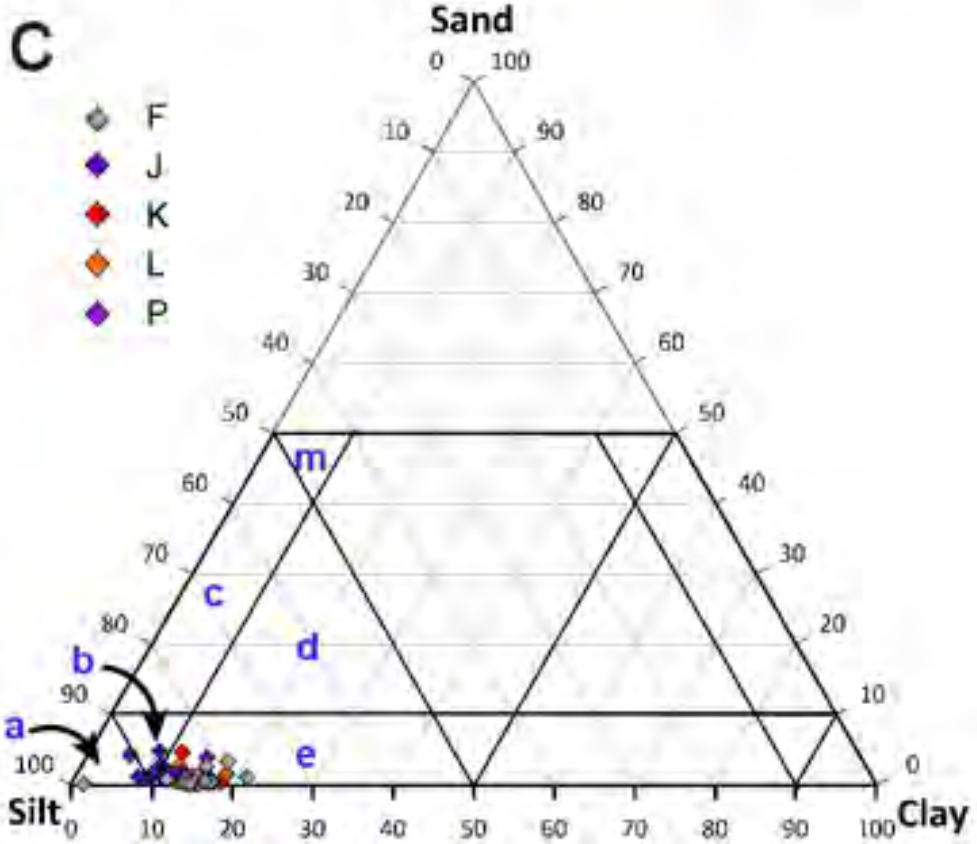
c
Sand
F
J
K
L
P
m
c
d
b
a
e
Silt
Clay

a

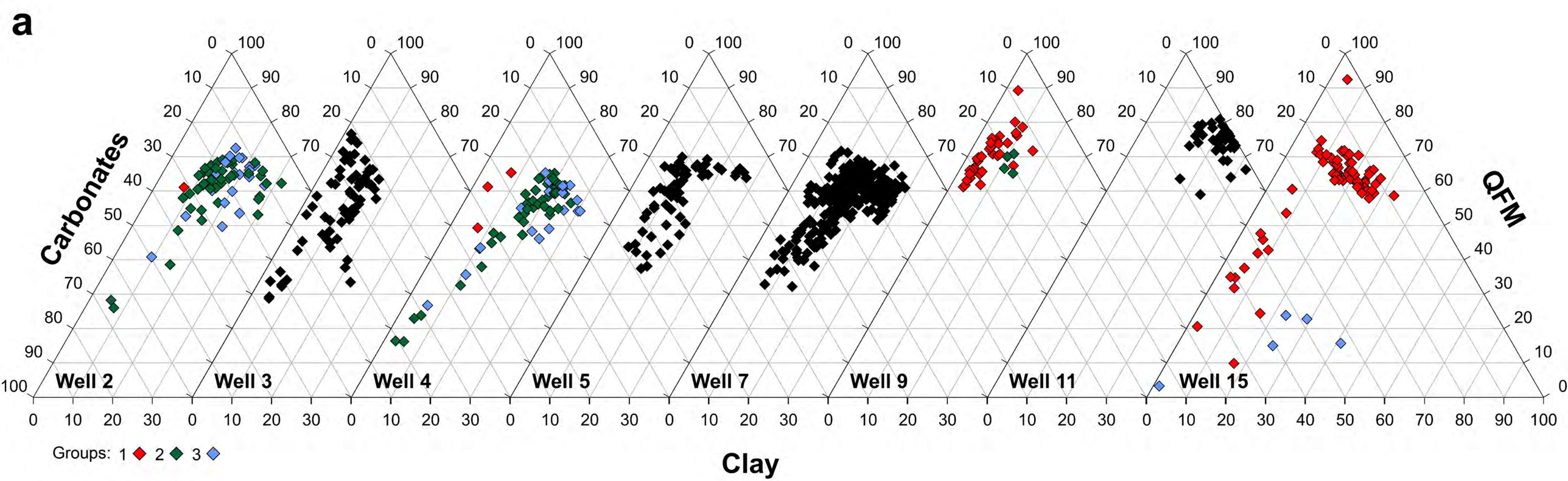
Carbonates
QFM
Clay
Well 2
Well 3
Well 4
Well 5
Well 7
Well 9
Well 11
Well 15
Groups: 1 2 3

b

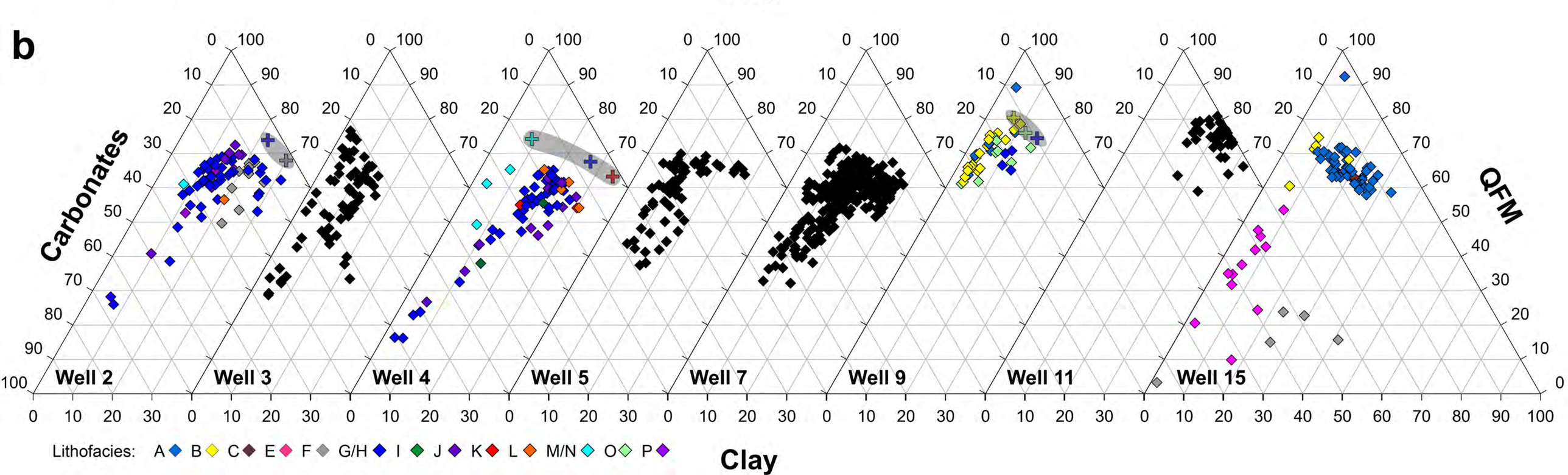
Carbonates
QFM
Clay
Well 2
Well 3
Well 4
Well 5
Well 7
Well 9
Well 11
Well 15
Lithofacies: A B C E F G/H I J K L M/N O P

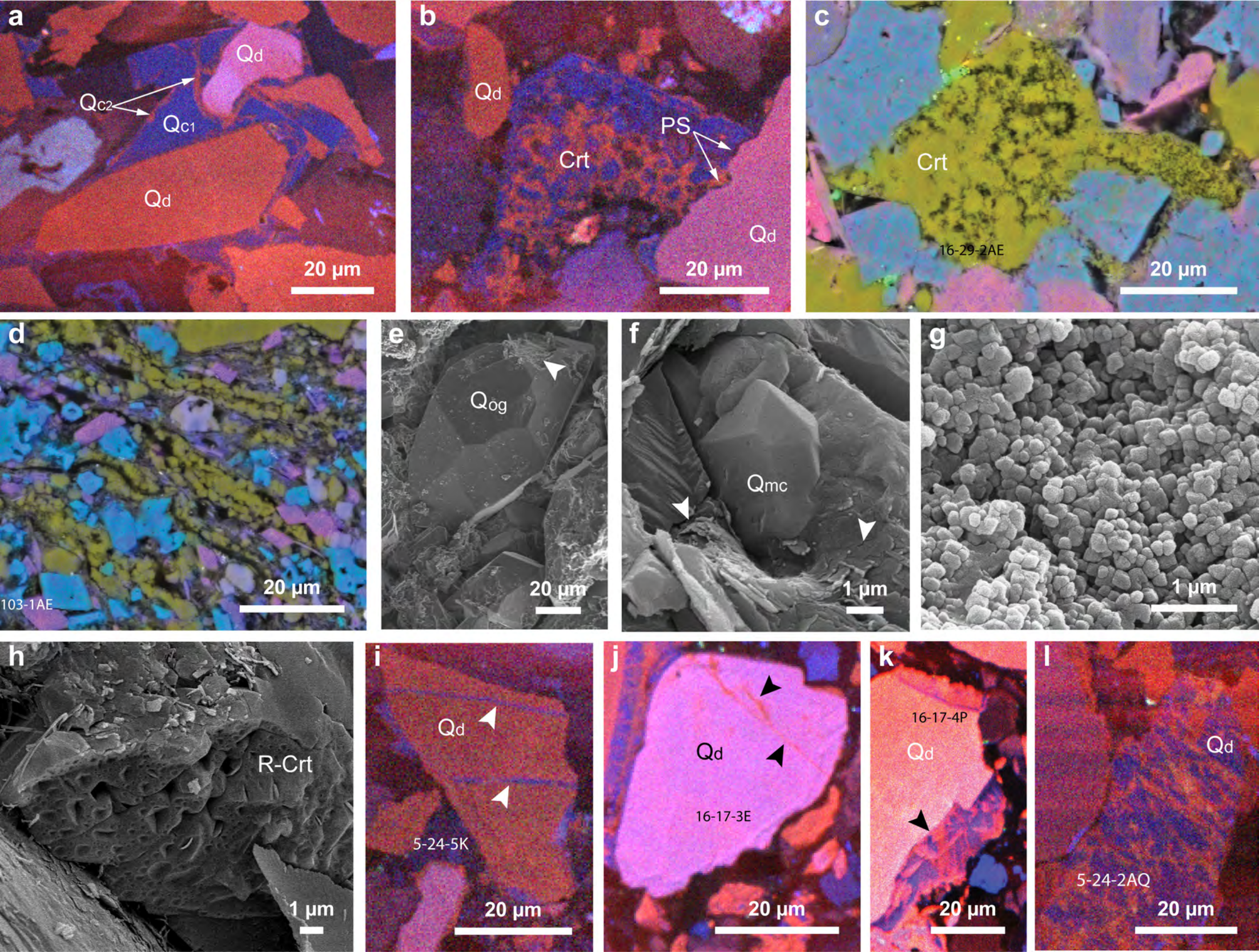
a
Qd
Qc2
Qc1
Qd
20 µm
b
Qd
PS
Crt
Qd
20 µm
c
Crt
16-29-2AE
20 µm
d
103-1AE
20 µm
e
Qog
20 µm
f
Qmc
1 µm
g
1 µm
h
R-Crt
1 µm
i
Qd
5-24-5K
20 µm
j
Qd
16-17-3E
20 µm
k
16-17-4P
Qd
20 µm
l
Qd
5-24-2AQ
20 µm

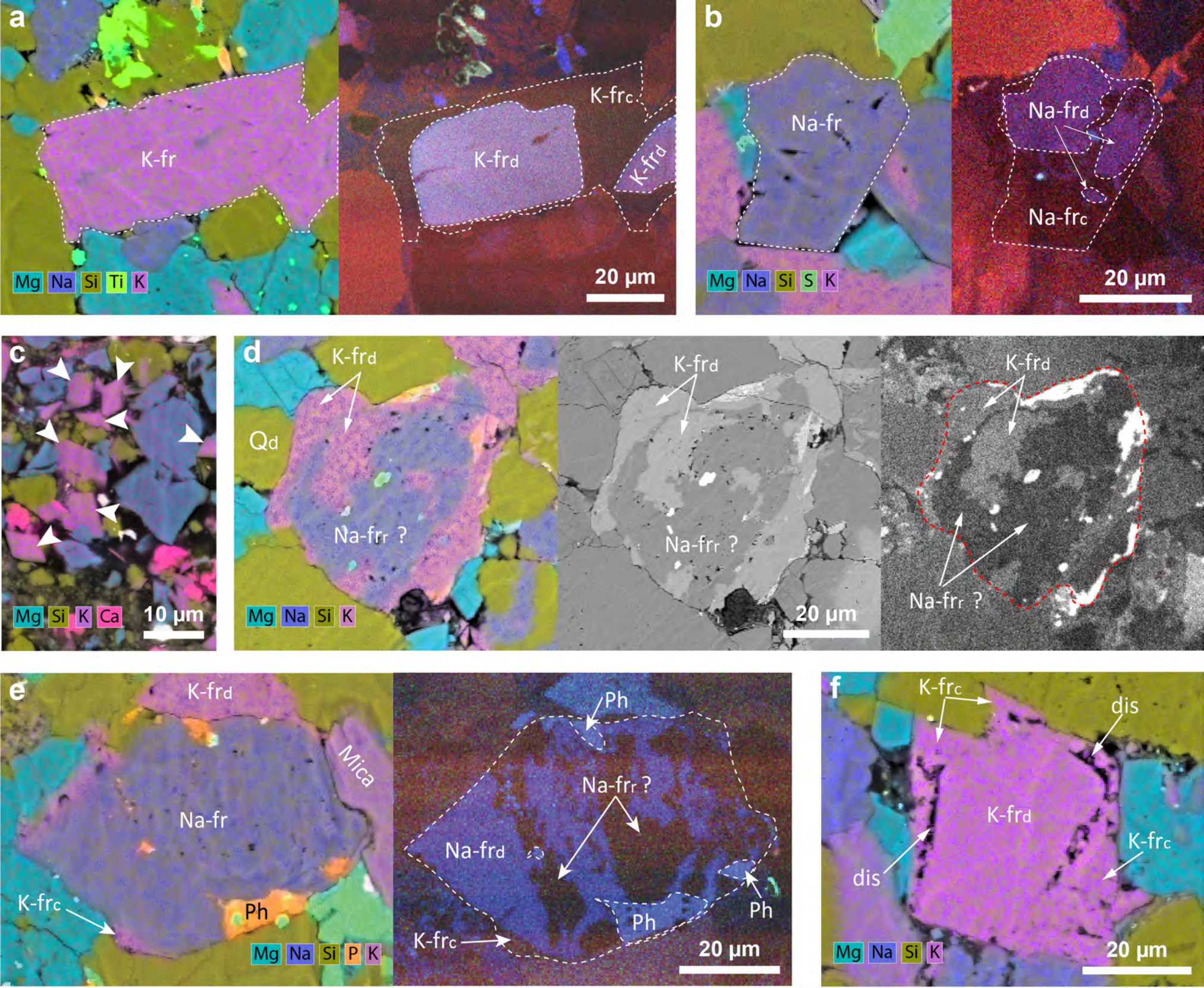
a
K-fr
Mg Na Si Ti K
K-frc
K-frd
K-frd
20 µm
b
Na-fr
Mg Na Si S K
Na-frd
Na-frc
20 µm
c
Mg Si K Ca
10 µm
d
K-frd
Qd
Na-frr ?
Mg Na Si K
K-frd
Na-frr ?
20 µm
K-frd
Na-frr ?
e
K-frd
Mica
Na-fr
K-frc
Ph
Mg Na Si P K
Ph
Na-frr ?
Na-frd
Ph
Ph
K-frc
20 µm
f
K-frc
dis
K-frd
dis
K-frc
Mg Na Si K
20 µm

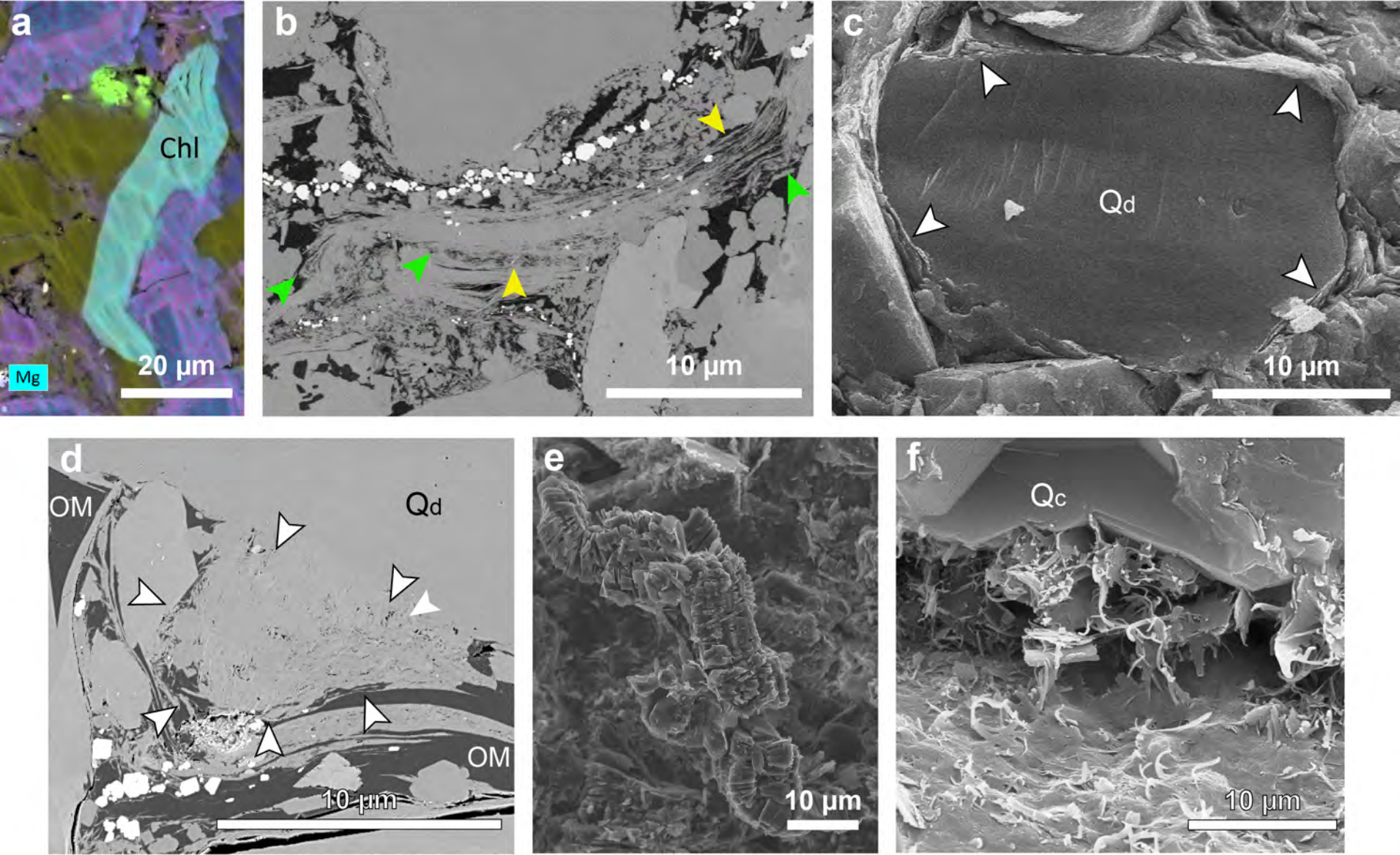
a
Chl
Mg
20 μm
b
10 μm
c
Qd
10 μm
d
OM
Qd
OM
10 μm
e
10 μm
f
Qc
10 μm

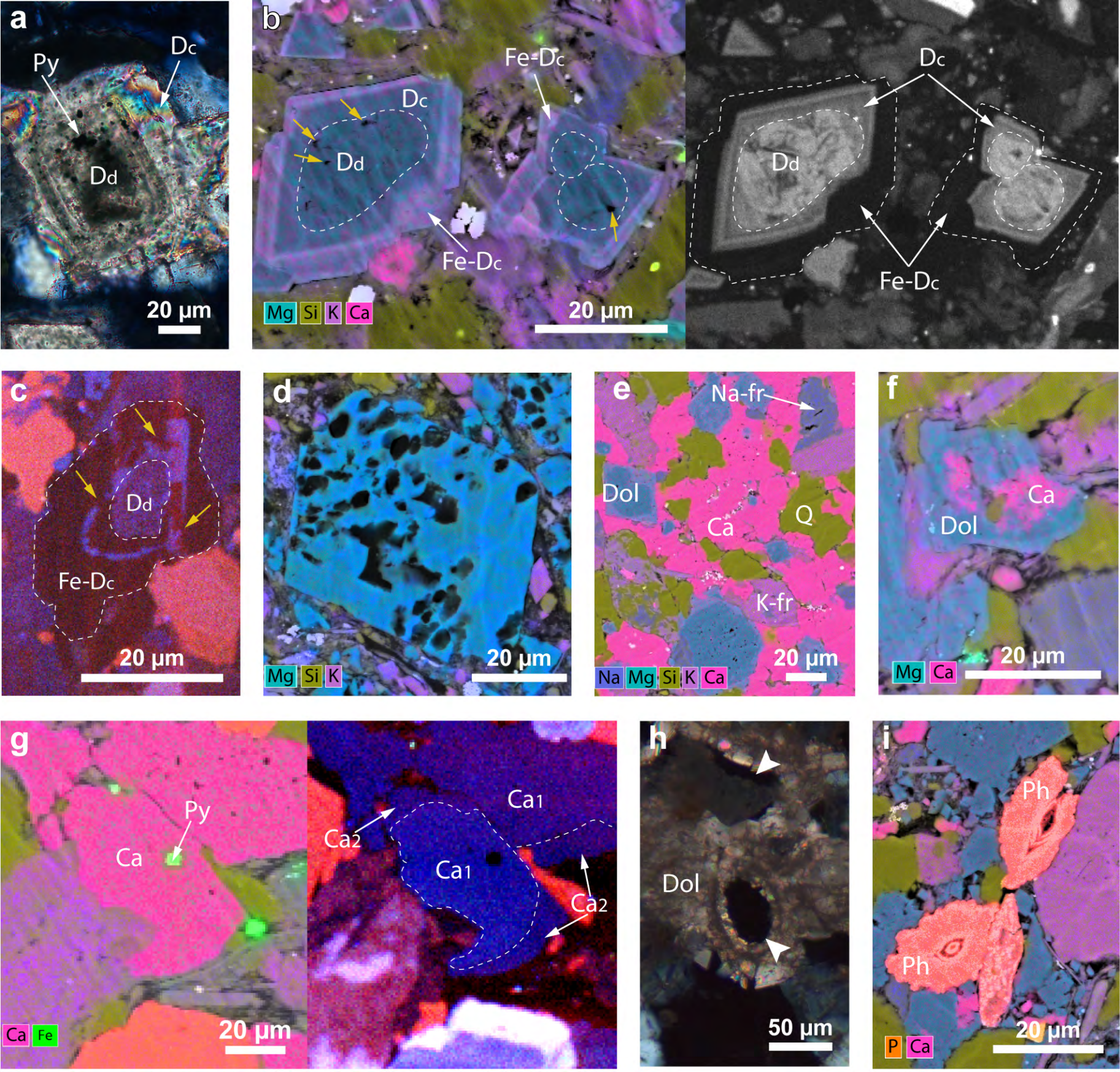
a
Py
Dc
Dd
20 μm
b
Fe-Dc
Dc
Dd
Fe-Dc
Mg Si K Ca
20 μm
Dc
Dd
Fe-Dc
c
Dd
Fe-Dc
20 μm
d
Mg Si K
20 μm
e
Na-fr
Dol
Ca
Q
K-fr
Na Mg Si K Ca
20 μm
f
Ca
Dol
Mg Ca
20 μm
g
Py
Ca
Ca Fe
20 μm
Ca1
Ca2
Ca1
Ca2
h
Dol
50 μm
i
Ph
Ph
P Ca
20 μm

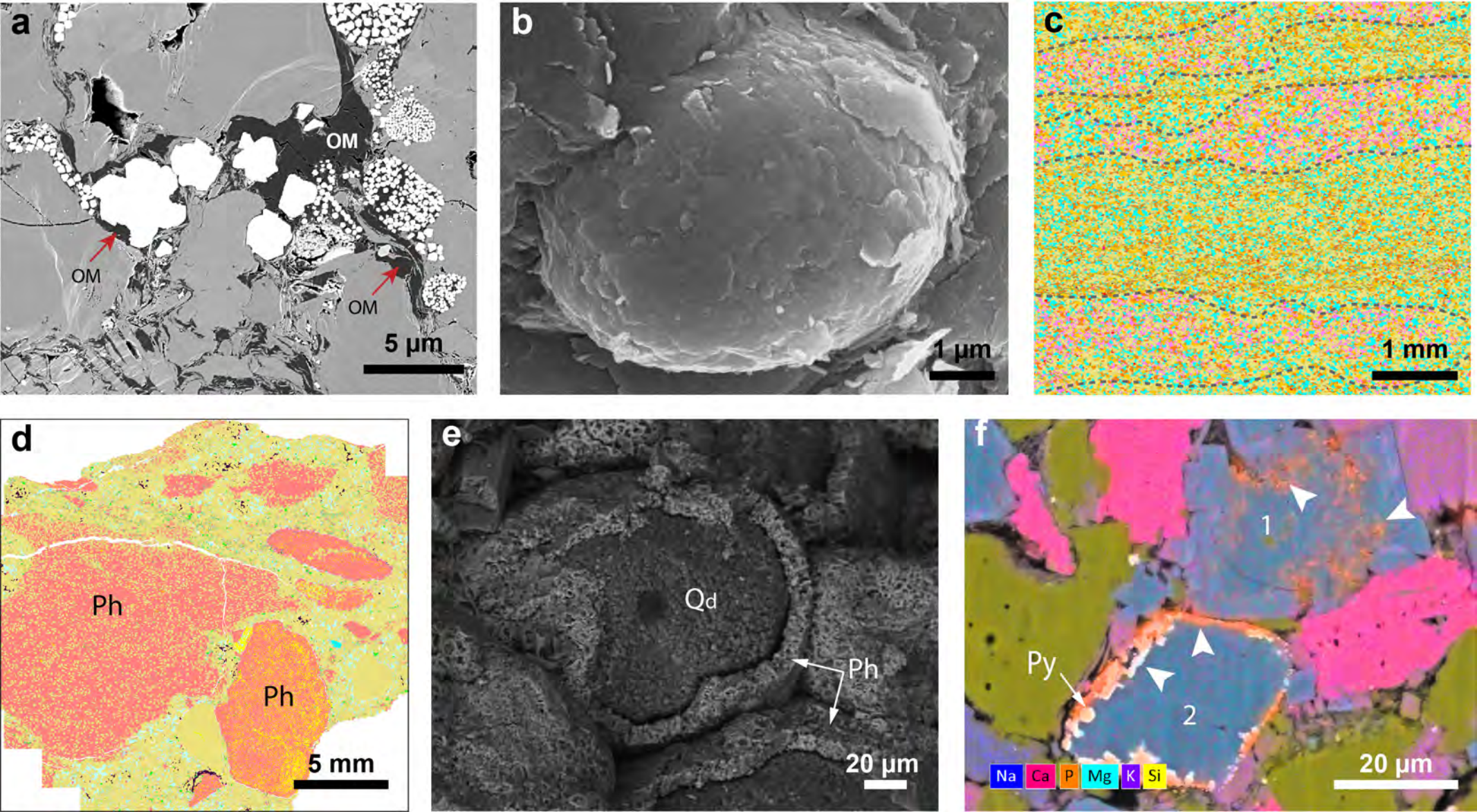
a
OM
OM
OM
5 μm
b
1 μm
c
1 mm
d
Ph
Ph
5 mm
e
Qd
Ph
20 μm
f
1
2
Py
Na
Ca
P
Mg
K
Si
20 μm

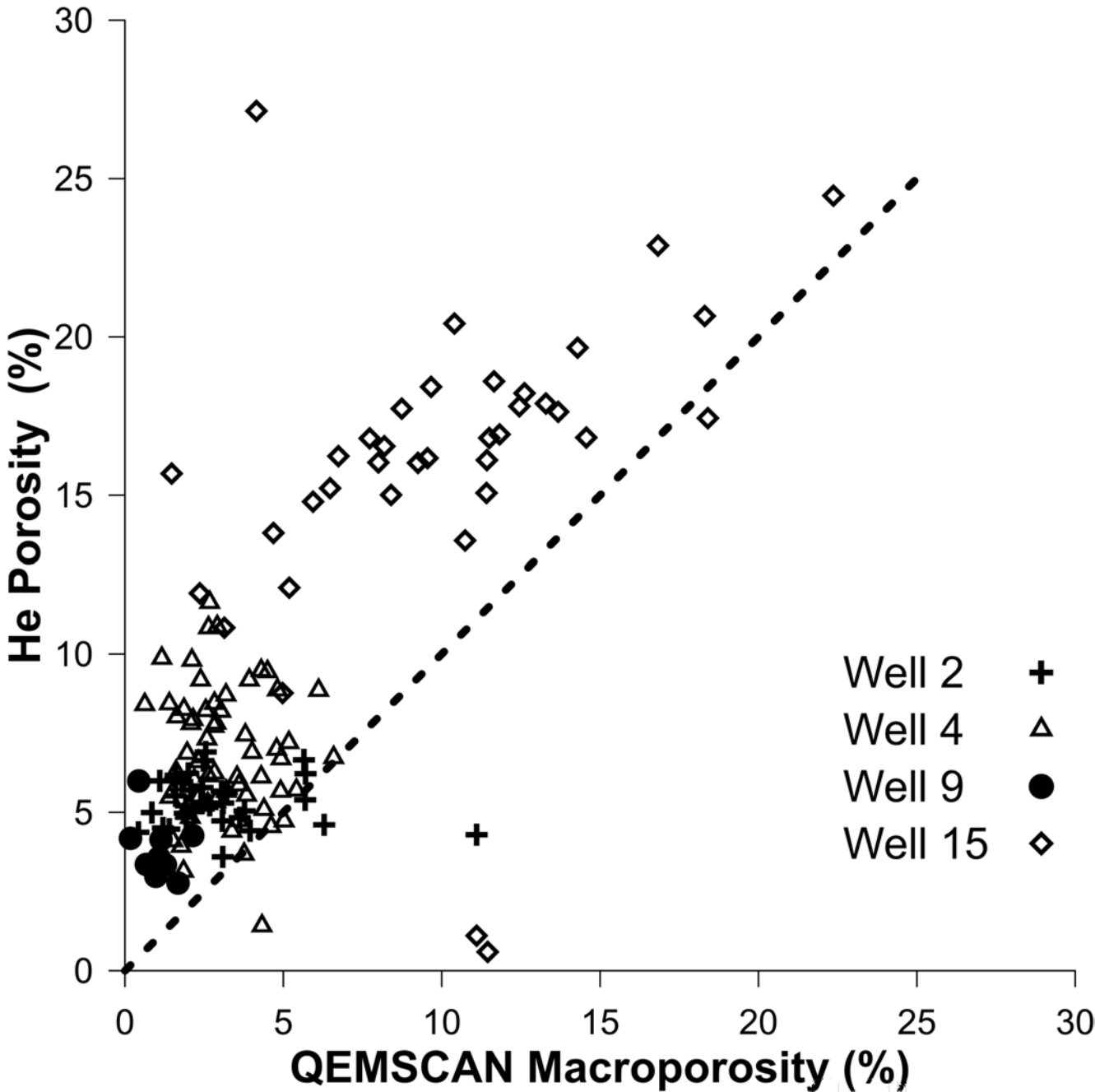
He Porosity (%)
QEMSCAN Macroporosity (%)
0
5
10
15
20
25
30
Well 2
Well 4
Well 9
Well 15

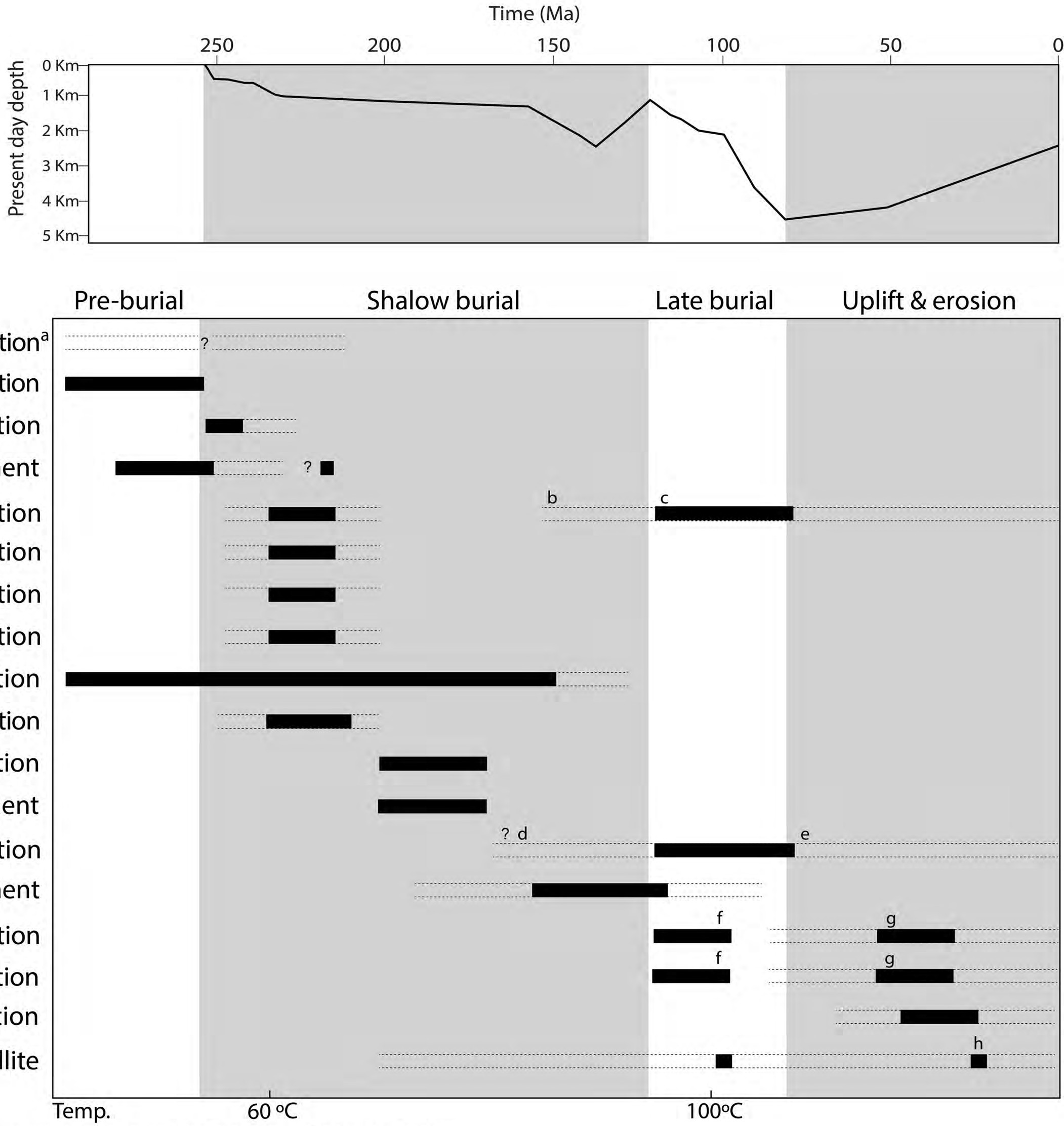

(a) Dissolved detrital components include dolomite, feldspar, chert.

(b) Quartz cment related to pressure solution. It is possible that the two generations of quartz cement are temporaly continous.

(c) Relationship between fibrous illite and HC emplacement is not clear.

(d) Pressure solution was potential active at shallow depth due to microfractures in quartz grains.

(e) Pressure solution is still an active process in the deeply burried section of the basin.

(f) Dissolution related to HC emplacement.

(g) Dissolution in the eastern (shallow) section of the basin related to meteoric water.

(h) In the eastern (shallow) section of the basin illite precipitation postdates kaolinite precipitation.

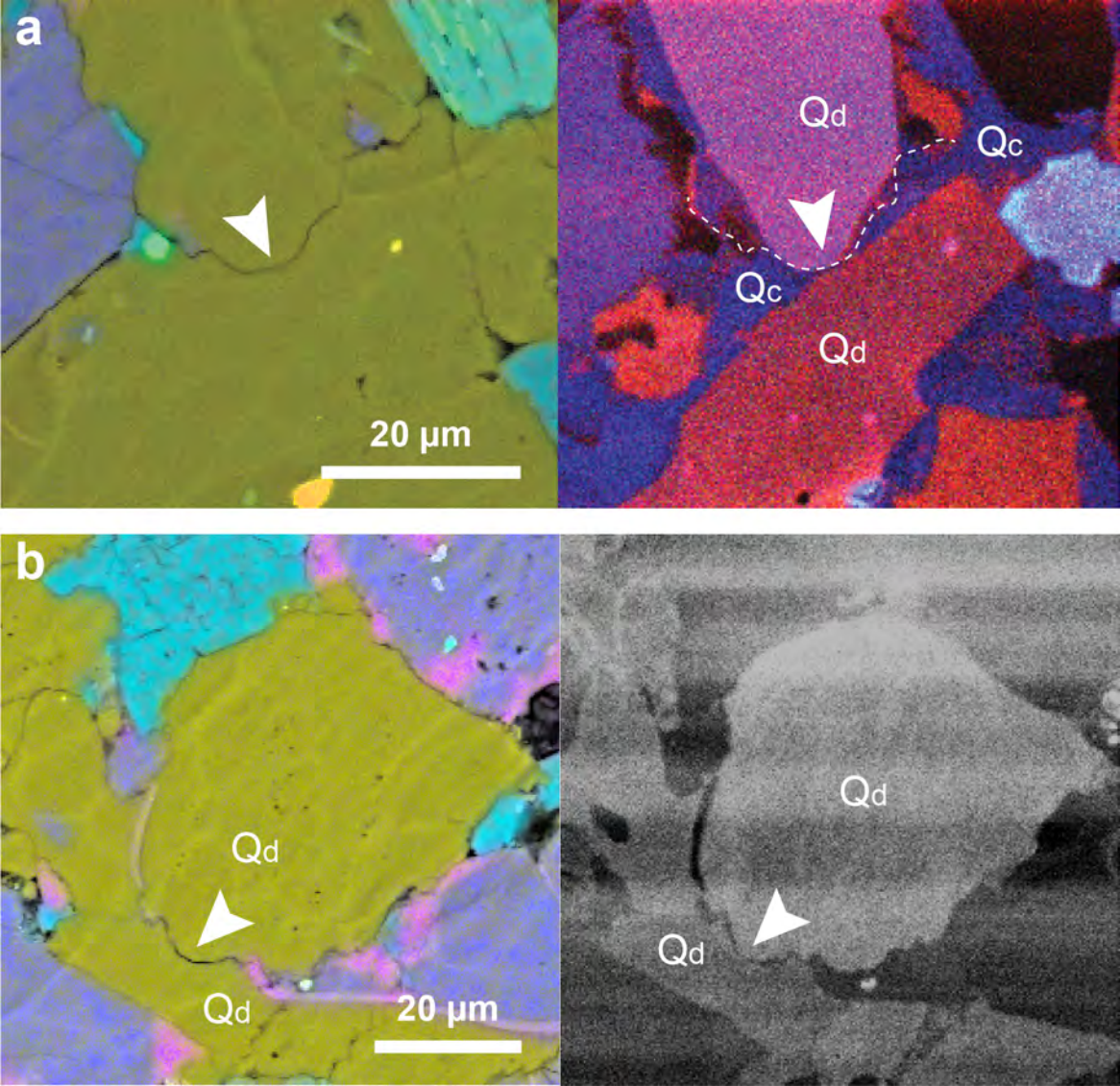
a
20 µm
Qd
Qc
Qc
Qd
b
Qd
Qd
20 µm
Qd
Qd

Porosity / IGV (%)

0 10 20 30 40 50 60 70 80 90

Depth (Km)

0 1 2 3

a

b

c

Silt-rich sediment (Kominz et al., 2011)

Clean, well-sorted sandstone (Paxton et al., 2002)

Mudstone (Velde, 1996)

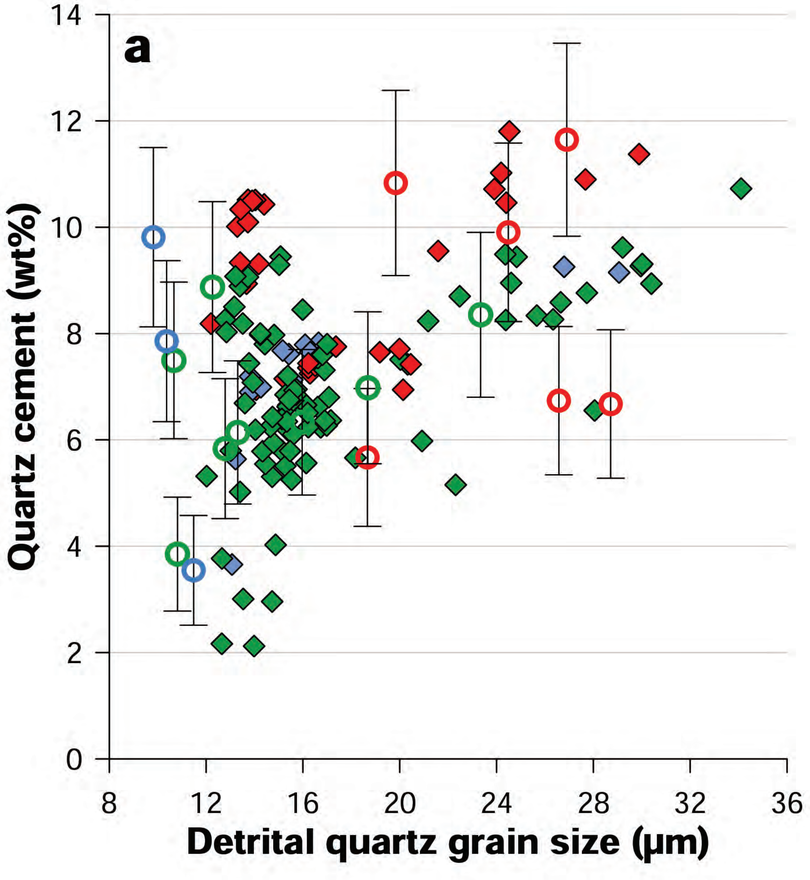
a
Quartz cement (wt%)
0
2
4
6
8
10
12
14
8
12
16
20
24
28
32
36
Detrital quartz grain size (µm)

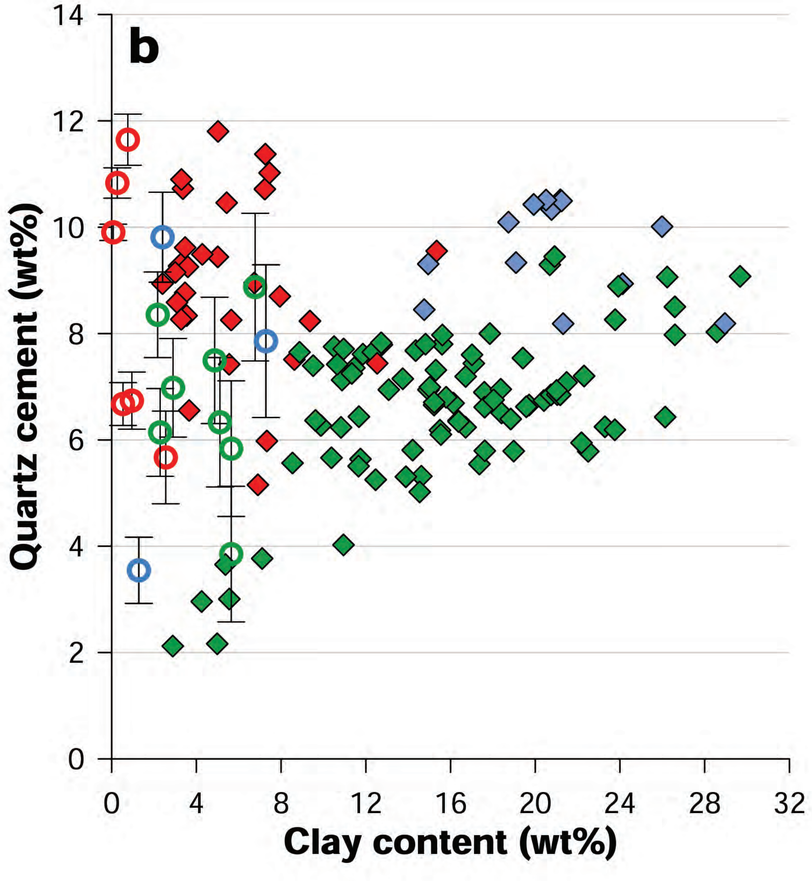
b
Quartz cement (wt%)
0
2
4
6
8
10
12
14
0
4
8
12
16
20
24
28
32
Clay content (wt%)

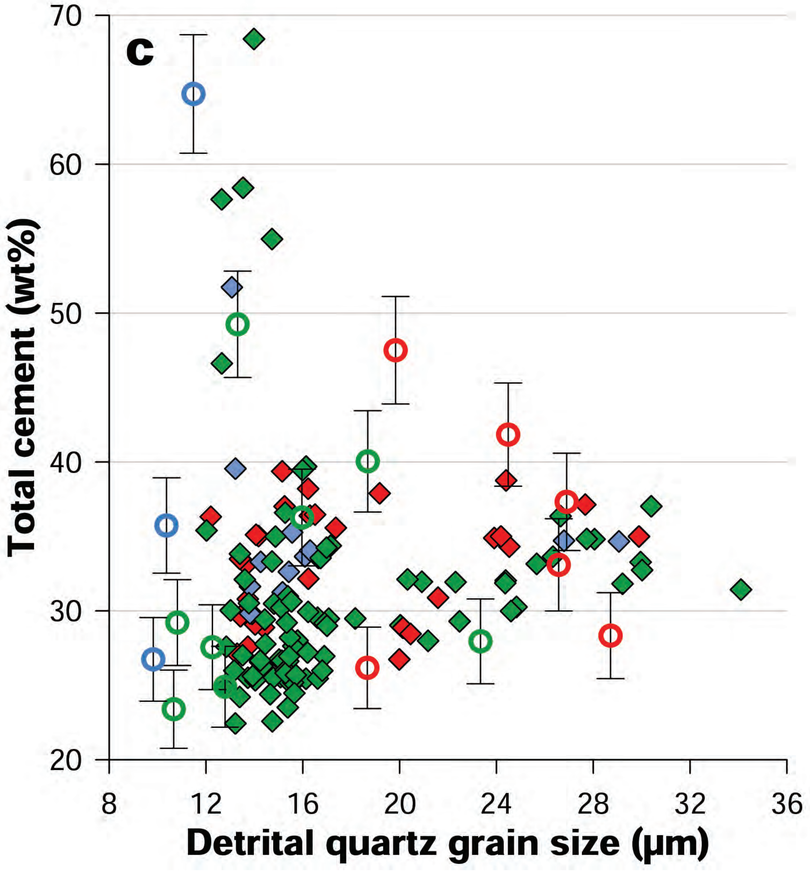
c
Total cement (wt%)
20
30
40
50
60
70
8
12
16
20
24
28
32
36
Detrital quartz grain size (µm)

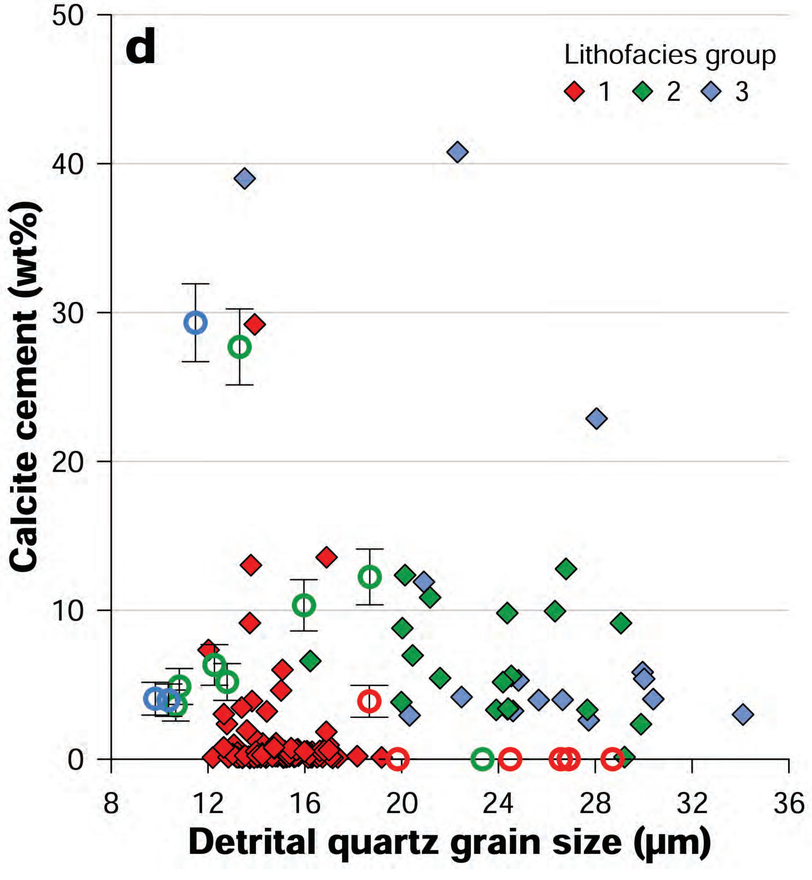
d
Lithofacies group
1
2
3
Calcite cement (wt%)
0
10
20
30
40
50
8
12
16
20
24
28
32
36
Detrital quartz grain size (µm)

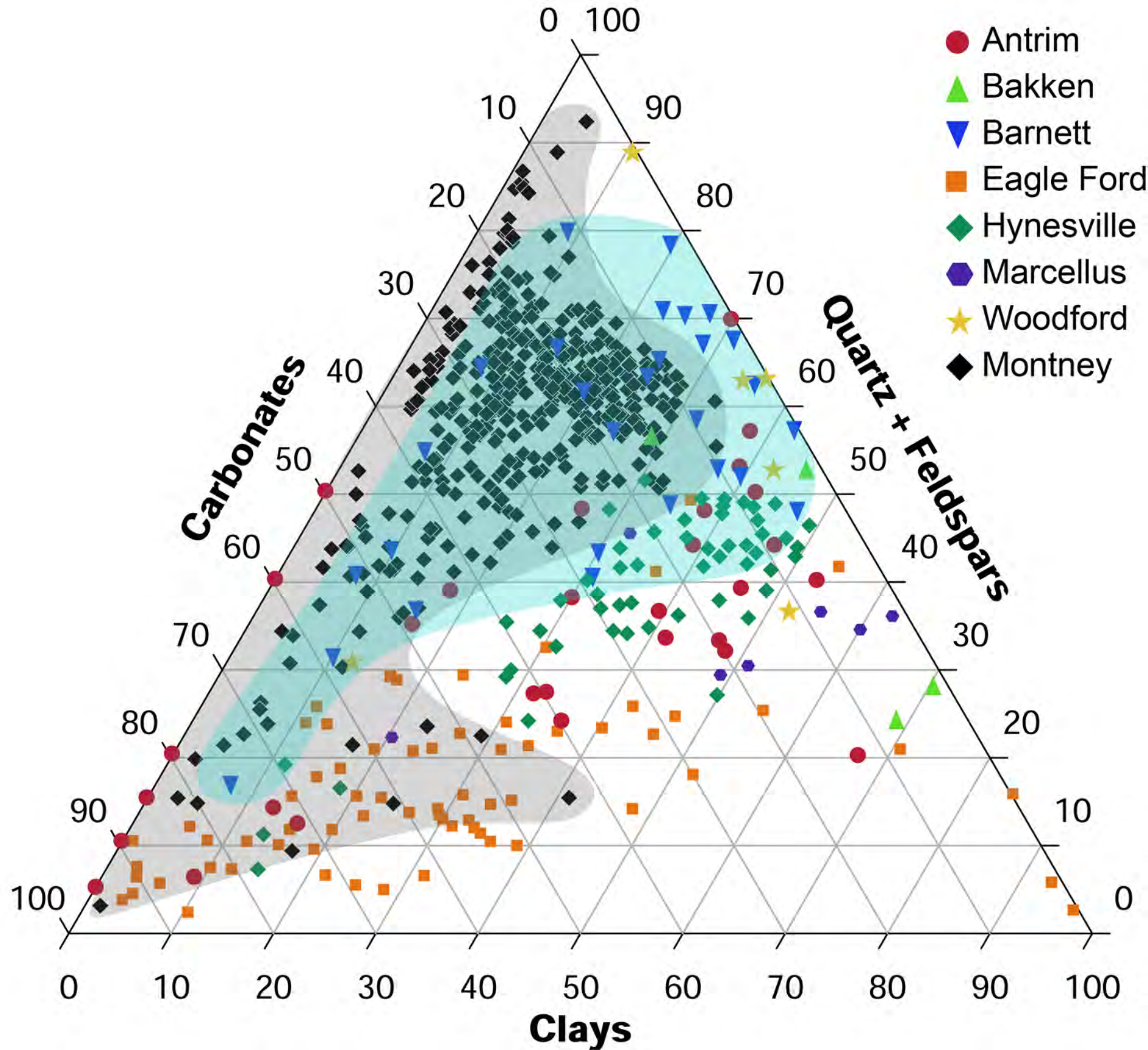
Antrim
Bakken
Barnett
Eagle Ford
Hynesville
Marcellus
Woodford
Montney
Carbonates
Quartz + Feldspars
Clays
0
10
20
30
40
50
60
70
80
90
100

Well #	Well location	Sample type	depth range (m)	Core description	SEM/ SEM-CL	Thin sections	Quantitative XRD	QEMSCAN	Matrix porosity	TOC
1	d-48-A/94-B-9	Core chips	1963 - 2068		15[c]					
2	16-17-083-25w6m	Core samples	2396 - 2364	available	31	6	4	70 (2-16)[d,e]	37 (2-19)[e]	45 (2-19)[e,f]
3	12-36-83-25W6	Cuttings	1855 - 2380					98 (5-20)		98 (5-20)[g]
4	16-29-079-20W6	Core samples	2616 - 2793	available	4	11	9	62 (1-5)	62 (1-6)	43 (2-11)[f]
5	14-14-76-12W6	Cuttings	2175 - 2545					55 (5-10)		25 (5)[g]
6	06-27-076-12W6	Thin section	2462.5 - 2447.3			2				
7	06-03-079-13W6	Pseudocuttings[b]	1930.5 - 2244.4					297 (1)	109 (1-6)	75 (1-8)
8	103/08-19-075-08W6	Thin section	2226			1				
9	05-24-63-6W6	Core samples	3272 - 3388	available	7	15	2	40 (2-3)	50 (0.5-5)	40 (2-3)[f]
10	16-10-073-26W5	Thin section	1793.2 - 1794.5			2				
11	06-33-072-25W5	Cuttings	1590 - 1740					28 (5)		30 (5)[g]
12	102/07-20-70-24W5	Thin section	1744.75			1				
13	07-01-065-22W5	Thin section	1960.5			1				
14	04-36-064-19W5	Thin section	1889.75			1				
15	103/05-20-079-22W5	Core samples	860 - 933	available	15	26[h]	9	66 (1-2)	37 (1-3)	25 (1-6)[f]
16	15-23-086-01W6	Core samples	881		3		3			
17	Norquay lookout[a]	Thin section	3.9			1				

[a]For sampling details see Crombez et al. (2016).

[b]Crushed and homogenized 1 m intervals.

[c]Number of samples analysed.

[d]Sampling interval for the specific analysis, meters.

[e]Large distance between samples due to missing core.

[f]TOC in wt%, obtained from Leco TOC analysis.

[g]TOC in wt%, obtained from RockEval analysis.

[h]Thin sections were also exhamined under table-top CL microscope.

Facies	Lithology	Rock type classification [a]	Sedimentary structures	Trace fossil Assemblage	Bioturbation intensity	Average composition			% core2 [d]	% core 4	% core 9	% core 15	% all
						% Clay	% Silt	% Sand	Distal, deeply buried	Distal, deeply buried	Proximal, deeply buried	Proximal, shallowly buried	
A	Interlaminated siltstone and sandstone	Sand bearing, silt rich to sand and clay-bearing, silt rich mudstone	Dominant flaser and lenticular bedding, current ripples, rare climbing ripples, mud rip-up clasts and soft sediment deformation	*Thalassinoides, Conichnus, Planolites* , and escape structures	0-2	11.9 (4.5) [b]	65.0 (10.3)	23.1 (11.1)			10.6	53.1	16.8
B	Massive sandy siltstone	Silt-rich to sand-bearing, silt rich mudstone	Rare soft sediment deformation, flame structures, carbonate nodules, mud rip-up clasts, and high-angle cross bedding	N/A	0	5.1 (2.5)	76.0 (11.0)	19.0 (10.7)			37.7	12.0	13.1
C	Bioturbated clay-rich siltstone	Sand and clay-bearing, silt rich mudstone	Horizontal parallel to wavy lamination	*Thalassinoides, Palaeophycus, Planolites* , and *Scolicia* (?)	3-5	15.0 [c]	69.0	17.0			0.03	2.0	0.5
D	Mudstone	Silt-bearing, clay-rich mudstone	Horizontal parallel lamination	N/A	0	No data						0.6	0.2
E	Dolomitic siltstone	Dolomite cement-dominated to dolomite cement-rich, silt-dominated to sand and clay-bearing, silt-rich mudstone	Low-high angle bedding, and rare rip-up clasts/ dolomitic breccia	N/A	0	7.2 (3.4)	75.2 (13.3)	17.6 (12.7)				22.4	5.9
F	Faintly laminated calcareous siltstone	Calcite cement-bearing, clay-bearing, silt-rich mudstone	Horizontal parallel lamination, carbonaceous grains, and rare shell debris	Biodeformation structures	0-1	14.6 (4.0)	83.3 (6.8)	2.1 (5.0)	16.5			9.8	6.6
G/H	Laminated siltstone	Silt-dominated to clay-bearing, silt-rich mudstone	Horizontal parallel lamination, rare wavy bedding, current ripples, rare amalgamated current ripples, soft sediment deformation, and presence of dolomite beds	Biodeformation structures, Planolites, laminae disruption and escape structures	0-1	11.8 (3.3)	85.9 (3.2)	2.3 (2.7)	58.4	61.5	10.4		31.1
I	Horizontal to irregularly laminated calcareous siltstone	Calcite cement-bearing, clay-bearing, silt-rich mudstone	Horizontal parallel and wavy lamination, and rare current ripples	Bio-deformation structures	3-5	12.4 (2.9)	85.9 (3.7)	1.7 (0.8)	2.3	2.9			1.2
J	Massive siliceous clayey siltstone	Silica cement-bearing, silt-dominated mudstone to clay-bearing, silt-rich mudstone	Rare dolomite beds	N/A	0	12.5 (3.4)	86.0 (2.9)	1.5 (1.3)	9.2	21.3	20.7		12.6
K	Massive calcareous clayey siltstone	Calcite cement-bearing, clay-bearing, silt-rich mudstone	Rare siltstone beds and lamination	N/A	0	14.9 (4.9)	82.7 (1.8)	2.5 (3.1)	0.8	3.7			1.0
L	Siliceous phosphatic siltstone	Silica cement-bearing, clay-bearing, silt-rich mudstone with phosphate nodules	mm-scale silica-rich lens-shaped structures, and phosphate nodules	Biodeformation structures	0-3	14.9 (2.6)	83.7 (2.6)	1.4 (1.0)	2.8	5.2			1.9
M/N	Bioturbated, calcareous, sandy siltstone	Calcite cement-bearing, sand-bearing, silt-rich mudstone	Rare mud rip-up clasts and phosphate nodules	*Phycosiphon, Teichichnus, Rosselia Cylindrichnus, Planolites, Skolithos, Asterosoma, Palaeophycus, Thalassinoides, rare Scolicia, Arenicolithes* , and *Arthicnus*	5-6	5.5 (1.4)	72.7 (1.2)	22.3 (1.2)	2.6	5.3			1.8
O	Hummocky to ripple cross-stratified sandy siltstone	Silt rich to sand-bearing, clay-bearing, silt-rich mudstone	Hummocky cross-stratification, current ripples, climbing ripples, mud rip-up clasts, rare loading structures and soft sediment deformation	Rare *Planolithes*	0-1	6.0 (2.8)	82.0 (2.3)	12.0 (3.5)			20.5		5.4
P	Interbedded siliceous-mudstone and calcareous- siltstone	Silica and calcite cement-bearing silt rich to clay-bearing, silt-rich mudstone	Soft sediment deformation, normal grading, shell debris, mud drapes, mud rip-up clasts, mud escape structures, current ripples, carbonate nodules, rare horizontal parallel lamination, and wavy lamination	N/A	0	10.6 (1.3)	87.2 (1.2)	2.2 (0.5)	7.5				1.8

[a] After Adams and Macquaker, 2003.

[b] Standard deviation 1σ.

[c] One sample.

[d] Facies % of core, normalize to exclude missing core sections.

Group	Group I						Group II		Group III						
Lithofacies	**A**	**B**	**C**	**E**	**M/N**	**O**	**G/H**	**I**	**F (total)**	**F (Well 2)**	**F (Well 15)**	**J**	**K**	**L**	**P**
Mode (μm)	42.55 (5.6) [d]	49.65 (4.70)	44.21 --	44.39 (12.35)	44.64 (3.29)	52.33 (3.07)	37.72 (3.45)	35.66 (1.48)	48.38 (19.66)	36.72 (2.62)	69.74 (19.42)	36.77 (2.99)	35.76 (0.45)	37.02 (3.84)	36.02 (0.97)
Mean [a]	4.14 (0.25)	4.12 (0.25)	4.28 --	4.44 (0.52)	4.10 (0.07)	4.25 (0.06)	4.95 (0.30)	5.01 (0.01)	5.19 (0.40)	5.08 (0.19)	5.37 (0.62)	4.98 (0.14)	4.92 (0.20)	4.96 (0.21)	4.92 (0.07)
σ1 [b]	1.11 (0.11)	0.94 (0.10)	1.10 --	1.03 (0.18)	1.04 (0.08)	0.93 (0.06)	0.87 (0.26)	0.92 (0.03)	0.82 (0.26)	0.86 (0.23)	0.75 (0.30)	0.80 (0.19)	0.82 (0.25)	0.74 (0.10)	0.82 (0.06)
Skeweness c	0.21 (0.05)	0.14 (0.31)	0.21 --	0.14 (0.16)	0.14 (0.06)	0.23 (0.03)	-0.08 (0.40)	-0.08 (0.02)	-0.25 (0.26)	-0.25 (0.28)	-0.24 (0.27)	-0.25 (0.53)	-0.23 (0.46)	-0.49 (0.23)	-0.26 (0.10)

[a] $Graphic\ mean = \frac{\phi 16 + \phi 50 + \phi 84}{3}$

[b] $Graphic\ standard\ deviation = \frac{\phi 84 - \phi 16}{4} + \frac{\phi 95 - \phi 5}{6.6}$

[c] $Inclussive\ graphic\ skewness = \frac{\phi 16 + \phi 84 - 2\phi 50}{2(\phi 84 - \phi 16)} + \frac{\phi 5 + \phi 95 - 2\phi 50}{2(\phi 95 - \phi 5)}$

[d] *Standard deviation*

Well		2					4						9					
Sample		3E	4P	12E	16O	16I	2AE	2H	3AJ	4V	5AD	5V	1C	2AQ	3B	4F	5K	5N
Depth (m)		2281.0	2289.0	2431.1	2480.9	2487.0	2621.0	2644.0	2653.0	2703.0	2731.0	2739.0	3278.0	3289.1	3340.0	3364.0	3379.0	3376.0
Lithofacies		G/H	G/H	G/H	F	F	M/N	G/H	G/H	K	G/H	G/H	B	B	O	B	G/H	B
Detiral	Qz detrital	27.2 (2.5) [a]	22.3 (2.3)	26.2 (2.4)	27.9 (2.5)	19.3 (2.2)	27.3 (2.5)	22.2 (2.3)	16.7 (2.1)	9.2 (1.6)	22.1 (2.3)	27.3 (2.5)	27.6 (2.5)	38.1 (2.7)	26.3 (2.4)	31.9 (2.6)	32.3 (2.6)	29.3 (2.5)
	Chert	1.1 (0.6)	2.1 (0.8)	4.4 (1.1)	4.4 (1.1)	2.0 (0.8)	3.3 (1.0)	4.9 (1.2)	2.4 (0.9)	0.0 0.0	1.0 (0.5)	3.3 (1.0)	4.2 (1.1)	2.0 (0.8)	2.4 (0.8)	3.4 (1.0)	2.9 (0.9)	2.3 (0.8)
	K-feldspar detrital	5.8 (1.3)	5.5 (1.3)	3.7 (1.0)	3.7 (1.0)	4.3 (1.1)	5.1 (1.2)	5.8 (1.3)	8.6 (1.5)	1.9 (0.8)	13.3 (1.9)	7.0 (1.4)	9.8 (1.6)	10.0 (1.7)	9.7 (1.6)	9.9 (1.6)	8.8 (1.6)	4.3 (1.1)
	Na-feldspar detrital	4.6 (1.2)	5.8 (1.3)	6.4 (1.4)	7.0 (1.4)	5.2 (1.2)	5.0 (1.2)	8.5 (1.5)	5.4 (1.3)	3.8 (1.1)	8.8 (1.6)	9.0 (1.6)	7.0 (1.4)	6.2 (1.3)	5.7 (1.3)	4.9 (1.2)	5.8 (1.3)	4.5 (1.1)
	Dolomite detrital	2.6 (0.9)	3.0 (0.9)	2.3 (0.8)	1.2 (0.6)	4.4 (1.1)	16.9 (2.1)	5.9 (1.3)	4.2 (1.1)	8.3 (1.5)	2.5 (0.9)	3.4 (1.0)	7.7 (1.5)	4.6 (1.2)	7.2 (1.4)	5.4 (1.3)	6.1 (1.3)	6.2 (1.3)
	Clay	2.9 (0.9)	5.1 (1.2)	5.6 (1.3)	2.4 (0.8)	7.3 (1.4)	2.6 (0.9)	5.6 (1.3)	2.3 (0.8)	1.3 (0.6)	6.8 (1.4)	4.9 (1.2)	1.0 (0.5)	0.5 (0.4)	0.1 (0.2)	0.8 (0.5)	2.2 (0.8)	0.3 (0.3)
	Mica	7.1 (1.4)	7.8 (1.5)	14.1 (1.9)	18.0 (2.1)	16.5 (2.0)	3.9 (1.1)	7.0 (1.4)	4.2 (1.1)	2.9 (0.9)	6.7 (1.4)	12.9 (1.9)	3.4 (1.0)	5.2 (1.2)	2.9 (0.9)	3.5 (1.0)	7.1 (1.4)	2.6 (0.9)
	Heavy minerals	0.3 (0.3)	0.7 (0.5)	0.5 (0.4)	0.0 (0.0)	0.4 (0.4)	0.2 (0.2)	0.9 (0.5)	0.2 (0.3)	0.3 (0.3)	0.6 (0.4)	0.5 (0.4)	0.5 (0.4)	0.3 (0.3)	0.7 (0.5)	0.2 (0.2)	0.1 (0.2)	0.2 (0.2)
Authigenic	Qz cement (1st generation)	5.1 (1.2)	3.2 (1.0)	3.1 (1.0)	5.6 (1.3)	5.1 (1.2)	3.3 (1.0)	2.8 (0.9)	2.5 (0.9)	1.9 (0.7)	5.4 (1.2)	6.0 (1.3)	6.0 (1.3)	5.1 (1.2)	7.9 (1.5)	8.7 (1.6)	6.7 (1.4)	9.3 (1.6)
	Qz cement (2nd generation)	1.9 (0.7)	3.2 (1.0)	2.8 (0.9)	4.2 (1.1)	2.7 (0.9)	2.4 (0.8)	1.0 (0.6)	3.7 (1.0)	1.7 (0.7)	3.5 (1.0)	1.5 (0.7)	0.8 (0.5)	1.5 (0.7)	2.0 (0.8)	2.9 (0.9)	1.7 (0.7)	1.5 (0.7)
	K-feldspar cement	7.0 (1.4)	5.4 (1.2)	2.4 (0.9)	2.2 (0.8)	1.4 (0.6)	1.3 (0.6)	1.5 (0.7)	1.4 (0.7)	1.4 (0.7)	2.3 (0.8)	3.8 (1.1)	4.2 (1.1)	4.6 (1.2)	6.2 (1.3)	4.6 (1.2)	3.1 (1.0)	2.5 (0.9)
	Na-feldspar cement	2.4 (0.9)	2.3 (0.8)	1.9 (0.8)	1.4 (0.7)	1.4 (0.7)	0.8 (0.5)	1.8 (0.7)	1.7 (0.7)	0.9 (0.5)	1.3 (0.6)	0.1 (0.2)	2.7 (0.9)	3.2 (1.0)	3.0 (0.9)	2.6 (0.9)	1.5 (0.7)	2.0 (0.8)
	Na-feldspar albitization	1.0 (0.5)	1.0 (0.6)	1.1 (0.6)	0.8 (0.5)	1.1 (0.6)	0.2 (0.3)	0.0 0.0	1.4 (0.7)	0.3 (0.3)	1.2 (0.6)	2.7 (0.9)	2.7 (0.9)	3.4 (1.0)	2.7 (0.9)	0.2 (0.3)	0.8 (0.5)	1.9 (0.8)
	Dolomite cement	1.2 (0.6)	2.1 (0.8)	2.6 (0.9)	2.7 (0.9)	6.9 (1.4)	11.3 (1.7)	3.2 (1.0)	1.9 (0.7)	4.0 (1.1)	0.1 (0.2)	0.7 (0.5)	7.1 (1.4)	1.4 (0.6)	7.2 (1.4)	4.0 (1.1)	7.3 (1.4)	14.4 (1.9)
	Fe-dolomite	6.5 (1.4)	6.8 (1.4)	3.5 (1.0)	3.5 (1.0)	10.3 (1.7)	0.6 (0.4)	12.6 (1.8)	8.4 (1.5)	23.9 (2.4)	4.6 (1.2)	3.5 (1.0)	6.1 (1.3)	3.7 (1.0)	7.3 (1.4)	9.7 (1.6)	4.0 (1.1)	12.7 (1.8)
	Calcite (1st generation)	5.1 (1.2)	6.9 (1.4)	0.9 (0.5)	3.0 (0.9)	2.7 (0.9)	0.0 0.0	2.0 (0.8)	2.6 (0.9)	3.3 (1.0)	2.1 (0.8)	1.6 (0.7)	0.0 (0.0)	0.0 (0.0)	0.0 (0.0)	0.0 (0.0)	0.0 (0.0)	0.0 0.0
	Calcite (2nd generation)	7.1 (1.4)	3.5 (1.0)	4.3 (1.1)	1.1 (0.6)	1.2 (0.6)	3.9 (1.1)	2.9 (0.9)	25.1 (2.4)	26.0 (2.4)	4.2 (1.1)	2.0 (0.8)	0.0 (0.0)	0.0 (0.0)	0.0 (0.0)	0.0 (0.0)	0.0 (0.0)	0.0 (0.0)
	Anhydrite	0.0 (0.0)	0.0 (0.0)	0.0 (0.0)	0.0 (0.0)	0.0 (0.0)	0.0 (0.0)	0.0 (0.0)	0.0 (0.0)	0.0 (0.0)	0.0 (0.0)	0.0 (0.0)	2.3 (0.8)	1.5 (0.7)	4.1 (1.1)	3.0 (0.9)	0.0 (0.0)	1.6 (0.7)
	Halite	0.2 (0.2)	0.0 (0.0)	0.0 (0.0)	0.0 (0.0)	0.2 (0.2)	0.0 (0.0)	0.0 (0.0)	0.0 (0.0)	0.0 (0.0)	0.0 (0.0)	0.0 (0.0)	0.0 0.0	0.0 (0.0)	0.0 (0.0)	0.0 (0.0)	0.0 (0.0)	0.0 (0.0)
	Pyrite	1.3 (0.6)	1.9 (0.8)	2.3 (0.8)	1.7 (0.7)	2.5 (0.9)	1.1 (0.6)	0.7 (0.5)	0.5 (0.4)	0.6 (0.4)	1.8 (0.7)	0.9 (0.5)	0.6 (0.4)	0.8 (0.5)	0.4 (0.3)	0.7 (0.5)	2.4 (0.8)	0.6 (0.4)
	Phosphate	1.3 (0.6)	0.0 (0.0)	0.0 (0.0)	0.5 (0.4)	0.2 (0.3)	1.4 (0.6)	0.7 (0.5)	0.1 (0.2)	0.7 (0.5)	1.0 (0.5)	0.5 (0.4)	0.8 (0.5)	3.2 (1.0)	0.9 (0.5)	1.0 (0.5)	0.5 (0.4)	0.9 (0.5)
porosity	Primary porosity	0.0 0.0	3.2 (1.0)	0.0 0.0	2.3 (0.8)	1.3 (0.6)	2.2 (0.8)	2.6 (0.9)	2.7 (0.9)	2.3 (0.8)	2.3 (0.8)	3.7 (1.0)	1.9 (0.8)	1.6 (0.7)	0.9 (0.5)	0.9 (0.5)	2.5 (0.9)	1.5 (0.7)
	Organic matter-filled porosity	7.0 (1.4)	5.8 (1.3)	8.8 (1.6)	4.0 (1.1)	1.1 (0.6)	5.6 (1.3)	5.1 (1.2)	1.3 (0.6)	2.7 (0.9)	4.9 (1.2)	3.2 (1.0)	1.6 (0.7)	1.5 (0.7)	0.6 (0.4)	0.8 (0.5)	1.4 (0.6)	0.6 (0.4)
	Secondary porosity	0.1 (0.2)	0.2 (0.3)	0.1 (0.2)	0.0 0.0	0.1 (0.2)	0.4 (0.3)	0.3 (0.3)	0.5 (0.4)	0.2 (0.3)	0.3 (0.3)	0.0 0.0	0.3 (0.3)	0.1 (0.2)	0.0 0.0	0.0 0.0	0.7 (0.5)	0.3 (0.3)
unknown	Unknown	1.4 (0.7)	2.2 (0.8)	3.1 (1.0)	2.3 (0.8)	2.3 (0.8)	1.4 (0.7)	1.9 (0.7)	2.1 (0.8)	2.4 (0.8)	3.1 (1.0)	1.5 (0.7)	1.8 (0.7)	1.4 (0.7)	1.7 (0.7)	1.1 (0.6)	2.2 (0.8)	0.5 (0.4)
Total		100.0	100.0	100.0	100.0	100.0	100.0	100.0	100.0	100.0	100.0	100.0	100.0	100.0	100.0	100.0	100.0	100.0
	IGV_m^c (Vol %)	46.0	44.3	32.6	32.2	37.1	33.8	36.9	51.9	69.6	33.5	27.6	33.9	28.1	40.6	38.8	31.1	47.9
ϕ_i^b=60%	COPL % [d]	25.9	28.2	40.7	41.0	36.4	39.6	36.6	16.9	--	39.9	39.9	39.5	44.4	32.6	34.7	42.0	23.6
	CEPL % [e]	34.1	29.3	19.3	17.7	22.7	18.8	21.5	40.4	--	18.6	18.6	19.2	14.6	26.8	24.8	16.2	35.0

[a] standard deviation, 2σ. [c] Intergranular volume.
[b] Initial porosity. [d] % of initial porosity lost due to compaction. [e] % of initial porosity lost due to cemntation.